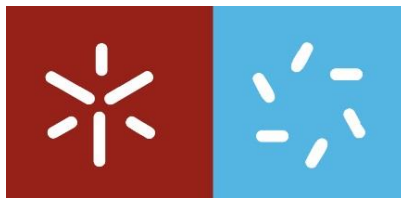University of Minho
School of Sciences

André Filipe Gonçalves de Carvalho

Preparation and characterisation of magnetic dehydropeptide-based hydrogels

October 2018

University of Minho

School of Sciences

André Filipe Gonçalves de Carvalho

Preparation and characterisation of magnetic dehydropeptide-based hydrogels

Master's Dissertation
Medicinal Chemistry

Performed under supervision of
Dr. Manuel Bañobre-Lopez
Dr. José Alberto Martins

October 2018

DECLARATION

Name: André Filipe Gonçalves de Carvalho

Electronic address: andrefcarvalho95@gmail.com

Phone number: (+351) 914 949 210

Citizen ID: 14850886

Supervisor: Dr. José Alberto Martins and Dr. Manuel Bañobre

Dissertation title: Preparation and characterisation of magnetic dehydropeptide-based hydrogels

Conclusion year: 2018

Master's Degree in Medicinal Chemistry

University of Minho, October 31 of 2018

Signature:

_____

Acknoledgements

Abstract

Self-assembled peptide-based hydrogels have emerged in the last decades as a new class of nanostructured biocompatible soft materials with many applications proposed in biomedicine. Our research group has demonstrated recently that dehydrodipeptides *N*-capped with naproxen (Npx, a NSAID drug) are non-toxic to cells, show enhanced stability against proteolysis and self-assemble into entangled nanofibre-based elastic hydrogels. These hydrogels revealed suitable nanocarriers for drug delivery applications. We envisage that dehydrodipeptide-based self-assembled hydrogels could be rendered magneto-responsive by incorporation of superparamagnetic iron oxide nanoparticles (SPIONs). Magnetic hyperthermia (MH) could conceptually be used as a remote trigger for release of incorporated drug cargos. In this Thesis novel dehydrodipeptides, tyrosinyldehydrophenylalanine *N*-protected with naproxen (Npx-Tyr-ΔPhe-OH, **1**) and the methyl ester of *N*-naproxenyl aspartyldehydrophenylalanine (Npx-Asp(OH)-ΔPhe-OMe, **2**) were synthesised and fully characterised by multinuclear NMR spectroscopy and MS.

Methodologies were developed for preparation of hydrogels and for incorporation of SPIONs into the hydrogels. TEM studies showed that the hydrogels are made of entangled nanofibres. CD and FTIR studies suggest that the peptide assumes a β-sheet conformation in the self-assembled nanofibres. Rheological characterization revealed that incorporation of SPIONs (10-30% m/m) into the Npx-Tyr-ΔPhe-OH hydrogel (0.8 wt%) resulted in delayed structural build-up and significant weakening of gel elasticity. Magnetometry experiments revealed that at high SPION loadings (10% m/m) the magnetic hydrogels (0.8 wt%) display a dominant paramagnetic behaviour with a diamagnetic contribution, from the organic hydrogelator matrix, at high magnetic fields. Incorporation of SPIONs (0.01-0.06 % m/m) into hydrogels **1** and **2** (0.4 and 0.8 wt%) resulted in a significant reduction of their transversal relaxivity (r_2). The efficacy (SAR) of the SPIO nanoparticles (20-35 % m/m) as heat generators in magnetic hyperthermia is significantly reduced upon incorporation into the hydrogels (0.8 wt%).

Overall, the results obtained demonstrate that self-assembled dehydrodipeptide hydrogels loaded with SPIO nanoparticles are promising new materials worth further investigation as contrast agents for MRI and Magnetic Hyperthermia triggered drug delivery.

Resumo

Nas últimas décadas surgiu uma nova classe de hidrogéis biocompatíveis baseados em pequenos péptidos (di e tripéptidos) com várias aplicações biomédicas. O nosso grupo de investigação desceveu a auto-associação de desidrodipeptídeos N-protegidos com o anti-inflamatório não esteróide naproxeno (Npx, um fármaco AINE). Estudos posteriores demonstraram que estes materiais não são citotóxicos, são estáveis face a enzimas proteolíticas e dão origem a hidrogéis elásticos baseados numa rede tridimensional de nanofibras. Estes hidrogéis mostraram ser excelentes candidatos para a entrega controlada de fármacos. O objetivo principal deste trabalho consiste no desenvolvimento de hidrogeis de desidropéptidos magnetossensíveis através da incorporação de nanopartículas de óxido de ferro superparamagnético (SPIONs). A hipertermia magnética (HM) seria assim usada como estímulo para a liberação controlada de fármacos. Com este objetivo foram sintetizados e caraterizados dois desidrodeptidos novos, a tirosinildesidrofenilalanina N-protegida com naproxeno (Npx-Tyr-ΔPhe-OH, **1**) e o éster metílico da *N*-naproxenilaspartildesidrofenilalanina (Npx-Asp-ΔPhe-OMe, **2**).

Desenvolveram-se metodologias para a preparação de hidrogéis e para a incorporação de SPIONs nos hidrogéis. Estudos de TEM mostraram que os hidrogéis são constítuidos por uma rede tridimensional de nanofibras. Os resultados de CD e FTIR sugerem que o péptido assume uma conformação de folha β. A caracterização reológica revelou que a incorporação de SPIONs (10-30% m/m) no hidrogel Npx-Tyr-ΔPhe-OH (0.8 wt%) resultou numa diminuição significativa da elasticidade do gel. Ensaios de magnetometria revelaram que com cargas elevadas de SPIONs (10% m/m), os hidrogéis (0.8 wt%), exibem um comportamento paramagnético dominante com uma contribuição diamagnética resultante da matriz de hidrogel orgânico. A incorporação de SPIONs (0.01-0.06% m/m) nos hidrogéis **1** e **2** (0.4 e 0.8 wt%) resultou numa redução significativa da relaxividade transversal (r_2). A eficácia (SAR) das SPIONs (20-35% m/m) como geradores de calor na hipertermia magnética é significativamente reduzida após incorporação nos hidrogéis (0.8 wt%).

Os resultados obtidos demonstram que os hidrogéis resultantes da ato-associação de desidrodipéptidos carregados com SPIONs constituem materiais promissores que merecem uma investigação mais aprofundada como agentes de contraste para IRM e como sistemas de entrega controlada de fármacos baseados na Hipertermia Magnética.

Index

Index of figures

Index of tables

Abbreviations

AMF	Alternating magnetic field
Boc2O	*Tert*-butyl dicarbonate
CA	Contrast agents
cac	Critical aggregation concentration
CD	Circular dichroism
$CDCl_3$	Deuterated cloroform
cgc	Critical gelation concentration
DCC	*N,N*-dicyclohexylcarbodiimide
DCM	Dichloromethane
DMAP	4-dimethylaminopyridine
DMSO-d_6	Deuterated dimethylsulfoxide
DNA	Deoxyribonucleic acid
DOTA	1,4,7,10-Tetraazacyclododecane-1,4,7,10-tetraacetic acid
DTPA	Diethylenetriaminepentaacetic acid
ELR	Echo limiting regime
FC	Field-cooling
FDA	Food and Drug Administration
FeNPs	Iron nanoparticles
FM	Ferromagnetic
Fmoc	Fluorenylmethoxycarbonyl
FRET	Forster ressonance energy transfer
FTIR	Fourier-transform infrared
G'	Elastic modulus
G''	Shear loss modulus
GDL	D-glucono-δ-lactone
HOBt	1-hydroxybenzotriazole
INL	International Iberian Nanotechnology Laboratory
IONP	Iron oxide nanoparticles
J	NMR coupling constant
MAR	Motional average regime
MH	Magnetic hyperthermia
MNPs	Magnetic nanoparticles
MRI	Magnetic resonance imaging
Ms	Saturation magnetization
NEt$_3$	Triethylamine
NMR	Nuclear magnetic resonance
NOE	Nuclear Overhauser
Npx	Naproxen
NSAID	Nonsteroidal anti-inflammatory drug
PAA	Polyacrylic acid
PM	Paramagetic
Ppm	Parts per million
rt	Room temperature
SAR	Specific absorption rate
SBM	Solomon-Bloenbergen-Morgan
SDR	Static dephasing regime
SLP	Specific power loss
SPIONs	Superparamagnetic iron oxide nanoparticles

SQUID	Superconducting quantum interference device
SUVS	Small unilamellar vesicles
TB	Blocking temperature
TEM	Transmission electron microscopy
TFA	Trifluoroacetic acid
TLC	Thin layer chromatography
TMG	N,N,N',N'-tetramethylguanidine
ZFC	Zero-field-cooling

Introduction

Peptide Hydrogels

Conventional self-assembly usually refers to a bulk event where control of structure formation is limited to the spontaneous nature of the process which is, in turn, linked to the molecular structure of the constituting biomolecular amphiphile. The self-association of small molecules to give rise to supramolecular structures is found in several biological processes, essential for the maintenance of life such as the double helix of the DNA or organization of the phospholipids in the cellular membranes. [1]

Nanostructures formed by peptides that self-assemble in water through non-covalent interactions have attracted considerable attention because peptides have several unique advantages such as modular design and easiness of synthesis, convenient modification with known functional motifs, good biocompatibility, low immunogenicity and toxicity, inherent biodegradability and fast responses to wide range of external stimuli. Peptide assembly is a spontaneous thermodynamic and kinetic driven process, based on the synergistic effect of various intermolecular non-covalent interactions such as hydrogen bonding, hydrophobic and aromatic $\pi-\pi$ interactions (Figure 1). [2], [3]
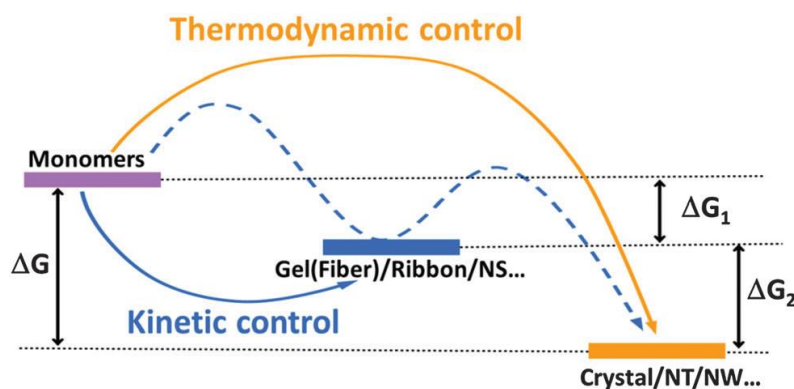
FIGURE 1. SCHEMATIC OF THE ASSEMBLY PATHWAYS.[2]

When low molecular weight peptide molecules start to join together, in response to pH changes or by cooling a super-saturated media, three situations are possible (Figure 2)[4]·[5]

1. Crystallization, in response to a very ordered packing;

2. Formation of a precipitate;

3. Gelation which is an aggregation process intermediate between 1 and 2.
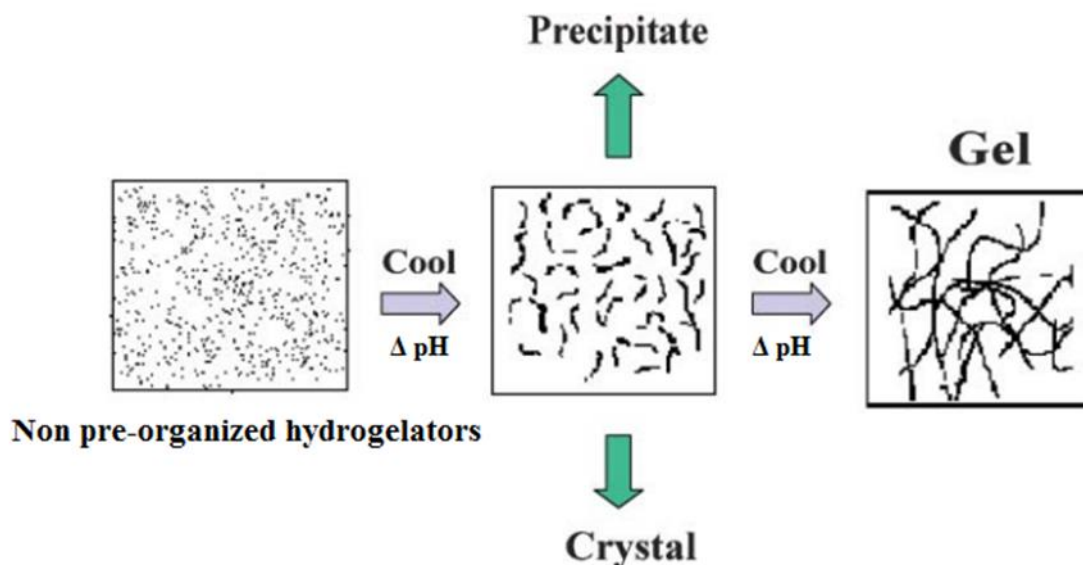
FIGURE 1. SCHEMATIC REPRESENTATION OF AGGREGATION MODES.[4]

Supramoleculargels are formed when small molecules self-assemble into fibrous structures. Above a critical concentration, the entanglement and cross-linking of these structures leads to the formation of a self-supporting gel. Figure 3 shows this hierarchical process.[6]
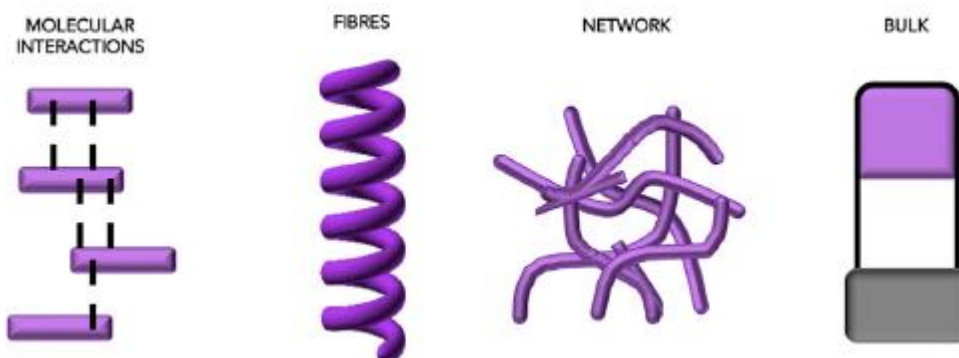
FIGURE 2. HIERARCHICAL PROCESS THAT LEADS TO GELATION OF LOW MOLECULAR WEIGHT HYDROGELATORS.[7]

Functionalised dipeptides are a class of interesting and useful low molecular weight hydrogelators. The balance between the hydrophobic and hydrophilic character of low molecular weight peptide hydrogelators as well as their ability to establish π-π stacking interactions are fundamental issues to be considered when designing these molecules. Johnson *et al* [8] stated that dipeptides should have an ideal hydrophobicity, expressed by the value of log P, to be a potential hydrogelator. These authors report that weak and unstable gels are formed when peptides have log P below 2.8, whereas when log P was above 5.5, the dipeptides appeared to be too hydrophobic to form homogeneous gels. At intermediate values of log P between 3.4 and 5.5, all

3

the dipeptides assembled to give gels. In general, dipeptide hydrogelators are functionalised at the N-terminus with a hydrophobic group, often a large bulky aromatic group such as fluorenylmethoxycarbonyl (Fmoc) or naphthalene group (Figure 4). [2], [7], [9]

P = Dipeptide derivative.
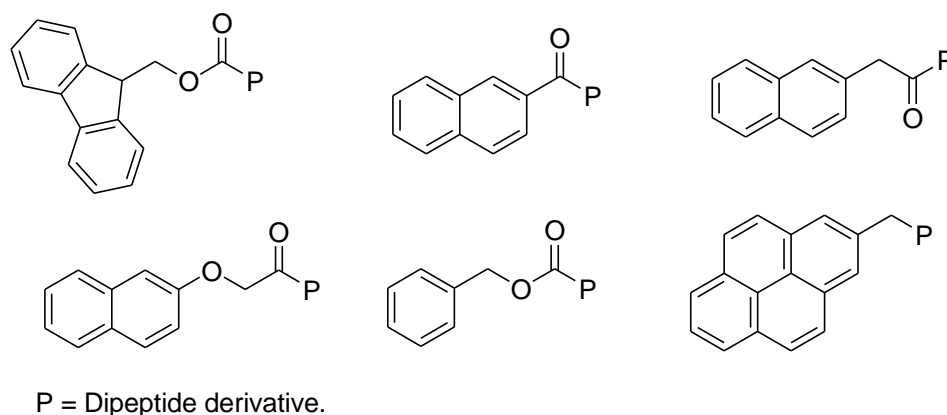
FIGURE 3. STRUCTURES OF *N*-PROTECTING GROUPS USED IN THE DESIGN OF DIPEPTIDE HYDROGELATORS.

Naphthalene-protected dipeptides were first reported by Yang *et all..*[10] This class of material was found to be very robust gelators. For example, 2-naphthylacetylphenylalanylphenylalanine can easily give hydrogels by using a range of triggers such as pH, temperature, enzymatic catalysis or solvent change (Figure 5).
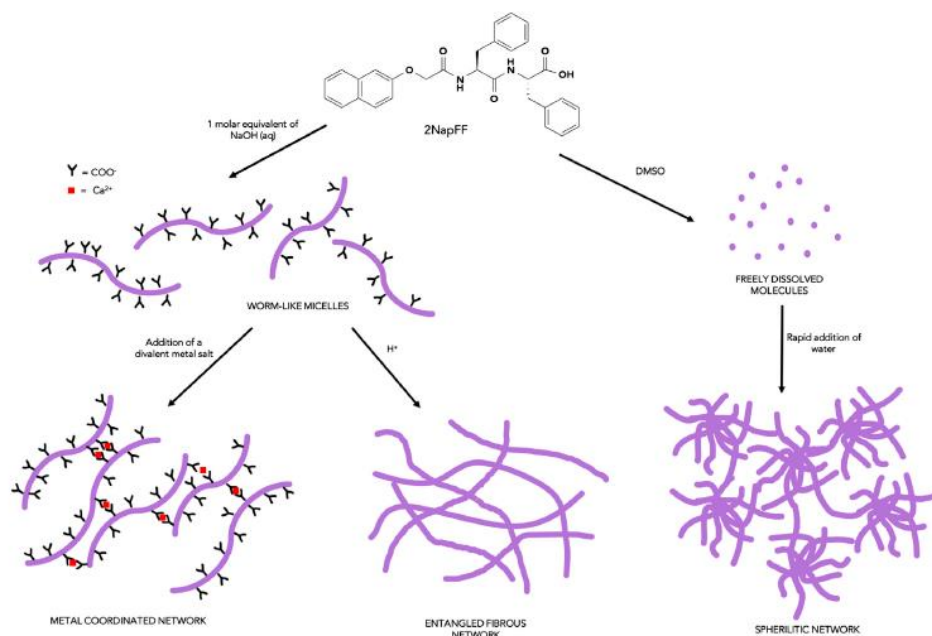
FIGURE 4. GELATION OF 2-NAPHTHYLACETYLPHENYLALANYLPHENYLALANINE.[7]

Enzymatic degradation of this type of hydrogels is another issue that has to be taken into account while designing a peptide hydrogelator. Natural proteinogenic peptide sequences are prone to be readily hydrolyzed by proteolitic enzymes. Though, the introduction of non-

proteinogenic aminoacids is useful to impart proteolytic stability to this type of biomaterials. The latter include D-amino acids, β-aminoacids or dehydroamino acid derivatives. [11] In our laboratories several dehydrodipeptides *N*-capped with the anti-inflammatory non-steroidal drug naproxen were prepared and tested as hydrogelators (Figure 6). [3], [5], [12]

R = Amino side-chain.
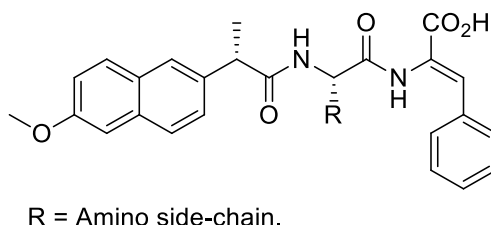
FIGURE 5. STRUCTURE OF THE DEHYDRODIPEPTIDES *N*-PROTECTED WITH NAPROXEN.

These compounds gave hydrogels with low critical gelation concentration and gel–sol phase transition pH between 5 and 8. The hydrogels consist of networks of micro/nanosized fibers formed by peptide self-assembly (Figure 7). Fluorescence and circular dichroism spectroscopy indicate that the self-assembly process is driven by stacking interactions of the aromatic groups. Some of these hydrogels can be potentially applied as drug-nanocarriers.

FIGURE 6. TEM IMAGE OF THE HYDROGEL OBTAINED FROM PHENYLALANINEDEHYDROPHENYLALANINE.[5]

Recently, a new hybrid supramolecular magnetic hydrogel composed of *N*-fluorenylmethoxycarbonylphenylalanylphenylalanine (Fmoc-FF) peptide and iron nanoparticles (FeNPs) was prepared through the self-assembly of Fmoc-FF in a suspension containing FeNPs and in the presence or absence of an external magnetic field.

In this work several hydrogels based on the self-assembly of two dehydrodipeptides with different amounts of iron oxide superparamagnetic nanoparticles will be described as magnetic field trigger drug delivery systems.

Magnetic nanoparticles as Contrast Agents for MRI and Magnetic Hyperthermia

Magnetic nanoparticles, especially iron oxide nanoparticles (IONP) display unique physicochemical properties and high biocompatibility. Manny bottom-up synthetic wet methodologies have been devised for controlled synthesis of highly crystalline IONP. A plethora of applications, ranging from biomedical imaging to drug-delivery and magnetic hyperthermia have been proposed for magnetic IONPs. [13]

The vast majority of magnetic nanoparticles obtained by bottom-up wet methodologies, are made of a magnetic core surrounded by an organic or inorganic corona that precludes nanoparticle aggregation and precipitation in aqueous media. Besides allowing stable dispersion in aqueous media, the organic/inorganic corona can be further functionalized to endow the nanoparticles with extra functionalities, such as molecular recognition by biological receptors and cell internalization. [14]

The physicochemical properties of magnetic nanoparticles are generally ascribed to the inorganic core. Nonetheless, besides its interfacing with the aqueous media and biological tissues, the organic shell may play also an important role in tuning the physicochemical properties of the core.

Superparamagnetic Iron Oxide nanoparticles nanoparticles (SPIONs) are widely used nanoparticles in biomedical applications. The most important applications of SPIONs include biomedical imaging, MRI and multimodal imaging and remotely activated Magnetic Hyperthermia (MH). Magnetic properties of nanoparticles such as saturation magnetization (M_s) and magnetic constant anisotropy (K) are fundamental for applications of nanoparticles in Magnetic Resonance Imaging (MRI) and Magnetic Hyperthermia (MH). [15], [16]

Magnetic properties of SPIONs

The size of the core of magnetic nanocrystals, usually 4-18 nm, is smaller than the size of a magnetic domain. Thus, fully magnetized magnetic domains behave as nanomagnets. The orientation of the magnetization in relation to the crystallographic directions determines the magnetic energy of a nanomagnet. The directions that minimize the magnetic energy are designated anisotropy directions or easy axes. The magnetic energy depends on the tilt angle between the magnetization and the easy axes (Figure 8).
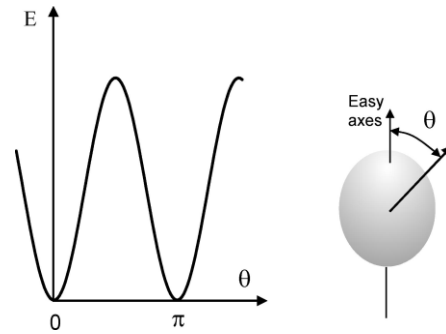
FIGURE 7. DEPENDENCE OF THE MAGNETIC ENERGY ON THE TILT ANGLE (θ) BETWEEN THE MAGNETIZATION VECTOR AND THE EASY AXES. (ADAPTED FROM [16])

The anisotropy energy (E) is directly proportional to the nanocrystal volume (equation 1). [17]

$$E = KV sin^2\theta \qquad \text{equation 1}$$

where K represents the anisotropy constant and V the nanocrystal volume.

The anisotropy energy grows very fast with the size (radius) of the nanocrystal. Moreover, the anisotropy energy depends also on the chemical composition and crystallographic structure of the magnetic material and crystal surface structure. Aggregation/self-assembly of neighbor nanocrystals by dipolar interactions has also a very pronounced effect on the anisotropy constant (K). Elongated nanocristals are characterized by a higher anisotropy constant (K) than spherical nanoparticles.

Alignment of the nanocrystal magnetization with the easy axes minimizes the magnetic energy according to the Boltzmann law. Following a perturbation, the return of the magnetization to equilibrium occurs *via* two different mechanisms: Néel relaxation and Brown relaxation (Figure 9).
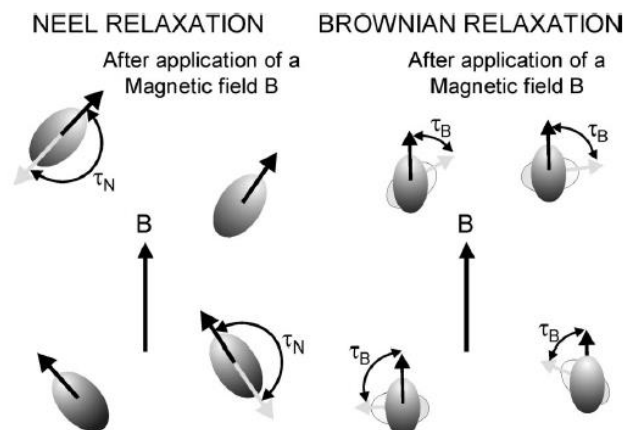
FIGURE 8. SCHEMATIC REPRESENTATION OF THE NÉEL AND BROWNIAN RELAXATION MECHANISMS FOR A MAGNETIC FLUID.[16]

The Néel relaxation mechanism consists of internal rotation (*flipping*) of the magnetic moment between the easy directions, characterized by the Néel relaxation time (τ_N). The Néel relaxation time shows an exponential dependence on the anisotropy energy according to the *Arrhenius* law (equation 2).

$$\tau_N = \tau_0 e^{\frac{E}{kT}} \qquad \text{equation 2}$$

Where T (K) is the absolute temperature; E is the anisotropy energy; k is the Boltzmann constant.

τ_0 is a complex function of the anisotropy energy, nanocrystal volume (V) and nanoparticle magnetization (M). τ_0 usually assume values of the order of magnitude 10^{-9}-10^{-10} s. When the thermal energy is higher than the anisotropy energy ($E<<kT$), the magnetization *flips* between different easy directions without reorientation of the whole nanoparticle. Nanoparticles used as Contrast Agents for MRI or Magnetic Hyperthermia are used as suspensions in aqueous media. In addition to Néel relaxation, the Brownian relaxation defines the magnetic fluctuations brought about by viscous rotation of the entire particle (equation 3).

$$\tau_B = \frac{3V_H \eta}{KT} \qquad \text{equation 3}$$

Where V_H represents the hydrodynamic volume of the nanoparticles; η represents medium viscosity; k is the Boltzmann constant and T the absolute temperature.

The effective relaxation time of a magnetic fluid includes both Néel and Brownian contributions (equation 4):

$$\frac{1}{\tau_{eff}} = \frac{1}{\tau_N} + \frac{1}{\tau_B} \qquad \text{equation 4}$$

At high temperature and low anisotropy conditions ($E<<kT$) the pre-exponential factor dominates the Néel relaxation time which decreases with increasing temperature. While the Néel relaxation time is an exponential function of the nanoparticles volume, the Brownian relaxation is a simple function of the nanoparticles volume. Thus, the Néel relaxation time becomes longer than the Brownian relaxation time for large nanoparticles. [18] The relaxation time of large nanoparticles

in solution is dominated by Néel relaxation (Figure 10).
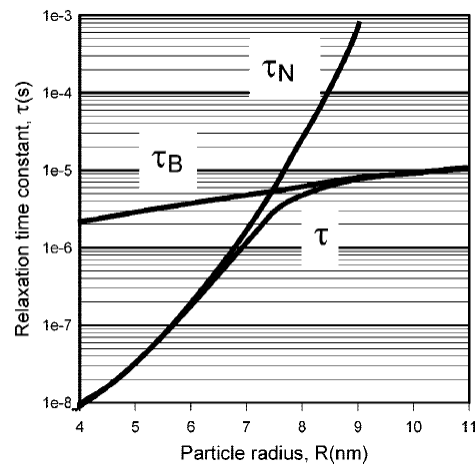
Superparamagnetism involves thermal activated *flipping* of the magnetic moment between the easy directions at temperatures above the *block temperature* ($E \approx kT$). Fast relaxation ensures that the system is always in thermodynamic equilibrium. In these conditions, the magnetization curve of magnetic fluids is fully reversible (Figure 11).
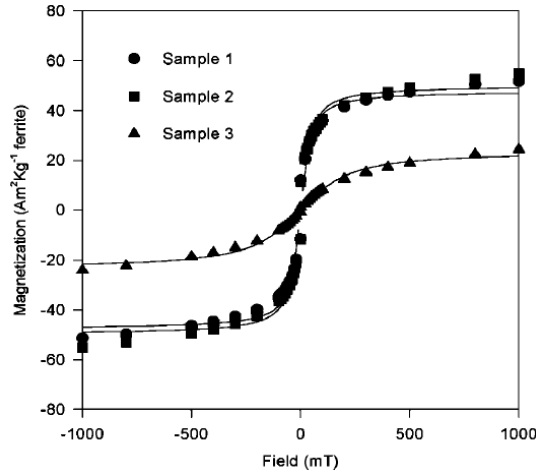
FIGURE 10. DEPENDENCE OF THE MAGNETIZATION OF IONP WITH DIFFERENT SIZES ON THE MAGNETIC FIELD STRENGTH. EXPERIMENTAL DATA POINTS FOR NANOPARTICLES WITH RADIUS 5.59 NM - SAMPLE 1; 5.67 NM - SAMPLE 2 AND 4.84 NM - SAMPLE 3 AND FITTED CURVES - CONTINUOUS LINES. (ADAPTED FROM [16])

Figure 11. Dependence of the magnetization of IONP with different sizes on the magnetic field strength. Experimental data points for nanoparticles with radius 5.59 nm - sample 1; 5.67 nm - sample 2 and 4.84 nm - sample 3 and fitted curves - continuous lines. Adapted from ref [16].

The dependence of the magnetization curve on the magnetic field is proportional to the

Langevin function (equation 5).

$$M = M_s L(x) \quad \text{equation 5}$$

Where M is the magnetization at a specific magnetic field strength, M_s is the magnetization at saturation, and $L(x)$ is the Langevin function.

The Langevin function takes into account a Boltzmann distribution of all possible energy levels for all orientations of the magnetization magnetic moment (equation 6).

$$L(x) = \left[\coth(x) - \frac{1}{x}\right] \; ; \; x = \frac{MsVB_0}{kT} \quad \text{equation 6}$$

Where M_s is the saturation magnetization; V is the nanoparticles volume and B_0 is the magnetic field strength.

IONP with sizes (diameter) below 25 nm usually display superparamagnetic behavior at room temperature. [19]

Saturation magnetization is one of the most important properties that determine the performance of magnetic nanoparticles in MRI and hyperthermia applications.
The saturation magnetization can be optimized by tuning the size, composition and shape of the nanoparticles.[20]–[22]

Aggregation and self-assembly have also a pronounced effect on the saturation magnetization of nanoparticles. [23]

The magnetic properties of magnetite (Fe_3O_4) are determined by the distribution of Fe^{2+} and Fe^{3+} ions amongst the octahedral and tetrahedral sites of the spinel structure.

Crystal structure of Spinel Ferrite

Tetrahedral site

Octahedral site

- A Site ions
- B Site ions
- Oxygen ions
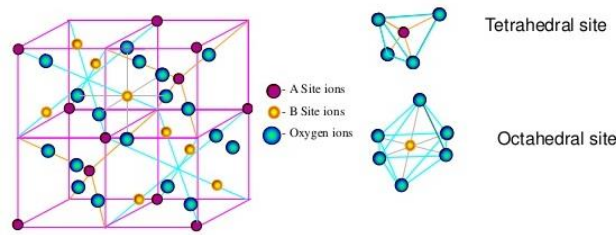
FIGURE 11. UNIT CELL OF SPINEL STRUCTURE. [24]

The number of Fe^{3+} ions occupying octahedral and tetrahedral sites is the same. There is ferromagnetic coupling between the Fe^{3+} ions occupying the octahedral sites. These are in turn coupled antiferromagnetically to the Fe^{3+} ions on the tetrahedral sites. As consequence, the magnetic moment of magnetite is determined only by the magnetic spin of the Fe^{2+} ions (4 unpaired electrons - 4 μ_B). Spinel ferrite structures MFe_2O_4 ($MO(Fe_2O_3)$) obtained by replacement of Fe^{2+} by other divalent metal ions ($M^{2+} = Fe^{2+}$, Mn^{2+}, Co^{2+}, Zn^{2+}) display different net magnetic moments, proportional to the magnetic spin of the M^{2+} ion. [21]
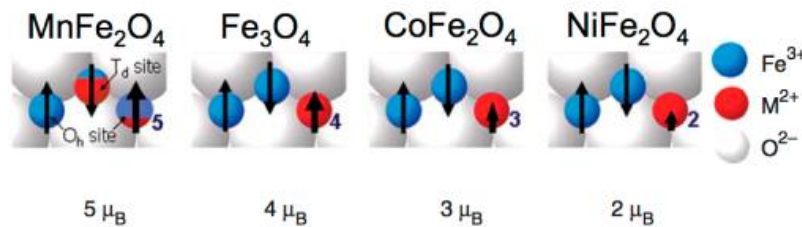
FIGURE 12. SCHEMATIC REPRESENTATION OF THE SPIN ALIGMENTS IN FERRITE STRUCTURES MFE2O4 (M^{2+}= FE^{2+}, MN^{2+}, CO^{2+}, ZN^{2+}, NI^{2+}).[21]

The saturation magnetization M_s of nanoparticles with spinel ferrite structure MFe_2O_4 ($MO(Fe_2O_3)$) (M^{2+}= Fe^{2+}, Mn^{2+}, Co^{2+}, Ni^{2+}) is determined by the magnetic spin moment (μ) of the M^{2+} ion. Moreover, in the superparamagnetic regime the saturation magnetization M_s increases with size (Figure 14).[24]
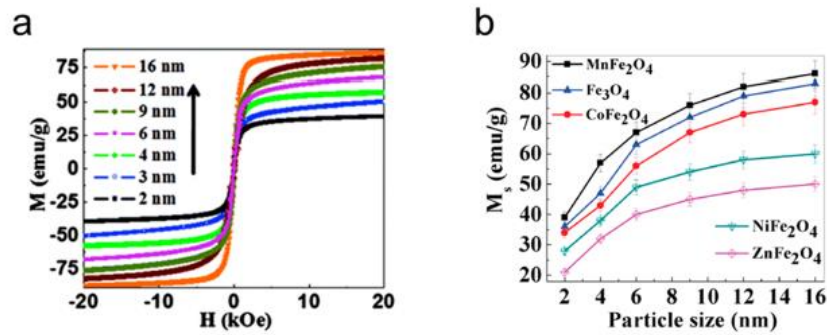
FIGURE 13. EFFECT OF SIZE OF MNFE2O4 NANOPARTICLES (A) AND COMPOSITION (B) OF FERRITE SPINEL STRUCTURES MFe_2O_4 (M^{2+}= Fe^{2+}, Mn^{2+}, Co^{2+}, Zn^{2+}, Ni^{2+}) ON SATURATION MAGNETIZATION.[24]

Self-assembly and controlled aggregation of nanoparticles has been described as smart strategy to enhance the saturation magnetization of nanoparticles.[25]

The shape of the nanocrystal has also a strong effect on the saturation magnetization. Nanoparticles with anisotropic shapes, such as nanocubes, display higher saturation magnetization than spheric nanoparticles, with the same number of atoms, due to proportionally lower contribution of *spin canting* effects to the total magnetization. [26]

Magnetic nanoparticles as contrast for MRI and Hyperthermia

Paramagnetic relaxation

MRI is the leading imaging modality in clinical imaging allowing anatomical and functional imaging with high spatial-temporal resolution. Importantly, MRI makes use of benign radiation - magnetic fields and radiofrequencies shows no penetration limitations for imaging of soft tissues. The main limitation of MRI is low detection sensitivity- inherent to the Nuclear Magnetic Resonance (NMR) phenomenon. [27]
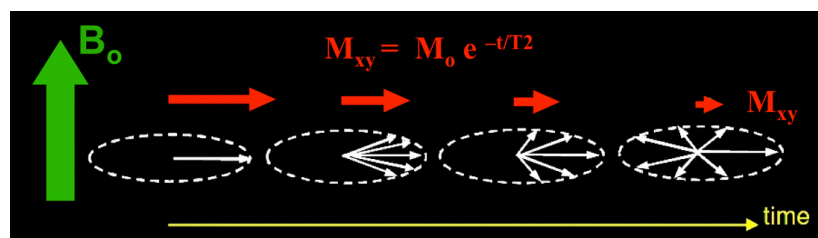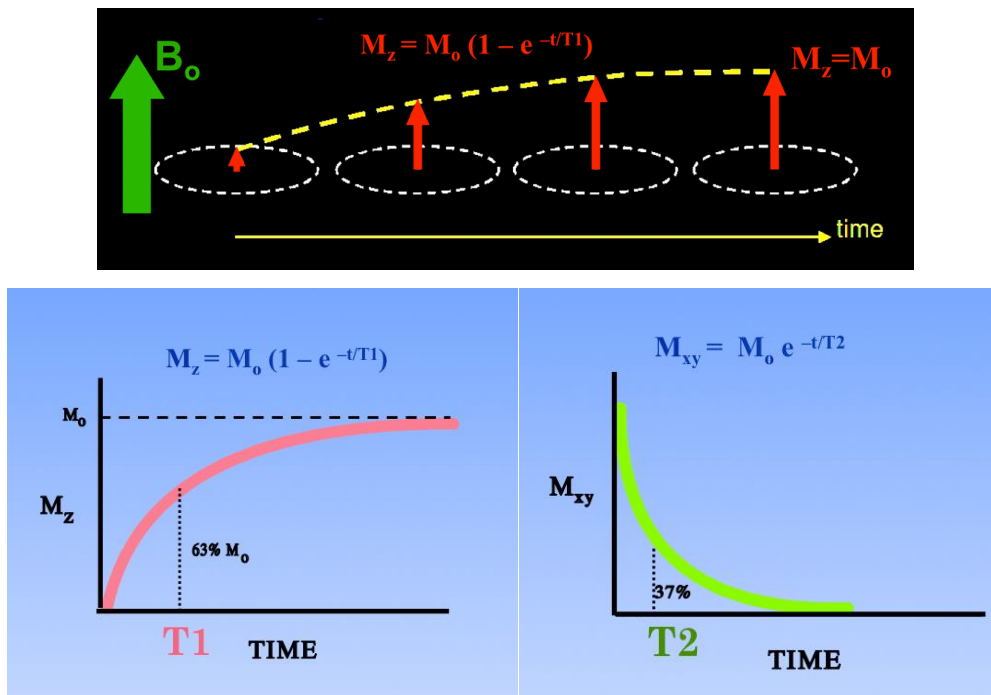
The return of the magnetization to equilibrium after excitation, can be described by two relaxation mechanisms - longitudinal relaxation (spin-lattice relaxation) and transverse relaxation (spin-spin relaxation). Flipping of polarized spins in the excited state leads to recovery of longitudinal magnetization, characterized by relaxation time T_1 - time required for the magnetization to reach 63% of its original value starting from zero. Dephasing of the nuclear spins leads to decrease of the transverse magnetization, characterized by relaxation time T_2 - time required for the transverse magnetization to decay to 37% of its maximum value in the excited state. [28] Contrast in MRI arises from intrinsically different relaxation times $T_{1,2}$ of the water protons of the tissues and differences in water abundance. Thus, in many clinical situations contrast reveals insufficient for diagnostics purposes. Higher detection sensitivity and better spatial resolution can be achieved by using higher magnetic fields (B_0). However, higher magnetic fields imply also the use of higher radiofrequency power. Absorption of high-power radiofrequency radiation by body tissues can lead to uncontrolled heating. Currently, MRI imagers are limited to 1.5 and 3 T (60 and 120 MHz). Magnetic relaxers (paramagnetic ions and magnetic nanoparticles) speed up the relaxation of the water protons of tissues. Gd^{3+} chelates and IONP are used clinically as contrast agents (CA) for MRI.[29]

The relaxation rates $R_{1,2} = 1/T_{1,2}$ measure the rate of recovery of the longitudinal magnetization and the rate of loss of transversal magnetization, respectively. Thus, a contrast agent leading to selective shortening of T_1 generates bright images (positive contrast) in MRI while a CA

that leads to selective shortening of T_2 originates dark images (negative contrast).

The efficacy of a contrast agent is measured by the parameter relaxivity. Relaxivity ($r_{1,2}$) is defined as the selective enhancement of the relaxation rates ($R_{1,2}$; $R_{1,2}= 1/T_{1,2}$) (selective reduction of the relaxation times, $T_{1,2}$) of the water protons normalized to 1 mM concentration of paramagnetic species (equation. 7).

$$R_{1,2\,(obs)} = \frac{1}{T_{1,2}} = \frac{1}{T_{1,2\,(diam)}} + r_{1,2}C \ ; \ i = 1,2 \qquad \text{equation 7}$$

Where $R_{1,2}$ (s^{-1}) represents the measured relaxation rate for the water protons; $T_{1,2(diam)}$ (s) represents the relaxation time measured before adding the paramagnetic species; $r_{1,2}$ is the relaxivity (mM^{-1}s^{-1}); C represents the concentration of paramagnetic species in the aqueous system.

Besides high relaxivity, the ratio r_2/r_1 is important for MRI imaging as a strong T_2 effect will cause an attenuation of the effective T_1 effect in T_1-weighed imaging. In general, a T_1 CA should display a r_2/r_1 ratio around $1/10$.

Complexes of paramagnetic metal ions (Gd^{3+}, Mn^{2+}, Fe^{3+}) and stable organic radicals are effective CA for T_1-weighed MRI. Gd^{3+} (4f^7, seven unpaired electrons) is the most effective metal ion for MRI. Owing to toxicity issues Gd^{3+} ions must be used *in vivo* chelated with organic ligands to ensure fast elimination unchanged. Octadentate Macrocyclic (DOTA-type) and linear (DTPA-type ligands) form complexes with Gd^{3+}ions with exceptional thermodynamic stability and kinetic inertness. [29]

Still, Gd^{3+} release *in vivo* has been implicated as the cause of the serious condition Nefrogenic Systemic Fibrosis. [30]

Although not totally free of toxicity concerns, Mn^{2+} complexes are emerging as potential Gd^{3+} replacements.[31] The physico-chemical model for paramagnetic relaxation, widely used to study the relaxivity of complexes of paramagnetic metal ions (Gd^{3+}, Mn^{2+}, Fe $^{3+}$) was originally developed by Solomon-Bloenbergen-Morgan - SBM model.[29]

This mechanism proposes that the relaxation of the water protons has two contributions: an inner sphere contribution, arising from water coordination to the metal ion; and outer-sphere contribution arising from the diffusional movement of the water molecules near the magnetic field gradients generated by the paramagnetic metal complex. The dipolar coupling between the nuclear

spin of the water protons and the spin of the unpaired electrons on the metal ion is determined by the rotational dynamics of the complex in solution (rotational correlation time- τ_R), the exchange rate (k_{ex}) of the coordinated water molecule, the distance between the protons of the coordinated water molecules and the metal ion (d), and the electron relaxation of electronic spin of the metal ion. The outer-sphere contribution to the relaxation is modulated by the translational correlation time τ_D ($\tau_D=d/D$), which is determined by the relative diffusion constant (D) of the paramagnetic complex and the water molecules and the distance of closest approach (d) between the complex and the diffusing water molecules (Figure 16).
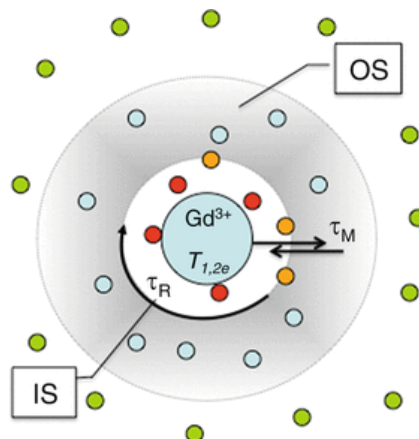
FIGURE 15. SCHEMATIC REPRESENTATION OF THE MOLECULAR PARAMETERS THAT DETERMINE THE RELAXIVITY OF A PARAMAGNETIC COMPLEX. (GREEN- BULK WATER; BLUE- WATER MOLECULES IN THE OUTER SPHERE (OS); RED- COORDINATED WATER MOLECULES ON THE INNER SPHERE (IS); ORANGE-EXCHANGING WATER MOLECULES) ADAPTED FROM REF [29])

The relaxivity of most Gd^{3+} complexes is mainly determined by the inner-sphere relaxation mechanism. The outer sphere relaxation contribution to the relaxivity of paramagnetic complexes (Gd^{3+}, Mn^{2+}, Fe^{3+}) is in general negligible. The design of metal complexes endowed with high relaxivities is a multiparameter problem requiring simultaneous optimization of all parameters that determine relaxivity, mainly τ_R and k_{ex}. [29]

Superparamagnetic relaxation

IONP display high biocompatibility and very low toxicity: injected nanoparticles are degraded *in vivo* and the surplus iron is incorporated into the physiological pools or used in metabolic processes.

SPIONs are preferencially used as T_2 contrast agents for MRI due to their strong T_2 effect and high ratio r_2/r_1. The SBM model can explain the T_2 relaxation effect of SPIONs by considering that its effect is mediated by the outer sphere relaxation mechanism - fast diffusion of water

molecules in the vicinity of the nanoparticles. Thus, the relaxation effects of SPIONs are modulated by the diffusional correlation time τ_D and by the Néel relaxation time τ_N (equation 8).

$$\frac{1}{\tau_C} = \frac{1}{\tau_D} + \frac{1}{\tau_N} \qquad \text{equation 8}$$

The global relaxation time τ_C permits to establish a boundary condition where the magnetic fluctuations generated by the nanoparticles will be effective in relaxing the water protons (equation 9). [16]

$$\omega_1 \tau_C < 1 \qquad \text{equation 9}$$

Where ω_1 is the angular speed of the proton precession, dependent on the magnetic field B_0.

The relaxivity r_2 of SPIONs is strongly affect by the nanoparticle magnetization. Thus, composition and size of the nanocrystal, and the state of agglomeration/self-assembly are the main factors that determine the performance of SPIONs as CA for MRI.

Effect of nanoparticle size on the relaxivity

The effect of nanoparticle size on r_2 can be rationalized by three different regimes: motional average regime (MAR - I), static dephasing regime (SDR - II) and echo limiting regime (ELR - III) (Figure 17).
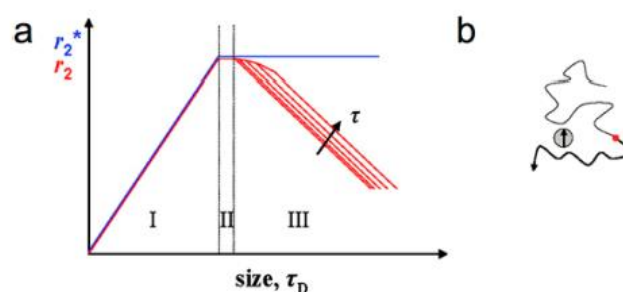
FIGURE 16. SIMULATED EFFECT OF THE SIZE OF NANOPARTICLES ON THE R_2 RELAXIVITY.[16]

In the MAR, fast diffusion of the water molecules in the vicinity of the nanoparticles results in averaging of the magnetic fields generated by the nanoparticles. In this regime the transversal

A

relaxivity r_2 is proportional to the magnetization of the nanoparticles which is in turn determined by the size of the nanocrystal (Figure 18).
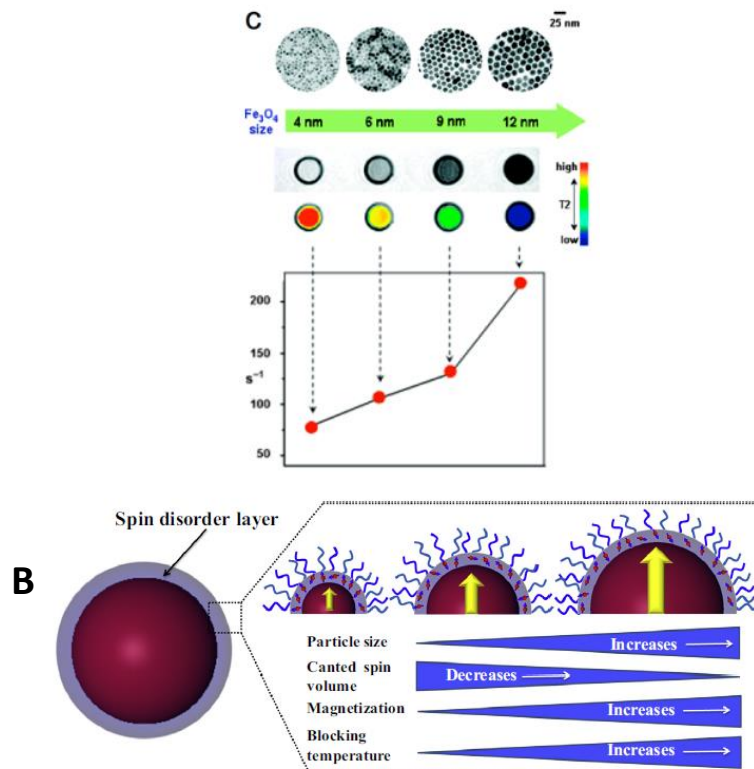
As seen above the magnetization of nanoparticles increases with the size of the nanocrystal (Figure 18b). The magnetic spins on the surface of nanoparticles are intrinsically disordered due to their unique state - *spin canting* effect (Figure 18B). This disordered surface layer, displaying iron ions with incomplete (frustrated) coordination, contributes little to the magnetization of the nanoparticles being responsible for the T_1 effect observed with SPIONs. Therefore, r_2 and the ratio r_2/r_1 increases with the increasing size of SPIONs due to high volume/surface ratio and the reduction of the *spin canting* layer contribution as the size of the nanoparticles increases and the surface curvature decreases. [20], [33]

As the size of the nanoparticles increases, the magnetic fields generated by the nanoparticles become so high that the diffusion of the water molecules is no longer limiting and the relaxivity reaches a plateau - SDR.

When the size of the nanoparticles exceeds the SDR the water protons are dephased so fast by the magnetic field generated by the nanoparticles that fewer spins are refocused by the echo sequence resulting in a decrease of r_2 - ELR. Nanoparticles whose size is in the SDR and the ELR regimes are ferrimagnetic. Their magnetization curves show remanent magnetization as their

magnetic moments are not randomized by the thermal energy. These nanoparticles are prone to aggregation and embolization *in vivo* which limits their uses *in vivo*. However these nanoparticles show great potential for cell tracking applications as particle aggregation inside cells is less problematic.[32]

Effect of nanoparticle composition on the relaxivity

As discussed above, the saturation magnetization M_s of nanoparticles with spinel ferrite structure MFe_2O_4 $(MO(Fe_2O_3))$ $(M^{2+}= Fe^{2+}, Mn^{2+}, Co^{2+}, Ni^{2+})$ is determined by the magnetic spin moment (μ) of the M^{2+} ion. [21]

Replacement of Fe^{2+} by divalent metal ions M^{2+} $(M^{2+}= Mn^{2+}, Co^{2+}, Ni^{2+})$ with a diferent magnetic spin is a strategy to obtain magnetic materials with different net magnetic moments – proportional to the M^{2+} ion magnetic spin.
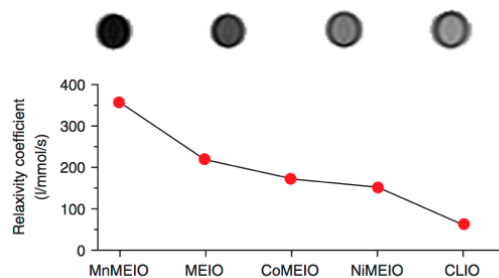
FIGURE 18. EFFECT OF THE NET MAGNETIC MOMENT OF MAGNETISM-ENGINEERED IRON OXIDE (MEIO) NANOPARTICLES MFE_2O_4 $(M^{2+}= MN^{2+}, FE^{2+}, CO^{2+}, NI^{2+})$ ON R_2.[21]

Mn ferrite ($\mu= 5$, Mn^{2+} has 5 unpaired electrons) is the most efective CA for T_2 imaging amongst the materials studied. Concerns about Mn toxicity still limit the use of Mn ferrite nanoparticles *in vivo*. [21]

Ferromgnetic Fe displays the highest magnetization due to absence of cancelled spins. However its tendency for oxidation upon exposure to oxigen limits its aplications *in vivo*. [34]

Effect of coating and aggregation of nanoparticles on the relaxivity

Coated nanoparticles with an organic/inorganic layer can have a strong effect on the relaxivity of magnetic nanoparticles. The thickness of the organic layer does not show a significant effect on r_1 as the T_1 effect is determined mainly by the *canting effect* of the magnetic spins on the

surface crystal layer. If the organic layer is too narrow, nanoparticle aggregation can lead to substantial increase of r_2. On the other hand, if the organic layer is too thick, then the distance of closest approach of the water molecules to the nanoparticles is too long, preventing the water molecules to sense the gradient of magnetic field generated by the nanoparticles. The result is a weakening of T_2 effect. [35]

Controlled aggregation/self-assembly of SPIONs can be used as a powerful strategy to increase r_2, as long as the nanoparticles aggregates remain in the superparamagnetic static dephasing regime (SDR). For SPIONs the SDR limit is of the order of magnitude 100 nm. Nanoparticle clusters behave as magnetic supersized nanoparticles. Given that the T_2 effect depends on the net magnetization, nanoparticle clusters display high relaxivity. [36]

The inclusion of nanoparticles clusters into amphiphilic block-copolymer micelles and biomolecule-based micelles are successful strategies to attain high relaxivities.[33], [37] Assembly-disassembly of nanoparticle aggregates triggered by external trigger stimuli is an elegant strategy to generate smart responsive T_2 CA. [38]

Magnetic Hyperthermia

Superparamagnetic single domain nanoparticles generate heat from magnetic spin relaxation instead of hysteresis loss. As described above *flipping* of the magnetic moment between the easy magnetization directions has to overcome the anisotropy energy barrier. In an alternating magnetic field (AMF) the repeated process of magnetization reversal and realignment with the easy magnetic directions requires energy. Néel relaxation of magnetic spin occurs with energy dissipation as heat. Brownian relaxation can also generate heat by rotational friction in aqueous media. Maximal heating can be attained by Néel or Brownian relaxation when the frequency (f) of the AMF magnetic field match $1/2\pi\tau$ with $\tau = \tau_N$ or τ_B respectively. [18]

The specific absorption rate (SAR) parameter (called also specific loss power, SLP) measures the efficacy of the magnetic nanoparticles has heat generators (equation 10).

$$SAR = \frac{C\,V_s}{m}\frac{dT}{dt} \qquad \text{equation 10}$$

C (J/(K.cm³) represents the volumetric specific heat capacity of the nanoparticles sample, usually approximated by the specific heat capacity of pure water. Vs (cm³) represents the volume of the sample, m (g) represents the mass of magnetic active material.

The SAR can be determined from the initial rate of temperature raise (dT/dt; K.s^{-1}) observed in experimental T vs t curves – calorimetric method (Figure 20).
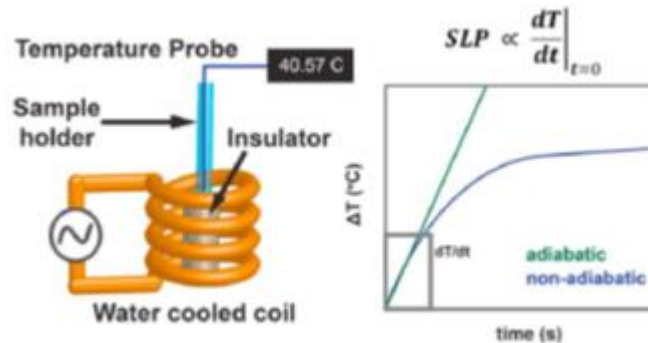
FIGURE 19. SCHEMATIC DIAGRAM OF THE CALORIMETRIC METHOD FOR THE DETERMINATION OF THE SAR. [39]

In the calorimetric method, the temperature increase of a solution of magnetic nanoparticles, excited by an AC magnetic field, is measured over time with an optical fibre temperature probe. A magnetic induction heating system cooled by a water coil and connected to a high-power radiofrequency generator is used for magnetic actuation. A thermally insulated sample container is used to minimize heat loss during heating. [40]

The SAR depends on several parameters related to the AMF field (frequency- f and amplitude- H), magnetic properties of the nanoparticles (density of nanoparticles - $_\gamma$, saturation magnetization- M_s and anisotropy constant) and environment properties such as medium viscosity- η (equation 11)

$$SAR = \frac{\mu_0 H M_s}{2\rho} L(\gamma) \frac{\omega^2 \tau_{eff}}{1+(\omega\tau)^2} \quad equation 11$$

µo represents vacuum permittivity, τ represents the effective relaxation time, ω represents the angular frequency and L the Langevin function.

SAR is directly proportional to the saturation magnetization (Ms) of the nanoparticles, but peaks for specific values of size and magnetic anisotropy (Figure 21). [18]
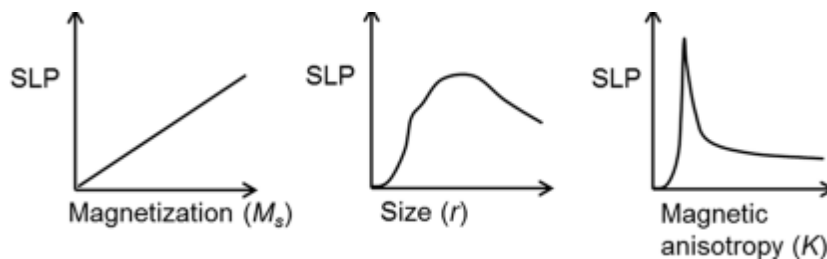
FIGURE 20. SCHEMATIC REPRESENTATION OF THE GENERAL TRENDS FOR THE DEPENDENCE OF THE SAR ON THE SATURATION MAGNETIZATION, SIZE AND MAGNETIC ANISOTROPY OF MAGNETIC NANOPARTICLES.[18]

Saturation magnetization is eventually the most important parameter governing SAR in superparamagnetic nanoparticles. SAR is also proportional to the amplitude H and square frequency f of the AC magnetic field. Tumor therapy by magnetic nanoparticle hyperthermia requires that the temperature inside the tumor reaches 45 °C to induce cell death by apoptosis. For safety reasons it is accepted that the product Hf must be lower than $5 \times 10^9\,\mathrm{Am^{-1}\,s^{-1}}$ for *in vivo* therapeutic applications. [41]

Nanoparticles displaying high SAR can reach the target temperature at lower doses, minimizing potential toxicity to surrounding tissues. The effect of the saturation magnetization, size and composition of the nanoparticles on the SAR is similar to their effects on the performance of the nanoparticles as CA for MRI discussed above.

Simultaneous optimization of the parameters Ms, size and magnetic anisotropy is required to obtain nanoparticles displaying optimized high SAR (Figure 22).
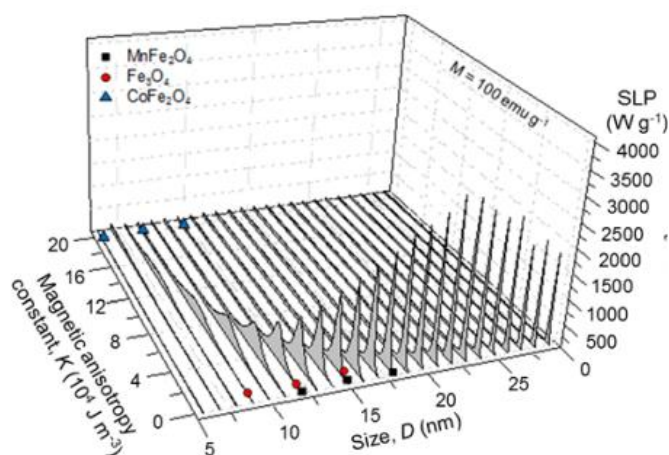
FIGURE 21. SIMULATION OF THE EFFECT OF NANOPARTICLE SIZE (D) AND MAGNETIC ANISOTROPY CONSTANT (K) ON THE SLP AT A FIXED SATURATION MAGNETIZATION VALUE OF 100 EMU/G.

For the selected value of saturation magnetization (100 emu/g; typical of highly cristalline SPIONs) SAR values in the range 1000-4000 W.g^{-1} could be obtained with nanoparticles with an anisotropy constant (K) in the range $(0.5\text{-}4)\times10^4$ J m^{-1} and diameter between 10-30 nm.[39] While

there are synthetic methodologies for size controlled synthesis, preparing nanoparticles with taylor-made anisotropy is more challenging.

Changing the shape of the nanoparticles, for example going from spheres to cubes, induces a change of surface anisotropy that affects the *spin canting* effects.The effect of surface anisotropy on the SAR can be enhanced by doping cubical and spherical iron oxide nanoparticles with transition metal ions, such as Zn^{2+} ions.[39], [42]
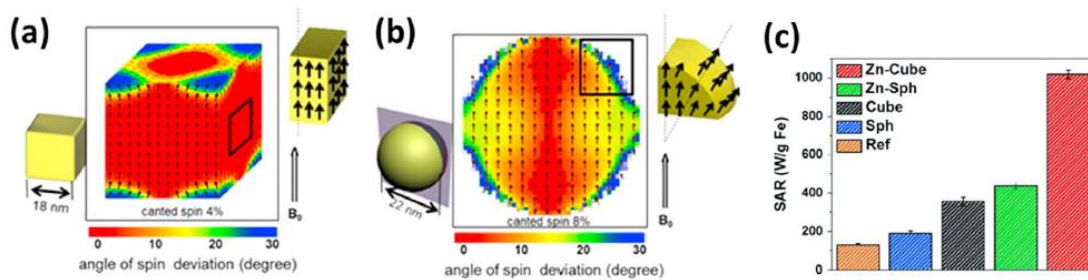
FIGURE 22. SIMULATION OF THE SURFACE ALIGNMENT OF THE MAGNETIC SPINS (SPIN CANTING) IN CUBIC AND SPHERICAL NANOPARTICLES (A) AND (B); C) EFFECT OF DOPING SPHERICAL AND CUBIC MAGNETITE NANOPARTICLES WITH Zn^{2+} ($Zn_{0.4}Fe_{2.6}O_4$) ON THEIR SAR.[39], [42]

$Zn_{0.4}Fe_{2.6}O_4$ nanocubes show an SLP value about twice that measured for the $Zn_{0.4}Fe_{2.6}O_4$ nanospheres. The SAR of IONPS can be optimized also by shape anisotropy: going from spherical (140 W/g), to cubical (314 W/g) to nanorods (862 W/g) of similar magnetic volume Srikanth and co-workers attained a significant enhancement of SAR. [43]

Self-association of magnetic nanoparticles by dipole-dipole interactions can have either an enhancing or a negative effect on hyperthermia, depending on the type of nano-association formed during the hyperthermia experiment (Figure 24).
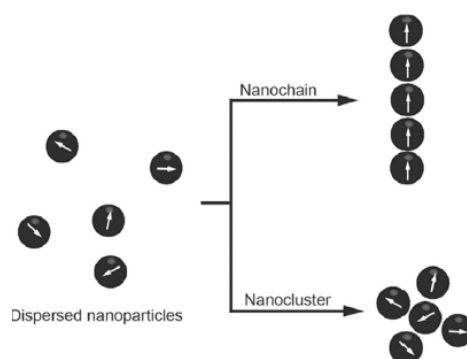
FIGURE 23. SCHEMATIC REPRESENTATION OF NANO-ASSEMBLIES (CHAINS AND CLUSTERS) THAT CAN FORM IN SOLUTION DURING HYPERTHERMIA EXPERIMENTS.

In general self-association into nanochains leads to enhancements of hyperthermia

performance while nanoclusters seem to have a negative effect on hyperthermia. [44], [45]

Despite tremendous efforts and steady progress there is only one formulation of SPIONs approved for human use as CA for T_2 MRI - ferumoxide (Feridex). A formulation containing IONPs with core size 4.5 nm and hydrodynamic diameter 160 nm resulting from stabilization with a dextran layer. Ferumoxide displays high T_2 relaxivity (r_2= 120 mM^{-1}s^{-1}; r_1= 10.1 mM^{-1}s^{-1}; 1.5 T) and a r_2/r_1 ratio suitable for T_2 imaging.[46] Regarding magnetic hyperthermia the first clinical treatment system was developed at the Medical University of Berlin in 2004. [47]

In 2008 *Magforce* was granted regulatory approval for treating patients with brain tumors with hyperthermia in Europe. Still FDA approval has not been granted in the US.[48]

This gap between the state of the art of scientific development and relevant clinical application will be probably closed in a near future with the development of effective nanosystems with demonstrated efficacy and safety. Multifunctional agents with demonstrated imaging (MRI) and therapy (hyperthermia) capabilities and safety are likely to have a great impact on diagnostic and therapy of cancer.

Results and discussion

The research group established in previous works that self-assembled Naproxen N-capped dehydrodipeptide hydrogels are potential nanocarriers for drug delivery applications. Model drugs were incorporated into the hydrogels during gelation. Non-covalent association of the drug molecules with the hydrogel nanofibres was demonstrated by steady-state fluorescence and Forster Resonance Energy Transfer (FRET) experiments. Importantly, drug delivery from the hydrogel to phospholipid Small Unilamellar Vesicles (SUVS) was demonstrated.[3], [49] Proteolytic resistance of the dehydrodipeptide hydrogelator molecules is likely to increase the in vivo life time of the hydrogels.[3]

We envisaged that dehydrodipeptide-based self-assembled hydrogels can be rendered magneto-responsive by incorporation of superparamagnetic iron oxide nanoparticles (SPIONs). Magnetic hyperthermia (MH) could be used as a remote trigger for release of cargos incorporated into the self-assembled hydrogels.

In this project we study the incorporation of SPIONs into dehydrodipeptide-based self-assembled hydrogels and the effect of the SPIONs on the self-assembly and nanostructure of the hydrogels. The effect of the hydrogel matrix on the properties of the SPIONs, as water magnetic relaxers (Contrast Agents for MRI) and as agents for magnetic hyperthermia is studied as well.

Synthesis

Two dehydrodipeptides N-protected with the non-steroidal anti-inflammatory drug naproxen were prepared using a strategy that involves the synthesis of a β-hydroxydipeptide followed by dehydration and removal of the methyl ester (Figure 25). One of the dehydrodipeptides has a tyrosine residue (Npx-L-Tyr-Z-ΔPhe-OH, **1**) and the other has an aspartic acid residue (Npx-L-Asp-Z-ΔPhe-OMe, **2**).

Npx-Tyr-ΔPhe-OH, **1**   Npx-Asp-ΔPhe-OMe, **2**
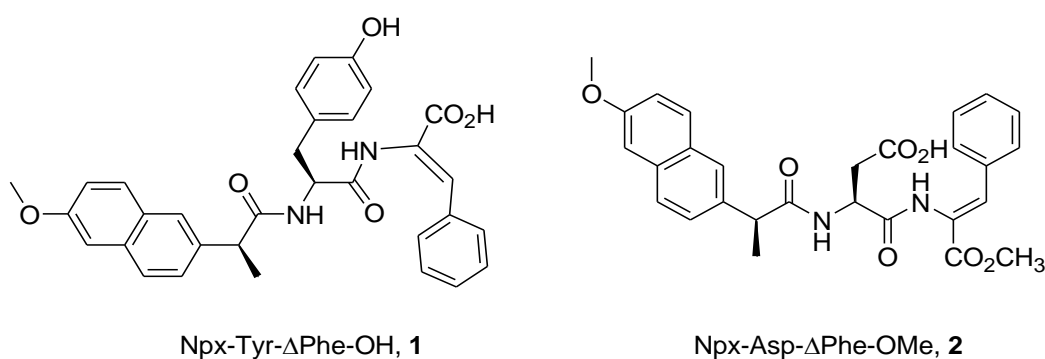
FIGURE 24. DEHYDRODIPEPTIDES **1** AND **2** N-CAPPED WITH THE NONSTEROIDAL ANTI-INFLAMMATORY DRUG NAPROXEN.

Compound **1** was prepared using a conventional stepwise protocol (Scheme 1).
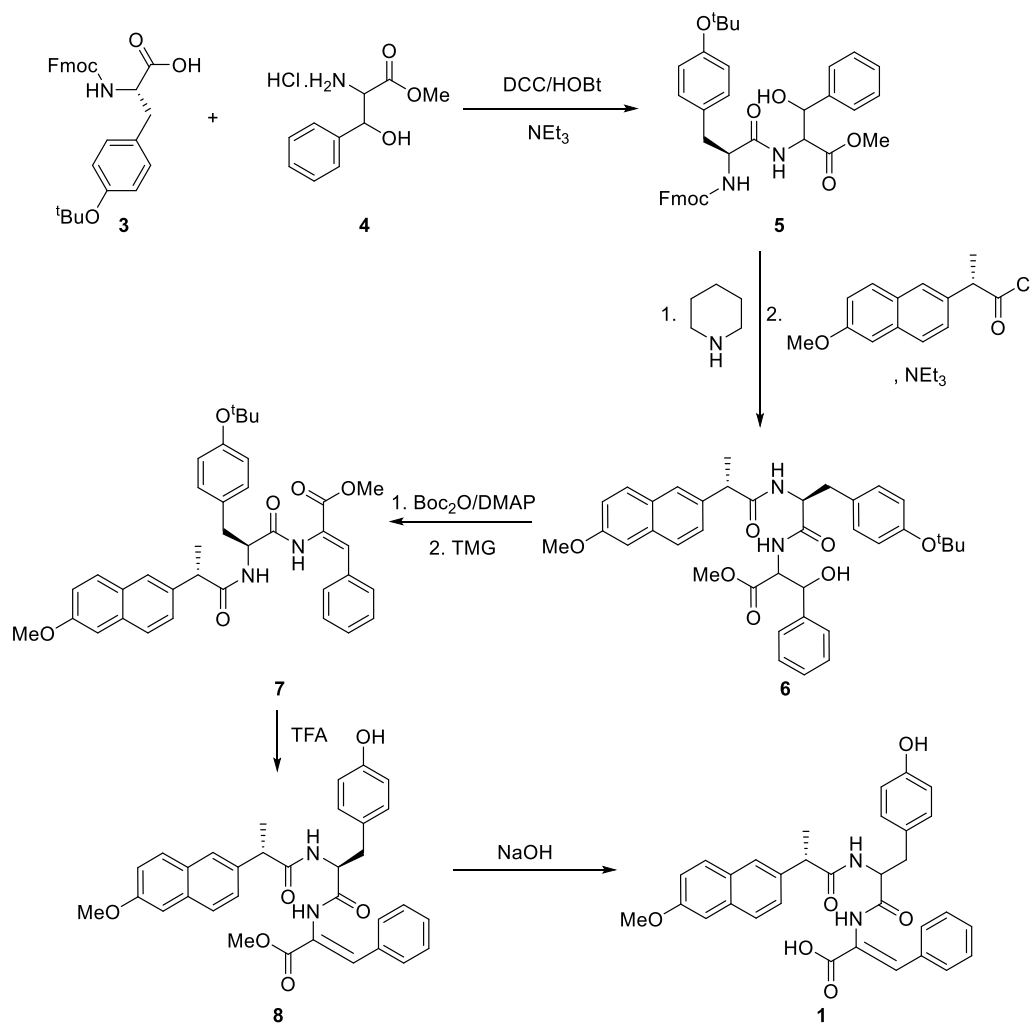
SCHEME 1. SYNTHESIS OF THE DEHYDROPEPTIDE NPX-TYR-ΔPHE-OH, **1**

The coupling of the *tert*-butyl ether of *N*-fluorenylmethoxycarbonyltyrosine [Fmoc-L-Tyr(O^{t}Bu)-OH, **3**) with methyl ester of D,L-β-hydroxyphenylalanine [HCl.H-D,L-Phe(β-OH)-OMe, **4**] was carried out using the classical approach with *N,N'*-dicyclohexylcarbodiimide (DCC) and 1-hydroxybenzotriazole (HOBt). Carbodiimide activation of amino acid derivatives often causes partial racemization of the amino acid. To avoid this problem is useful to add a nucleophile such as 1-hydroxybenzotriazole (HOBt). This compound reacts with the *O*-acyl urea to give hydroxybenzotriazole active esters (Scheme 2).
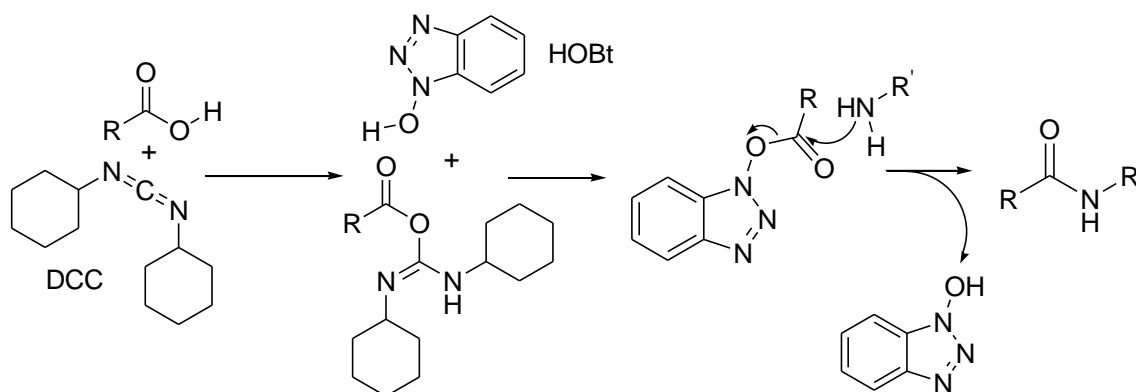
SCHEME 2. DCC / HOBT COUPLING REACTION BETWEEN CARBOXYLIC ACIDS AND AMINES.

The β-hydroxydipeptide **5** was obtained in 89 % yield as a diastereomeric mixture. This compound was first treated with piperidine to remove the fluorenylmethoxycarbonyl (Fmoc) group followed by reaction with (S)-(+)-naproxen chloride to give dipeptide **6** N-protected with naproxen. The latter was dehydrated using *tert*-butyl dicarbonate (Boc$_2$O) and 4-dimethylaminopyridine (DMAP) followed by treatment with *N,N,N′,N′* -tetramethylguanidine (TMG).[50] This reaction involves the formation of a carbonate that undergoes elimination with TMG to give stereoselectively the Z-isomer of the dehydroamino acid derivative (Scheme 3).
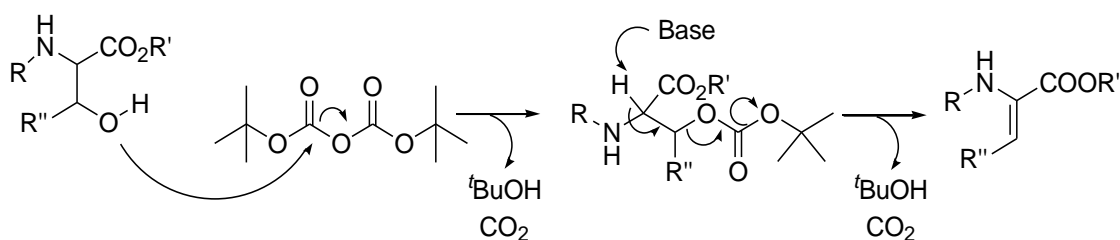
SCHEME 3. DEHYDRATION OF B-HYDROXYAMINO ACID DERIVATIVES WITH BOC$_2$O/DMAP AND TMG.

The dehydrodipeptide **7** was obtained in 39% yield. Figure 26 shows the proton NMR in CDCl$_3$ of compound **7**.
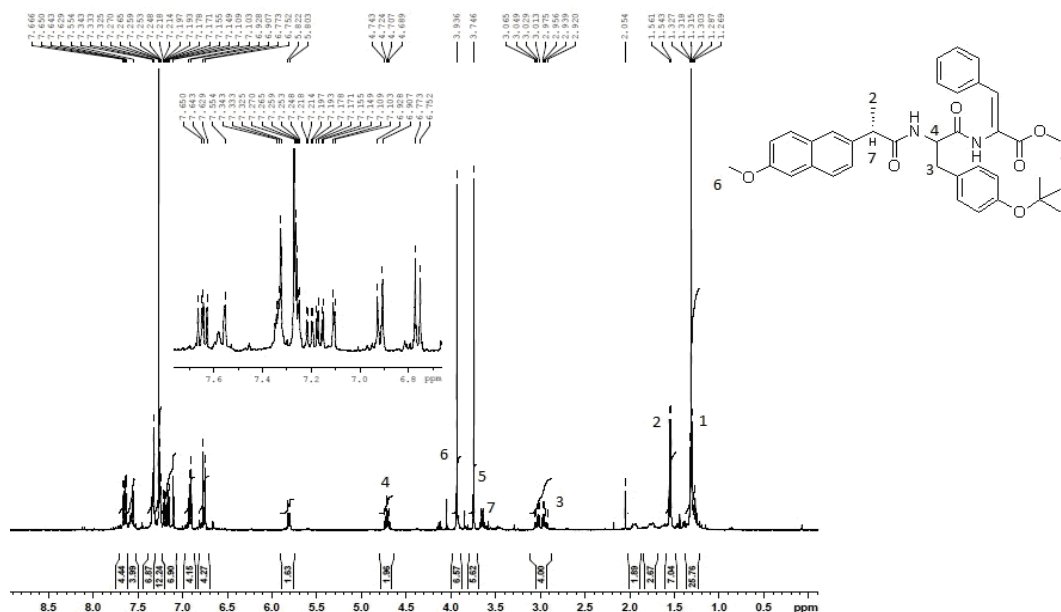
FIGURE 25. ¹H NMR SPECTRUM OF COMPOUND **7** IN CDCL₃.

The *tert*-butyl group of the dehydrodipeptide **7** was removed with trifluoroacetic acid (TFA) giving compound **8**. Basic hydrolysis of the methyl ester afforded the *C*-deprotected dehydrodipeptide Npx-Tyr-ΔPhe-OH, **1**. In the proton NMR spectrum of compound **1** in DMSO-*d₆* (Figure 27) it is possible to observe two singlets at 9.17 ppm and 9.60 ppm due to the OH proton of tyrosine and to the NH proton of dehydrophenylalanine and the absence of the signals at 1.31 ppm and 3.73 ppm assigned to CH₃ protons of the *tert*-butyl group and of the methyl ester, respectively.
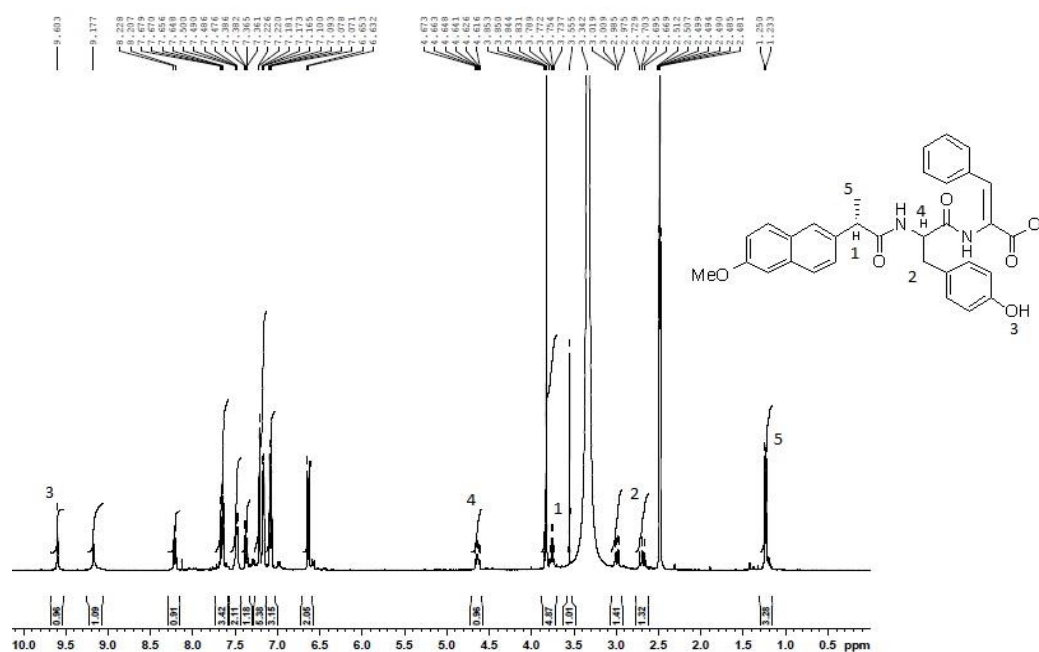
FIGURE 26. ¹H NMR SPECTRUM OF COMPOUND **1** IN DMSO-D₆.

The dehydrodipeptide **2** was prepared using a strategy similar to that described for compound **1** (Scheme 4). Thus, the *tert*butyl ester of *N*-fluorenylmethoxycarbonyl aspartic acid [Fmoc-L-Asp(O^{t}Bu)-OH, **9**] was coupled with the methyl ester of β-hydroxyphenylalanine (**4**) to give the dipeptide **10** as a diastereomeric mixture, in 66% yield. This compound was treated first with piperidine to remove the Fmoc group followed by naproxen chloride and triethylamine. The dipeptide N-capped with naproxen was dehydrated to give the Z-isomer of dipeptide Npx-L-Asp(O^{t}Bu)-*Z*ΔPhe-OMe, **12**. Removal of the *tert*butyl ester with TFA afforded compound **2**.
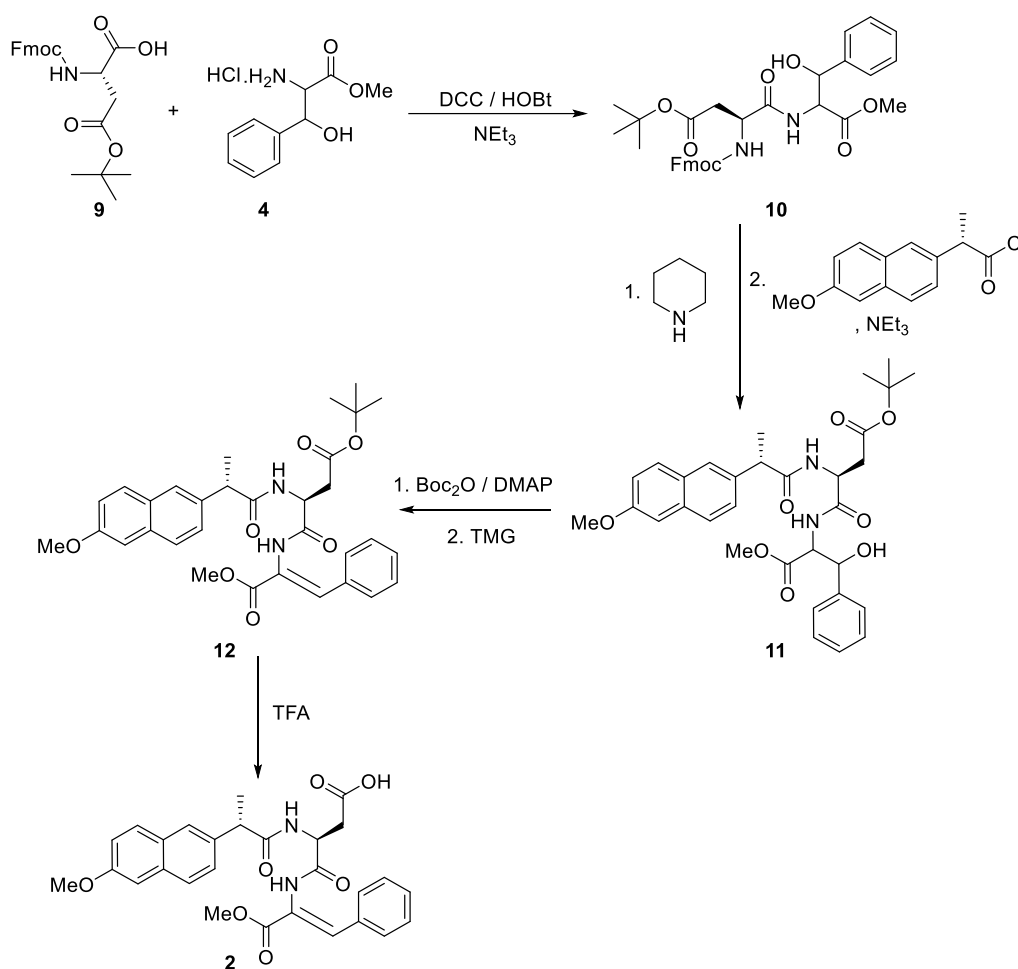
SCHEME 4. SYNTHESIS OF THE DEHYDROPEPTIDE NPX-L-ASP-Z-ΔPHE-OME, **2**.

Figure 28 shows the ^{1}H NMR spectrum of compound **2** in DMSO-d_6. The β-protons of aspartic acid appear as a doublet of doublets between 2.54 ppm and 2.77 ppm. The carboxylic acid proton appears at 12.37 ppm as a broad singlet.

The stereochemistry of compounds **1** and **2** was confirmed by Nuclear Overhauser (NOE) difference experiments by irradiating the α-NH proton of the dehydroamino acid residue and observing NOE enhancements in the signals of the β-phenyl protons.
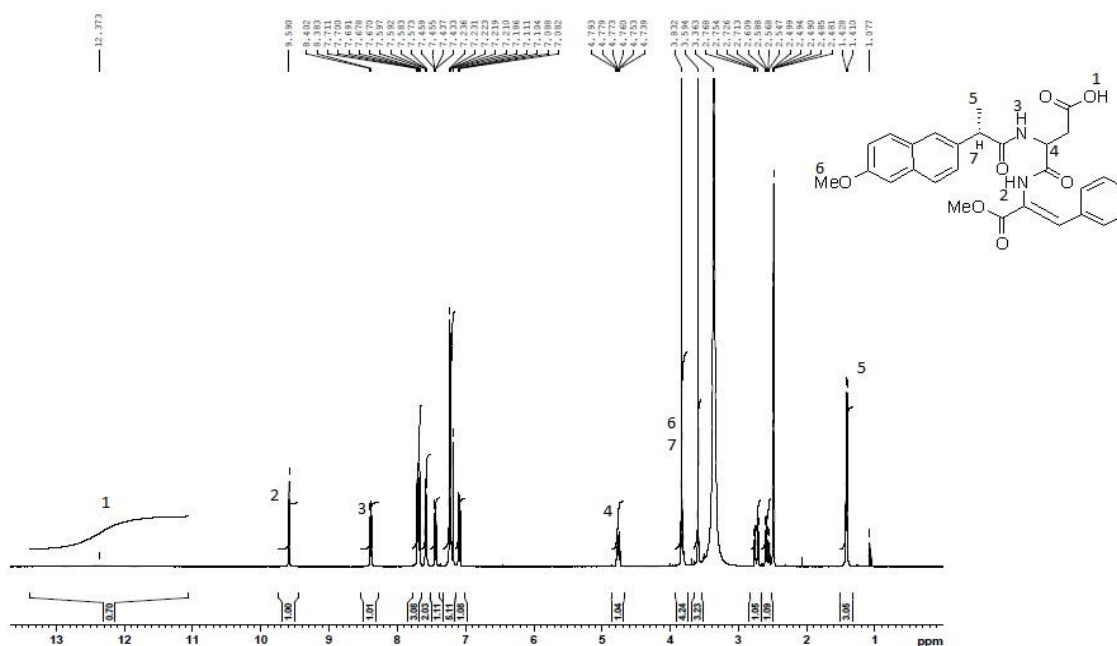
FIGURE 27. ^{1}H NMR SPECTRUM OF COMPOUND **2** IN DMSO-D$_6$.

The dehydrodipeptides **1** and **2** were used to prepare hydrogels.

Preparation of hydrogels

With dehydrodipeptides **1** and **2** in hand, different methodologies were tested for obtaining molecular hydrogels via self-assembly in solution. The solubility of hydrogelators **1** and **2** in buffer solutions (pH 4-8) was very low, both at rt and at 60 °C. Dehydrodipeptides **1** and **2** were dissolved in water upon pH adjustment to 10−11 with NaOH 1 M. Gel formation was attained by slow pH dropping triggered by hydrolysis of added D-glucono-δ-lactone (GDL) (Figure 29, Table I). When compared with other N-capped dehydrodipeptide hydrogelators with a dehydrophenylalanine residue it is possible to conclude that in all cases gelation is triggered via pH change. The critical gelation concentration (cgc) of hydrogelators **1** and **2** is similar to those observed for other *N*-protected dehydrophenylalnine hydrogelators and the gel-sol phase transition pH (pHgs) is identical to that observed for the tryptophanyldehydrophenylalanine hydrogelator and lower than those of phenylalanyldehydrophenylalanine and valinyldehydrophenylalanine hydrogelators (Figure 30). [3], [5]
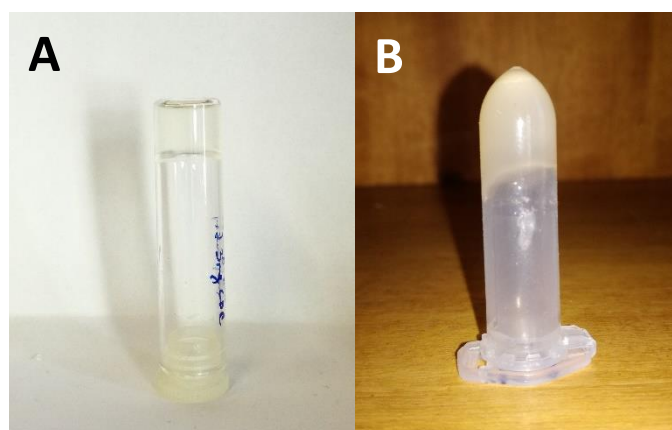
FIGURE 28. OPTICAL IMAGES OF HYDROGELS **1** AND **2**. A - DEHYDRODIPEPTIDE **1** (0.4WT%) B - DEHYDRODIPEPTIDE **2** (0.4WT%).

Npx-L-Phe-Z-ΔPhe-OH[5]
Cgc 0.4 wt%; pH 8.0

Npx-L-Val-Z-ΔPhe-OH[5]
Cgc 0.6 wt%; pH 8.0

Npx-L-Trp-Z-ΔPhe-OH[3]
Cgc 0.4 wt%; pH 5.68
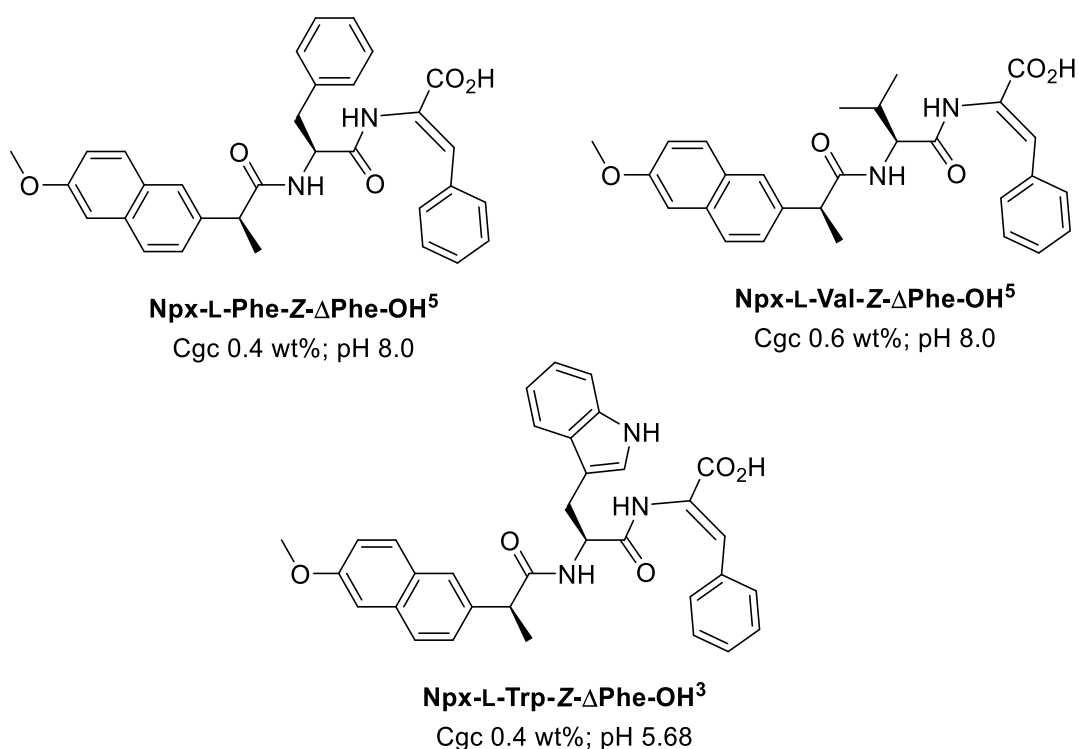
FIGURE 29. CRITICAL GELATION CONCENTRATION (CGC) AND SOL-GEL PH VALUES OF DEHYDROPHENYLALANINE DIPEPTIDE HYDROGELATORS *N*-PROTECTED WITH NAPROXEN REPORTED IN THE LITERATURE. [3], [5]

Peptide hydrogels derived from self-assembly of hydrogelators **1** and **2** were rendered magnetic by incorporation of superparamagnetic iron oxide nanoparticles (SPIONs) stabilised with polyacrylic acid. Magnetic self-assembled peptide hydrogels are proposed in this work as novel CA for MRI and for hyperthermia-triggered drug delivery. Preparation of hydrogels from peptides **1** and **2** loaded with SPIONs was accomplished using a similar methodology but adding the nanoparticles to the water suspension of the hydrogelator followed by pH adjustment to 10-11 with NaOH 1M. Gel formation was triggered by addition of GDL (Figure 31). Table I summarizes the

optimized conditions for gelation of dehydropeptides **1** and **2** without and with SPIONs.

TABLE I. OPTIMIZED CONDITIONS FOR GELATION OF DEHYDROPEPTIDES **1** AND **2** WITH AND WITHOUT SPIONS.

Peptide	Critical gelation concentration (cgc , wt%)	GDL Concentration (wt%)	pH
1	0.4	0.3	6.0
1 + 10 % or 20 % or 30 % of SPIONs	0.8	0.3	6.0
2	0.4	0.3	5.6
2 + 10 % or 20 % or 30 % of SPIONs	0.8	0.3	5.8
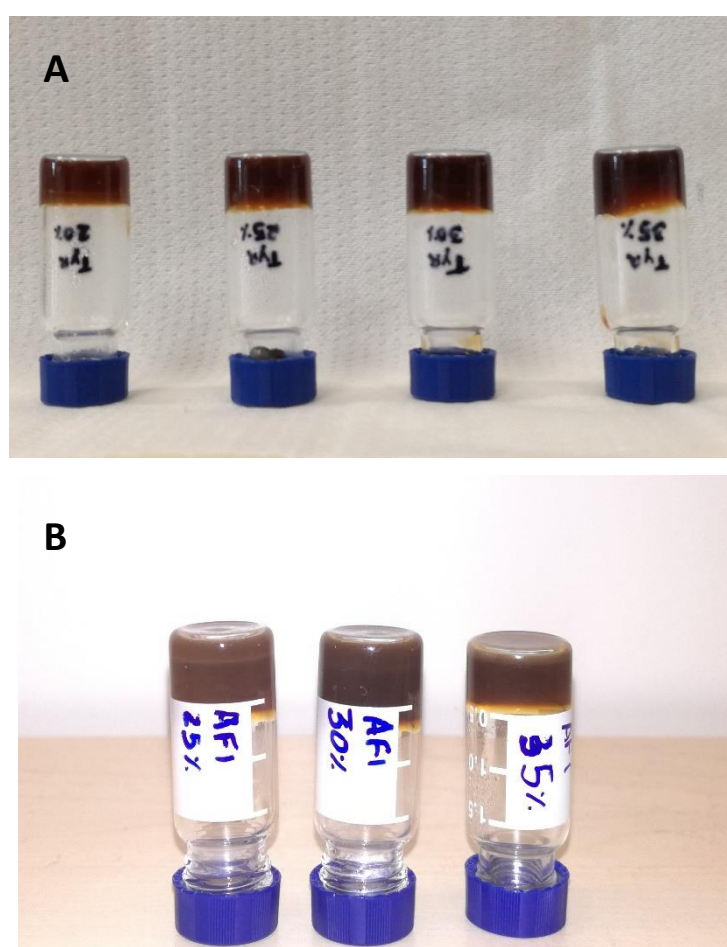
FIGURE 30. OPTICAL IMAGES OF HYDROGELS **1** AND **2** WITH SPIONS. A) DEHYDRODIPEPTIDE **1** (0.8 WT%) WITH 20%, 25%, 30% AND 35% OF SPIONS; B) DEHYDRODIPEPTIDE **2** (0.8 WT%) WITH 25%, 30% AND 35% OF SPIONS.

Both hydrogelators **1** and **2** display a critical gelation concentration of 0.4 wt%, of the same order of magnitude as that found for other dehydrodipeptide hydrogelators studied before in the research group.[5]   The introduction of *N*-terminal amino acid residues (Tyr and Asp) with ionisable polar side chains, seems not to have a critical effect on hydrogelator self-assembly.

Modelling and dynamic simulation studies identified before π-π stacking interactions of the aromatic naphthalene group of the naproxen moiety as the main contribution to self-assembly.[3]

As shown in Figure 31 we were able to prepare hydrogels with hydrogelators **1** and **2** (0.8 wt%) incorporating SPIONs in the concentration range 25-30% (m/m, in relation to hydrogelator weight). The incorporation of SPIONs into the hydrogels (0.8 wt%) results in slower gelation kinetics and weaker gels (see section on gel rheology) comparing to the hydrogels without SPIONs. The hyperthermia studies (see section on magnetic hyperthermia) required SPIONs in the concentration range 20-35 %. For comparasion purposes, we have chosen to carry out all studies with both hydrogels **1** and **2** at 8 wt% hydrogelator concentration.

Characterisation of SPIONs

Peptide hydrogels derived from self-assembly of hydrogelators **1** and **2** were rendered magnetic by incorporation of water colloidally stabilised superparamagnetic iron oxide nanoparticles (SPIONs) coated with a polyacrylic acid (PAA) organic shell.

The SPIONs used in this work were prepared and characterized by the group of Dr. Manuel Bañobre at the International Iberian Nanotechnology Laboratory (INL). Selected physicochemical and structural properties of the SPIONs, relevant for biomedical applications, are summarized in table II (figure 32).
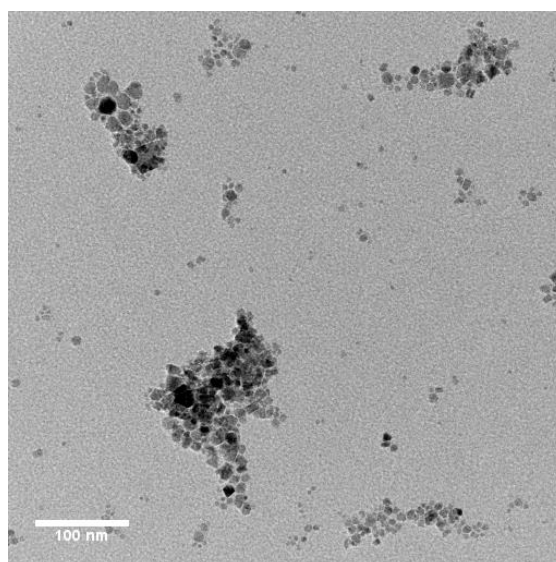
FIGURE 31. TEM IMAGE OF SPIONS PREPARED BY MANUEL BAÑOBRE'S GROUP AND USED IN THIS WORK. SCALE BAR 100 NM.

TABLE II. Properties of the SPIONs relevant for biomedical applications.

Composition	Core size (nm)	Hydrodynamic Diameter (HD) (HD; nm)	Zeta potential (mV)	Saturation Magnetisation (M_s; emu/g)
Fe_3O_4 Magnetite	8	108	-87.2	88.9

The PAA shell is fundamental to ensure colloidal stability of the nanoparticles preparation. The strong negative zeta potential of the nanoparticles (-87.2 mV at pH 7.0) results from ionization of the carboxylic acid groups on the PAA shell. The nanoparticle preparation is expected to display high colloidal stability at physiological pH due to inter-particle electrostatic and steric repulsion. The hydrodynamic diameter of the nanoparticles, much higher than the nanoparticle core size, reflects the thickness of the PAA shell and interactions of the ionised carboxylic acid groups with the solvation atmosphere. [34] Besides nanoparticle stabilisation, the PAA shell allows further functionalization of the nanoparticles, for example for targeting purposes. [14]

The core size of the nanoparticles, 8 nm, ensures that the nanoparticles are in the superparamagnetic regime at room temperature, which is fundamental to the applications proposed for the magnetic hydrogels- as CA for MRI and magnetic hyperthermia. The saturation magnetization, Ms is within the range expected for magnetite particles with this core size and composition (magnetite). [19], [24]

Magnetic self-assembled peptide hydrogels are proposed in this work as novel contrast agents for magnetic resonance imaging (MRI) and for magnetic hyperthermia (MH)-triggered drug delivery.

TEM studies

The micro- and nanostructure structure of hydrogels **1** and **2** was studied by transmission electron microscopy (TEM). Images were obtained from diluted solutions of hydrogelators **1** and **2** prepared under the set of conditions devised for hydrogel preparation. Due to the negligible electron density characteristic of purely organic samples, a staining with uranyLess was used to visualize the micro-nano-structure of the hydrogels (Figure 33).
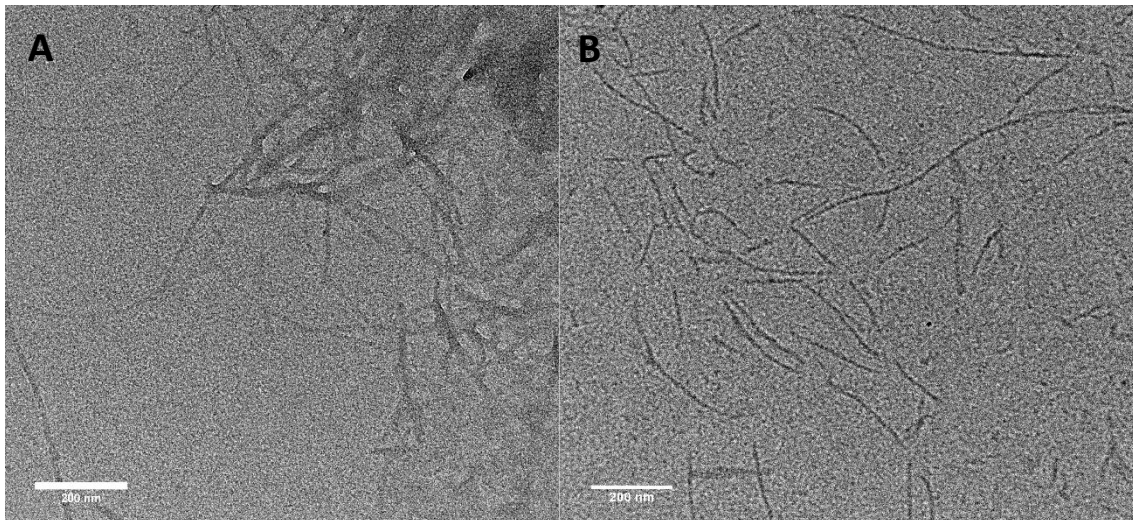
FIGURE 32. TEM IMAGES OF DEHYDRODIPEPTIDE **1** AND **2** OBTAINED WITH URANYLESS STAIN: A - DEHYDRODIPEPTIDE **1** (0.08WT%); B - DEHYDRODIPEPTIDE **2** (0.08WT%). SCALE BAR 200NM.

Dehydrodipeptides **1** and **2** display an entangled fibril structure that is the result of peptide self-assembly. Water gelation is the result of water trapping by the fibril network. In general, the fibres formed by dehydrodipeptide **1** (Figure 33A) displays a thickness around 10-20 nm and its length varies from approximately 0.2 to 0.4 μm. Dehydrodipeptide **2** (Figure 33B) shows fibres with diameters around10-20 nm and lengths between 70 nm and 0.8 μm.

Unfortunately, TEM images of both hydrogels containing SPIONs did not show enough quality to shed light into the distribution of the nanoparticles within the hydrogel and potential interactions with the fibrils. This part of the study constitutes a work in progress of the host research groups at UMinho and INL.

Circular Dichroism

Circular dichroism (CD) spectroscopy is a valuable tool for rapidly evaluate the secondary structure, folding and binding properties of peptides and proteins. This technique has two major advantages: it is possible to carry out measurements using small amounts of material in physiological buffers and is one of the best methods to observe structural alterations elicited by changes in pH, temperature or ionic strength. CD can be defined as the unequal absorption of left-handed and right-handed circularly polarized light. In the case of peptides when the chromophores of the amides are aligned in arrays, their optical transitions are shifted or split into multiple transitions due to "exciton" interactions. The result is that different structural elements have characteristic CD spectra (Figure 34). Thus, α-helical peptides have negative bands at 222 nm and

208 nm and a positive band at 193 nm. Peptides with well-defined antiparallel β-sheets have negative bands at 218 nm and positive bands at 195 nm, while a random coil peptides show low ellipticity above 210 nm and negative bands near 195 nm.[51]
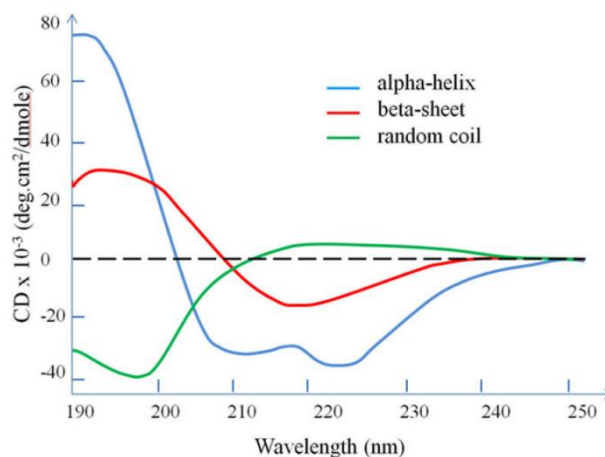
FIGURE 33. STANDARD CD SPECTRA OF THE THREE BASIC SECONDARY STRUCTURES OF PEPTIDES FROM CORRÊA ET AL.[52]

Circular dichroism (CD) spectra were acquired with solutions of hydrogelators **1** and **2** prepared in the same conditions as those used for TEM studies (Figure 35). SPIONs impart a strong dark colour to the hydrogelator solutions and also to the resulting hydrogels, which result too opaque for an optimal CD spectra acquisition. In order to minimize this issue as much as possible, CD spectra were acquired with solutions with hydrogelator concentrations much lower than the cgc: ≈ 200 and ≈ 500 fold dilutions of both non-magnetic and magnetic hydrogels incorporating SPIONs, respectively. Glucono-δ-lactone was added to the hydrogelator solutions, to simulate the experimental conditions of gel formation. Under these experimental conditions it is likely that the hydrogelator concentration is above the critical aggregation concentration (cac) with formation of hydrogelator fibres in solution.
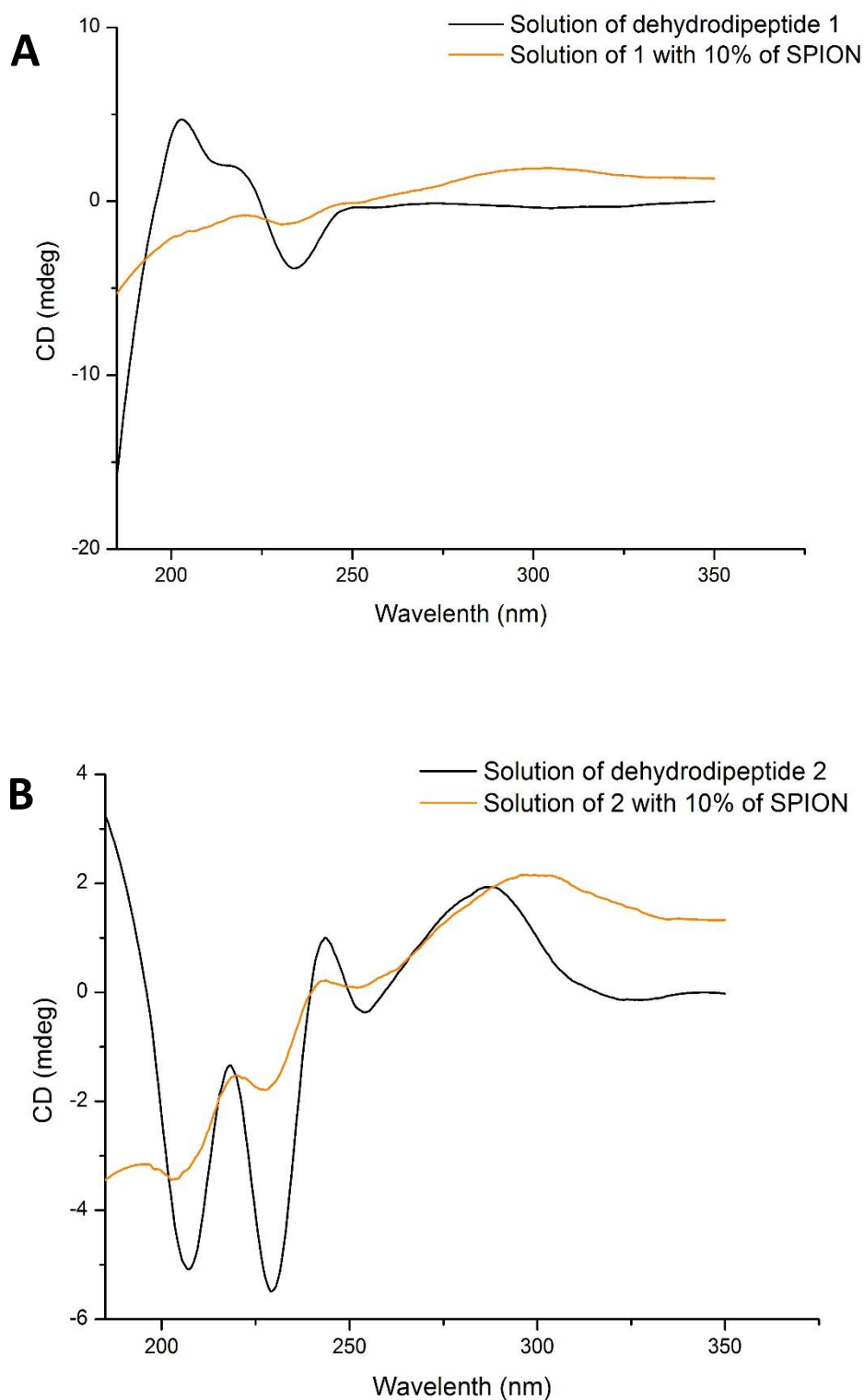
FIGURE 34. CD SPECTRA OF DILUTED AQUEOUS SOLUTIONS OF DEHYDROPEPTIDES **1** (A) AND **2** (B) WITHOUT (0.004 WT%) AND WITH 10 % SPIONS (0.0016 WT%).

The hydrolysed GDL (gluconic acid), is CD silent above 200 nm but active below 200 nm and potentially can interfere with the CD signal of the peptide $\pi-\pi^*$ transition. The CD spectrum

of Npx-L-Tyr-Z-ΔPhe-OH, **1** exhibits bands around 200 nm and 220 nm (positive peaks) and 230 nm (broad negative peak) (Figure 35 A). The CD spectrum of Npx-L-Asp-Z-ΔPhe-OMe, **2** shows a positive band below 200 nm, two negative bands at 210 nm and 230 nm and a positive broad peak around 280 nm (Figure 35 B). Addition of SPIOs to solutions of hydrogelators **1** and **2** results in broadening of the spectra, although the general features of CD spectra seem unchanged. With these data, it was impossible to establish the arrangement of the dehydrodipeptide molecules in the fibres. Thus, Fourier-Transformed Infrared (FTIR) spectroscopy was used to get more information about the secondary structure of the self-assembled dehydropeptides.

FTIR is a spectroscopic technique widely used for characterizing organic molecules. Excitation of specific molecular vibrational modes can be achieved in FTIR by irradiation with infrared light. Vibrational signatures can be assigned to specific vibrational modes of functional groups. In addition, every molecule displays an ensemble of characteristic coupled molecular vibrations (generally below 1300 cm^{-1}) that constitutes its *finger print*. The peptide nature of hydrogelators makes the vibrational signature of the amide bond especially relevant for molecular characterization purposes and for characterization of intermolecular interactions. The effect of gelation on the amide I and II bands can give valuable information regarding intermolecular hydrogen bonding and secondary structure features of self-assembled peptide molecules. The amide I band (1650 cm^{-1}) represents the C=O stretching vibration of the amide group coupled to the in-plane N–H bending and C–N stretching modes. The amide II (1567 cm^{-1}) represents mainly the N–H bending with some C–N stretching contribution. The most useful infrared band for the analysis of the secondary structure of peptides in aqueous media is the amide I band. [53] The amide I band is a combination of several bands representing the secondary structure of peptides (helix, β-structures and random coil) (Table III).[53]The deconvolution of this band allows the identification of various structures present in a peptide. Figure 36 shows this approach for lysozyme.[53]

TABLE III. CHARACTERISTIC AMIDE I BAND ASSIGNMENTS OF PEPTIDE SECONDARY STRUCTURE (FROM STUART, B.H).[53]

Wavenumber cm^{-1}	Assignment
1695 – 1670	Intermolecular β-structure
1690 - 1680	Intramolecular β-structure
1666 - 1659	β-Turn
1657 – 1648	α-Helix
1645 - 1640	Random coil
1640 - 1630	Intramolecular β-structure
1625 – 1610	Intermolecular β-structure
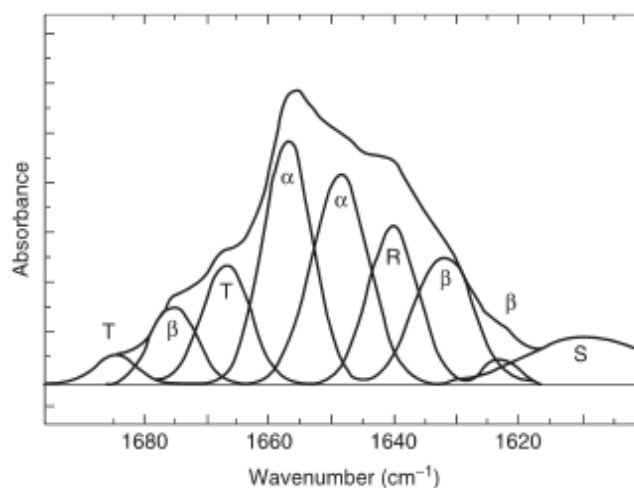
FIGURE 35. CURVE-FITTED AMIDE I BAND OF LYSOZYME IN D$_2$O REDRAWN FROM STUART B.H.[53]

FTIR spectra were recorded for compound **1**, for the hydrogel obtained from compound **1** and for hydrogels obtained from compound **1** loaded with different amounts of SPIONs (Figure 37).
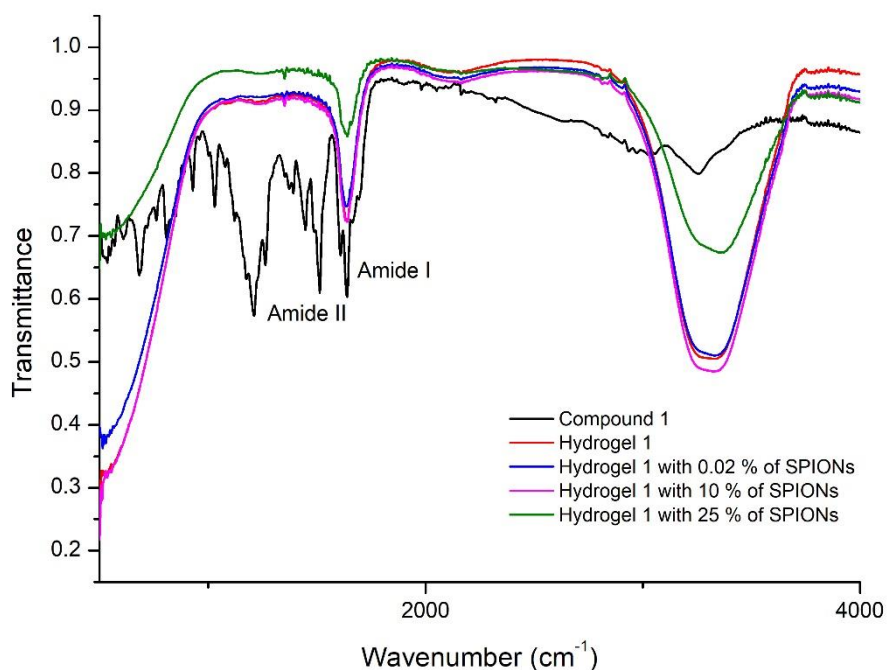
FIGURE 36. FTIR SPECTRA OF COMPOUND **1**, OF HYDROGEL **1** AND OF HYDROGEL **1** LOADED WITH SPIONS.

The FTIR spectrum of compound **1** shows well defined vibrational bands. The band at 1649 cm^{-1}- 1624 cm^{-1} can be identified as the signature of the peptide amide I bond vibration. The band at 1517 cm^{-1} can be assigned to the amide II vibrational signature. In the hydrogel phase without or with different amounts of SPIONs it is possible to observe very broad features with the disappearance of amide II band.

Figure 38 shows the deconvolution of the amide I band of the self-assembled compound **1** molecules without and with SPIONs.
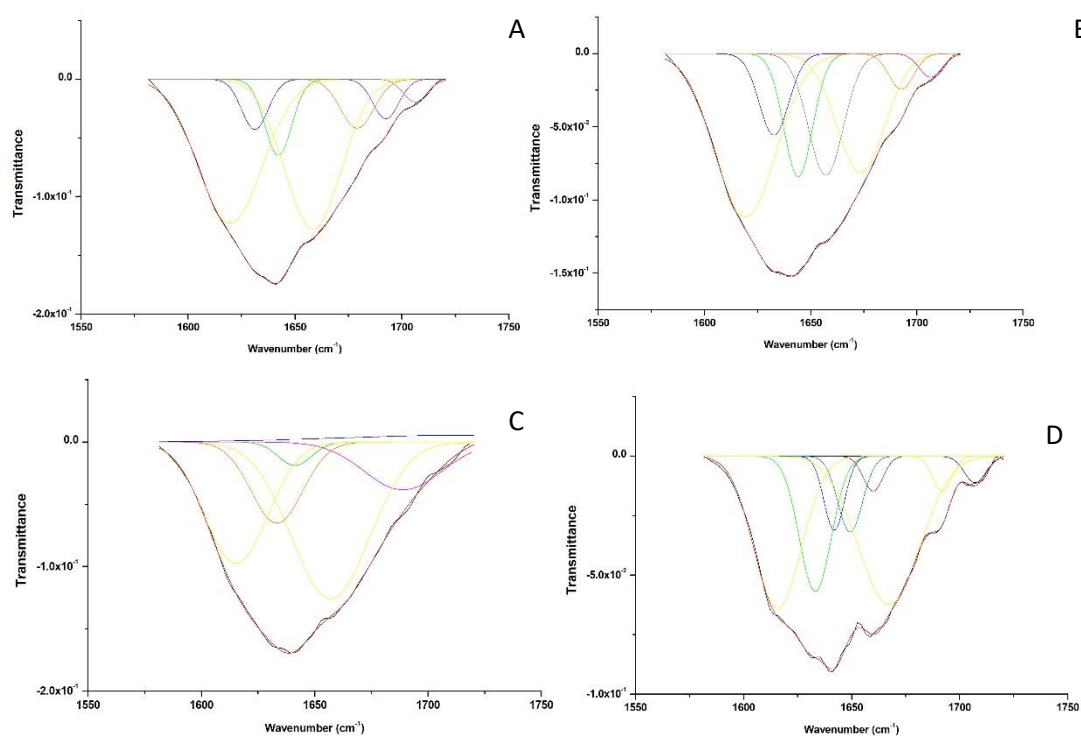
FIGURE 37. DECONVOLUTION OF THE VIBRATIONAL AMIDE I BAND SIGNATURE OF HYDROGEL **1** (A) AND OF HYDROGEL **1** WITH INCREASING AMOUNTS OF SPIONS (B-D).

According to the results obtained the hydrogel obtained from the hydrogel **1** and from the hydrogels of **1** with different amounts of SPIONs seem to have a predominant β-sheet secondary structure.

Rheology

The rheological properties of the hydrogels are fundamental for biological applications, especially for magnetic hyperthermia-mediated drug delivery applications purposed in this work.

The rheological properties of hydrogel **1**, without SPIONs and with SPIONs [10, 25 and 30% (m/m)] were studied by oscillatory rheology. The structural buildup of the gels, upon addition of GDL, was followed by rotational rheometry (Figure 39). A small amplitude sinusoidal shear at a frequency of 1 Hz was applied to the samples and the corresponding sinusoidal stress transmitted by the sample was measured.
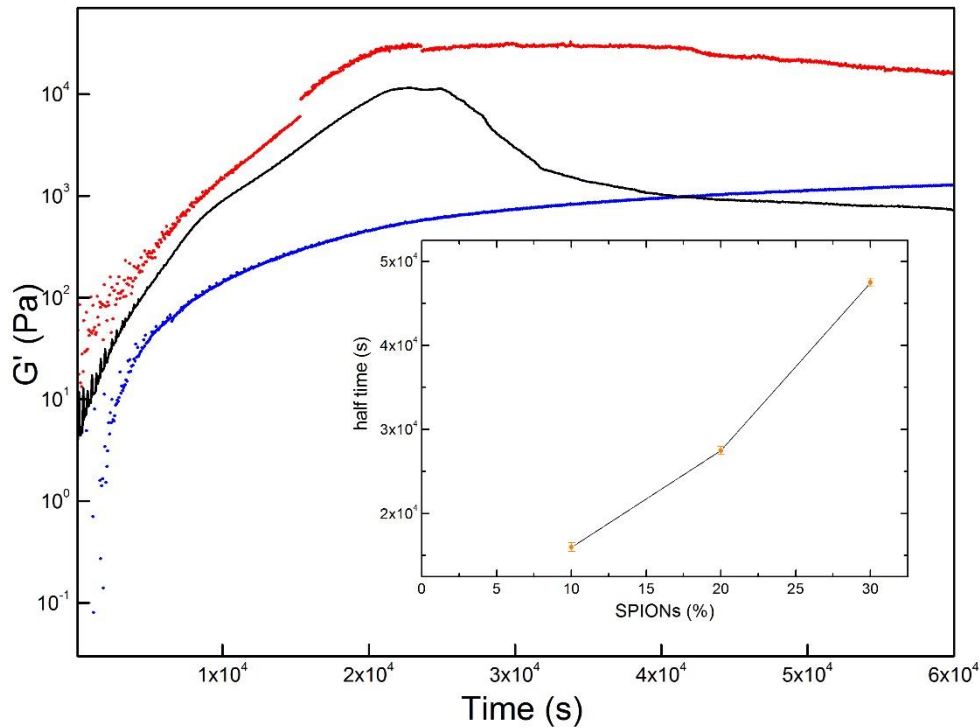
FIGURE 38. TIME EVOLUTION OF THE STORAGE MODULUS G' OF SAMPLES FORMULATED WITHOUT (RED: DATA MEASURED WITH 0.001% STRAIN; BLACK: DATA MEASURED WITH 0.01% STRAIN) AND WITH 20 % SPIONS (BLUE). INSET: EFFECT OF NP CONTENT OF THE HALF TIME FOR GEL STRUCTURAL BUILDUP.

The incorporation of SPIONs into hydrogel **1** results in slower structural buildup. A negative correlation between the rate of gelation and the concentration of SPIONs is observable (inset Figure 39).

Mechanical spectra for equilibrated gels are presented in Figure 40 (Table IV).
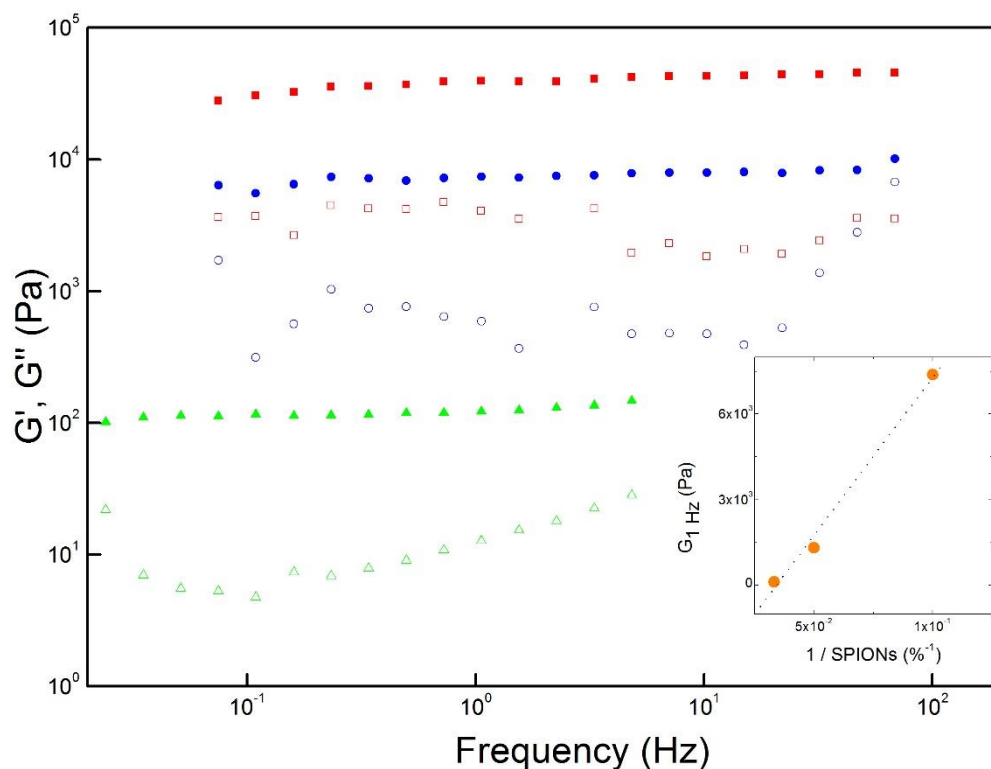
FIGURE 39. MECHANICAL SPECTRA (SOLID SYMBOLS: G'; EMPTY SYMBOLS: G'') OF DEHYDROPEPTIDE **1** (0.8 WT%) (RED SQUARES) AND DEHYDROPEPTIDE **1** WITH INCORPORATED SPIONS; 10% SPIONS (BLUE CIRCLES) AND 30% SPIONS (GREEN TRIANGLES). INSET: EFFECT OF SPIONS CONTENT ON THE GEL ELASTIC MODULUS MEASURED AT 1 HZ, G_{1Hz}

TABLE IV. G' AND G'' FOR HYDROGEL **1** AND HYDROGEL **1** WITH SPIONS.

Hydrogel	G' (Pa)	G'' (Pa)
1	3.93×10^4	4.07×10^3
1 with 10% SPIONs	7.3×10^3	5.93×10^2
1 with 30% SPIONs	1.22×10^2	12.2

Hydrogel obtained from dehydrodipeptide **1** (0.8 wt%) has higher G' and G'' values when compared with other hydrogels obtained from dehydrodipeptides already studied in our research group.[5] Thus the hydrogels obtained from the dehydrodipeptides phenylalanyldehydrophenylalanine (0.4 wt%) and valinyldehydrophenylalanine (0.6 wt%) N-capped with naproxen have G' values of 1.7×10^3 Pa and 6.6×10^2 Pa, respectively.[5] This suggests the existence of a more resilient network of fibers in the hydrogel obtained from **1**. All hydrogels obtained from **1** without and with SPIONs present a shear elastic modulus (G') significantly higher than their loss modulus (G'') which indicates a viscoelastic behavior. The incorporation of SPIONs into the hydrogel modulates the structure of the gel as the minimum in the frequency dependence

of the shear loss modulus G'' is shifted to smaller frequencies upon addition of nanoparticles. This means that the longest relaxation process in the gel slows down due to the presence of SPIONs. This result is in agreement with the delayed structural buildup induced by incorporation of increasing concentrations of SPIONs into the hydrogel (Figure 39). Moreover, SPIONs weaken gel elasticity since the shear elastic modulus (G') decreases with increasing SPIONs content (inset to Figure 40). The gap between the shear elastic modulus (G') and the shear loss modulus (G'') increases with increasing content of SPIONs, suggesting an enhancement of viscous contributions to the gels mechanical response.

The TEM studies show that the hydrogels are made of bundles of entangled fibers formed by hydrogelator self-assembly (Figure 33). Assuming that gel elasticity is determined by interactions between the fibers instead of nanoparticle-nanoparticle contacts, the picture emerging from the rheological data is that the incorporation of SPIONs into the hydrogel leads to swelling of the mesh size of the structure which slows down the formation of elastically effective fiber-fiber contacts.

Alternatively, if one assumes that the mesh size remains constant, the linear dependence of G_{1Hz} on the inverse of the SPIONs content (inset Figure 40) is reminiscent of a stiffening effect of the fibers[54] in the presence of the nanoparticles.

A more detailed rheological study (including the behavior under large strain) on a wider range of SPIONs content would be needed to help unravelling the structural features of such gels.

Magnetic characterisation of hydrogels

The magnetic properties of both non-magnetic and magnetic hydrogels **1** and **2** were evaluated trough magnetic measurements in a superconducting quantum interference device (SQUID) magnetometer as a function of the temperature (5-300K) and applied magnetic field (up to ±2T). (Figure 41).
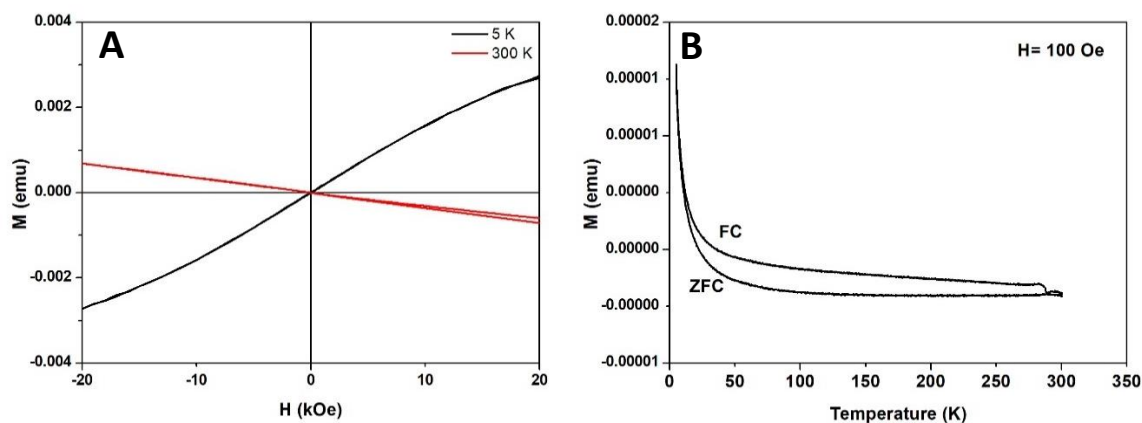
FIGURE 40. MAGNETIC CHARACTERIZATION OF HYDROGEL **2**: A) HYSTERESIS LOOP AT 5 AND 300K; B) *ZFC-FC* MAGNETIZATION CURVES FOR HYDROGEL **2** (0.8 WT%).

Figure 40-A shows the hysteresis loops (magnetization (M) *vs* applied magnetic field (H)) at 300 and 5K for the hydrogel **2** (0.8 wt%). Figure 40-B displays the temperature dependence of the magnetization under zero-field-cooling and field-cooling (ZFC-FC) conditions in the temperature range from 5 to 300K. In ZFC conditions the sample is cooled down from room temperature without an applied magnetic field and then the magnetization is measured as the temperature increases under an applied magnetic field. On the other hand, under FC conditions the sample is cooled down with an applied magnetic field (H=100 Oe in our case) and the magnetization is measured under this field as the temperature increases. Whereas the hysteresis loops allow us to identify the magnetic behaviour of the material (diamagnetic, paramagnetic, ferromagnetic, etc.) and magnetic parameters like coercive field, remanence and saturation magnetization, among others, from the ZFC-FC curves we can get further information about blocking temperature and magnetic dipolar interactions in collective magnetic systems, as those composed of nanoparticles. The hysteresis loop of the hydrogel **2** (0.8 wt%) at 300 K confirms the expected diamagnetic behaviour of the gel, in which the applied magnetic field creates a magnetization of opposite direction, causing a repulsive force. Diamagnetism is due to quantum mechanical effects and when there is no other magnetic contribution, these materials are called diamagnetic. As we decrease the temperature down to 5K, the weak diamagnetic force is overcome by the attractive force of the magnetic dipoles, in such a way that the magnetization increases 'linearly' with the applied magnetic field. This contribution has been confirmed to be extrinsic to the sample and come from the sample holder, which was composed of a conventional glass doped with magnetic transition metals. As we incorporate a 0.1% of magnetite nanoparticles in the hydrogel (Figure 42), the extra magnetic contribution coming from the nanoparticles is not enough to change the diamagnetic behaviour at

260 K, meaning that the diamagnetic contribution from the organic matrix of the hydrogel seems to dominate over the magnetic contribution of the SPIONS to the sample magnetism. The hysteresis loop at 5 K indicates a PM behaviour, although the absolute values the observed magnetization is higher than that of the non-magnetic gel, as expected from the extra magnetic contribution of the nanoparticles. However, as we increase the magnetic loading from 0.1 to 10% the magnetic behaviour at 260 K turns clearly superparamagnetic, as consequence of the higher magnetic signal due to the SPIONs that now overcomes the diamagnetic signal of the gel. This superparamagnetic behaviour is typical of magnetite nanoparticles of small size.[19], [24] Superparamagnetism comes from a ferromagnetic (FM) spin interaction under an applied magnetic field (the magnetic spins orientate in the direction of the applied magnetic field). However, as the average particle size of the SPIONs used as magnetic loading in the dehydrodipeptides solutions is well below the single-to-multi domain critical size (in magnetite around 20-25 nm), the magnetic nanoparticles behave as superparamagnets rather than ferromagnets, conversely showing zero coercive field and remanence, indicated by the absence of hysteresis of the magnetization curve and the negligible net magnetization at zero field, respectively. Nonetheless, the decrease of the magnetization at high magnetic fields still shows a significant diamagnetic contribution of the organic matrix to the overall paramagnetism. As we decrease the temperature down to 5 K, a FM-like contribution ($H_c=$ 210 Oe) is indicated by an open hysteresis loop due to the presence of a magnetically blocked state. Moreover, a PM contribution is observed to be overlapped to the superparamagnetism, being dominant and resulting in an additional linear increase of the magnetization at high applied fields. The ZFC-FC magnetization curves confirm the magnetic behaviour observed in the hysteresis loops. Whereas no significant differences are observed between the non-magnetic gel and that with 0.1% of MNPs, the increase of the magnetic loading up to 10 % induced a more relevant difference between the ZFC and the FC curves. Basically, whereas the ZFC and FC curves follow a PM decay with temperature in both non-magnetic and 0.1% magnetic gels, in the case of the 10% gel a more clear difference is observed between the ZFC and FC curves, which indicates a magnetic transition from a magnetic blocked state (FM-like behaviour) to a superparamagnetic state below and above the blocking temperature ($T_B=138$ K), defined as the maximum of the ZFC curve. T_B indicates the minimum temperature from which the thermal energy becomes sufficient to overcome the effect of the "strength" of the magnetic field on the magnetic moment orientation with respect to the magnetization easy directions of nanoparticles. Interestingly, also the divergence between the ZFC and the FC curves in the whole range of temperature up to 300 K is indicative of the strong

magnetic dipolar interactions between the magnetite nanoparticles in the gel network, which were negligible at the 0.1 % MNPs concentration.

Hydrogel **2** behaves in a similar way to hydrogel **1** (Figure 43): it displays dominant diamagnetic behaviour with 0.1 % concentration of incorporated SPIONs but becomes paramagnetic when the SPIONs concentration increases up to a 10%. The organic matrix of the hydrogel adds still a dominant diamagnetic contribution to the overall paramagnetic behaviour of the nanoparticles at high magnetic fields. The blocking temperature for hydrogel **2** is similar to that measured for hydrogel **1** (T_B=136 K).

In qualitative terms it is possible to infer that the structure of the hydrogelator molecules (aspartic acid or tyrosine residues) and of the micro- and nanostructure of the hydrogel fibres do not affect the distribution of the SPIONs inside the hydrogel matrix and, therefore, nor the magnetic dipolar interactions between them at this nanoparticle concentration (10 wt%).
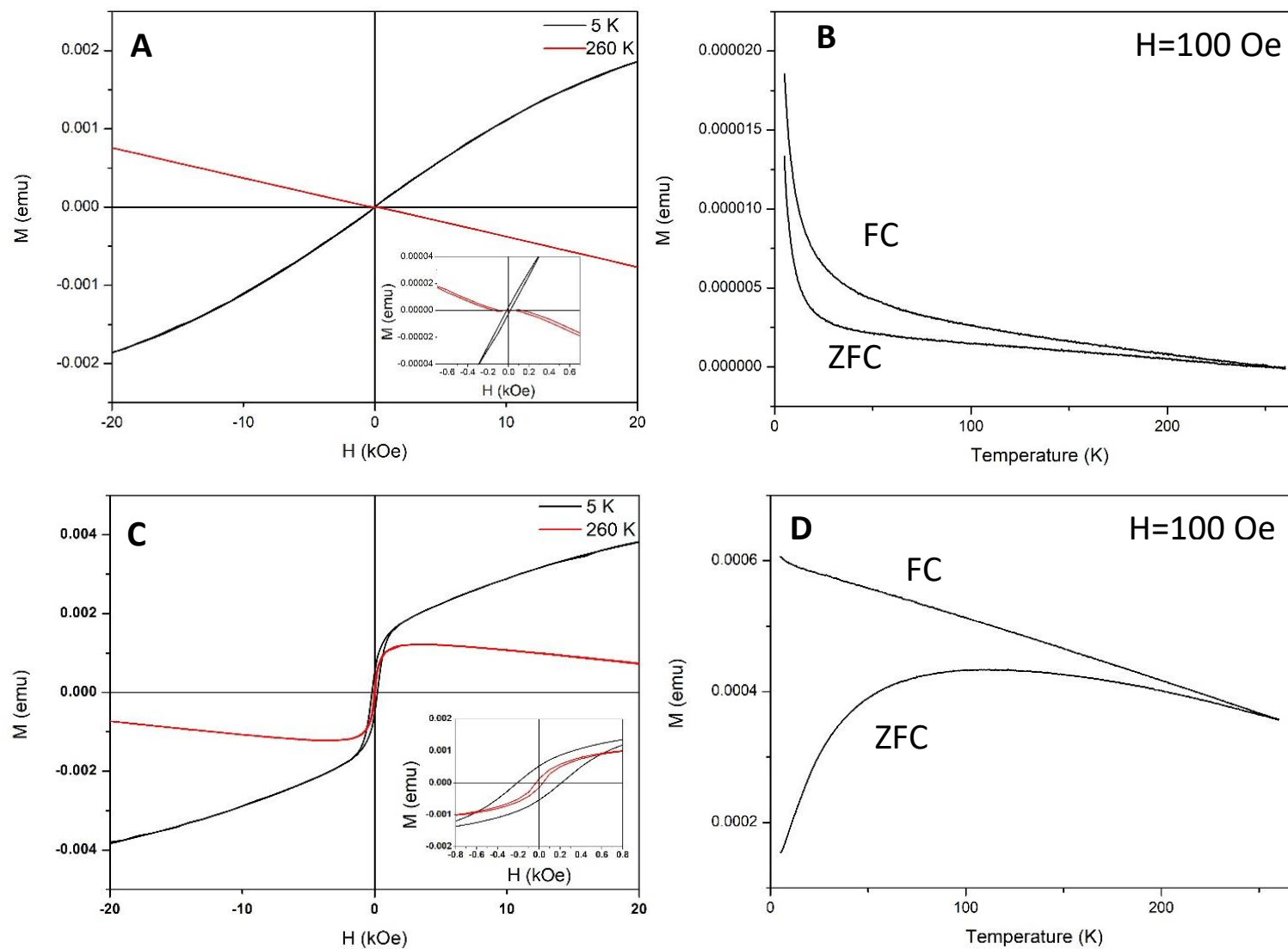
FIGURE 41. (A, C) Hysteresis loop at 5 and 260K of hydrogel **1** with 0.1% and 10% of incorporated SPIONs, respectively. (B,D) ZFC-FC magnetization curves of hydrogel **1** with 0.1% and 10% of incorporated SPIONs, respectively. Insets: High magnification at low magnetic fields.
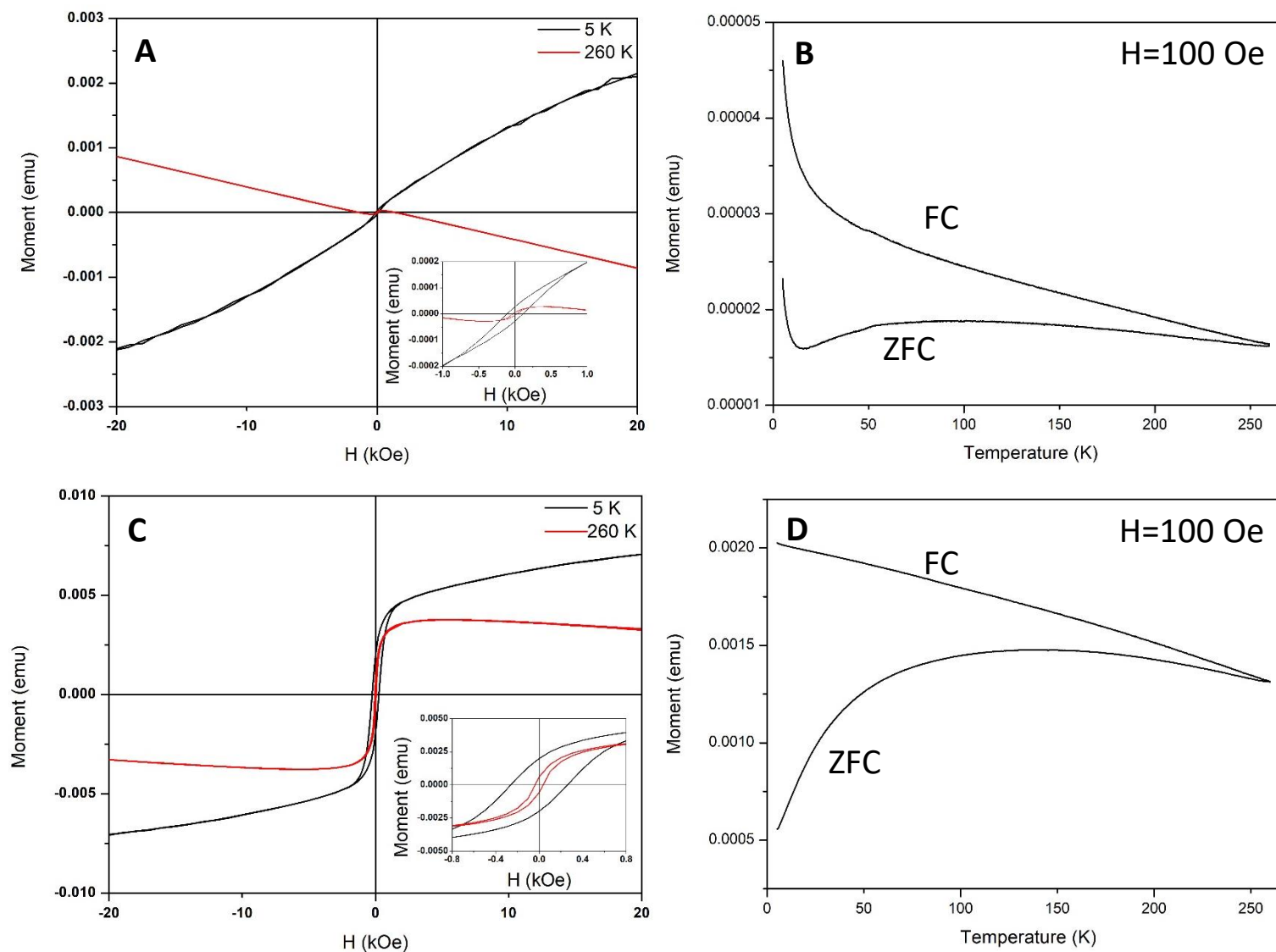
FIGURE 42. (A, C)Hysteresis loop at 5 and 260K of hydrogel **2** with 0.1% and 10% of incorporated SPIONs, respectively. (B,D) ZFC-FC magnetization curves of hydrogel **2** with 0.1% and 10% of incorporated SPIONs, respectively. Insets: High magnification at low magnetic fields.

Magnetic Resonance Imaging

It is well known that SPIONs around 10 nm of particle size preferentially reduce the transverse relation times (T_2) of the water protons resulting in dark images in magnetic resonance imaging (MRI), thus being considered as T_2-contrast agents.

In this work, the efficacy of the SPIONs as water paramagnetic relaxers was initially evaluated by MRI at 3 T and 25 °C (Figure 19) before incorporation in the developed hydrogels **1** and **2**.
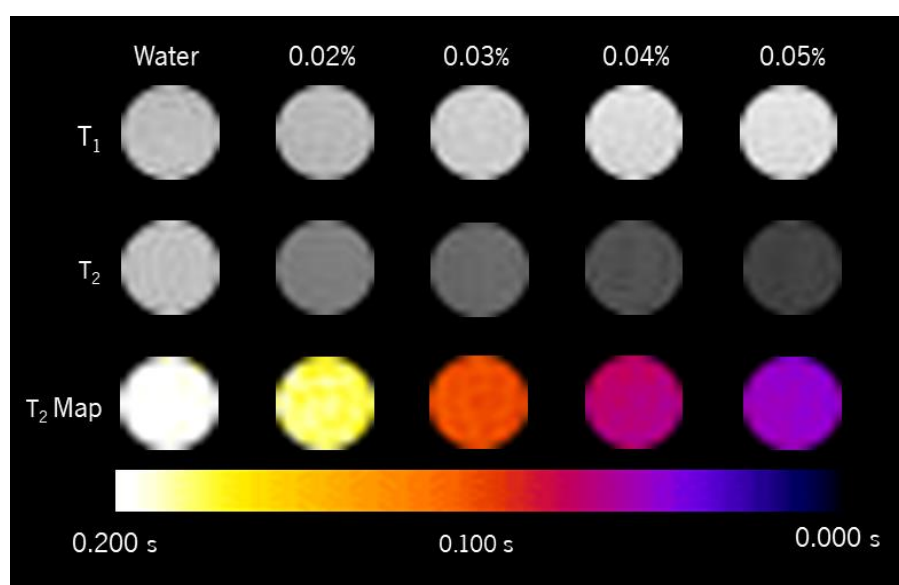
SPIONs % (m/v)	0.02	0.03	0.04	0.05
[Fe] (mM)	0.0716	0.1074	0.1433	0.1791
T_2 (s)	0.177	0.100	0.071	0.053
R_2 (s^{-1})	5.65	10.00	14.08	18.8

FIGURE 43. T_2 MRI RELAXATION MAP (3T, 25 °C) FOR THE SPIONs IN AQUEOUS SOLUTION.

The MRI T_2 relaxation map was acquired using the MEMS (multi-echo-multi-spin) sequence. The efficacy of the SPIONs as a paramagnetic water relaxer was evaluated by its transverse relaxivity, r_2 (equation 12, Figure 45).

$$R_{i(obs)} = \frac{1}{T_{i,0}} + r_i C \quad \text{(equation 12)}$$

$R_2 = 1/T_2$ (s^{-1}) represents the observed transverse relaxation rate of the water protons; $T_{2,0}$ (s) is the observed diamagnetic transverse relaxation time of water protons (measured before adding the paramagnetic species); r_2 (mM^{-1} s^{-1}) is the transverse relaxivity and C (mM) is the

concentration of the paramagnetic species (Fe).

Equation	y = a + b*x	
		Value
Relaxation rate	Intercept	-3.15816
	Slope	122.130
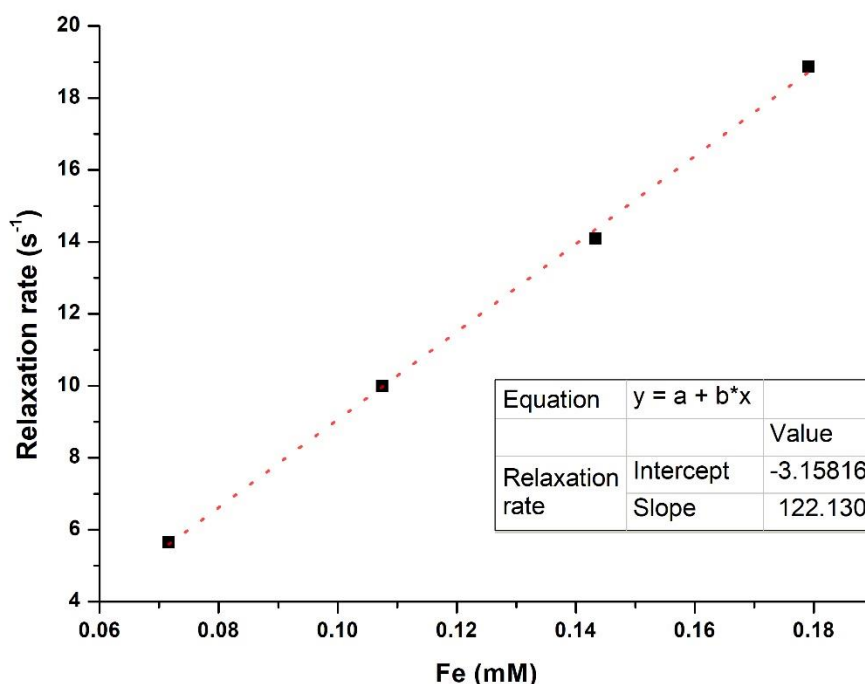
FIGURE 44. DEPENDENCE OF THE OBSERVED PARAMAGNETIC TRANSVERSE RELAXATION RATE (R_2; 3 T, 25 °C) ON THE FE CONCENTRATION OF THE SPIONS IN WATER SOLUTION.

The SPIONs display a substantial relaxivity, r_2= 122 mM^{-1}s^{-1}, comparable to that displayed by other materials with similar core size and magnetic composition that eventually made it into the clinics (i.e. Feridex, r_2= 120 mM^{-1}s^{-1}; r_1= 10.1 mM^{-1}s^{-1}; 1.5 T)[46]. The relaxivity of the SPIONs is likely limited by the small size of the magnetic core ($\approx$8 nm) and the inherent surface spin canting effects. Self-assembly/aggregation of the SPIONs can be excluded owing to steric and electrostatic repulsion effects derived from the net negative charge (zeta potential = -87.2 mV; pH 7.0, 25 °C) displayed by the nanoparticles in the physiological pH range.

SPIONs were incorporated into the hydrogel by adding an aqueous solution of SPIONs to alkaline hydrogelator solutions, followed by GDL addition (Figure 46).

FIGURE 45. PICTURE OF SELF-ASSEMBLED HYDROGELS CONTAINING SPIONS (0-0.06% (M/M)) FOR MRI MEASUREMENTS.

T_2 MRI relaxation maps (3 T, 25 °C) were acquired for self-assembled hydrogels of hydrogelators **1** and **2** containing SPIONs in the same concentration range as that studied in solution (Figure 47).

The relaxivity of the SPIONs incorporated into the hydrogels is strongly affected by the hydrogel matrix (Figure 48, Table V).

Hydrogelator 1 0.8 wt%	SPIONs % (m/m)	0	0.01	0.02	0.04
	[Fe] (mM)	0	0.0716	0.1433	0.2865
	T_2 (s)	0.436	0.259	0.140	0.095
	R_2 (s^{-1})	2.29	3.86	7.14	10.53

Hydrogelator 2 0.4 wt%	SPIONs % (m/m)	0	0.01	0.04	0.06
	[Fe] (mM)	0	0.0358	0.143	0.215
	T_2 (s)	0.612	0.306	0.107	0.053
	R_2 (s^{-1})	1.63	3.27	9.35	10.87

Hydrogelator 2 0.8 wt%	SPIONs % (m/m)	0	0.01	0.02	0.04
	[Fe] (mM)	0	0.0716	0.1433	0.2865
	T_2 (s)	0.215	0.101	0.086	0.06
	R_2 (s^{-1})	4.65	9.90	11.63	16.67
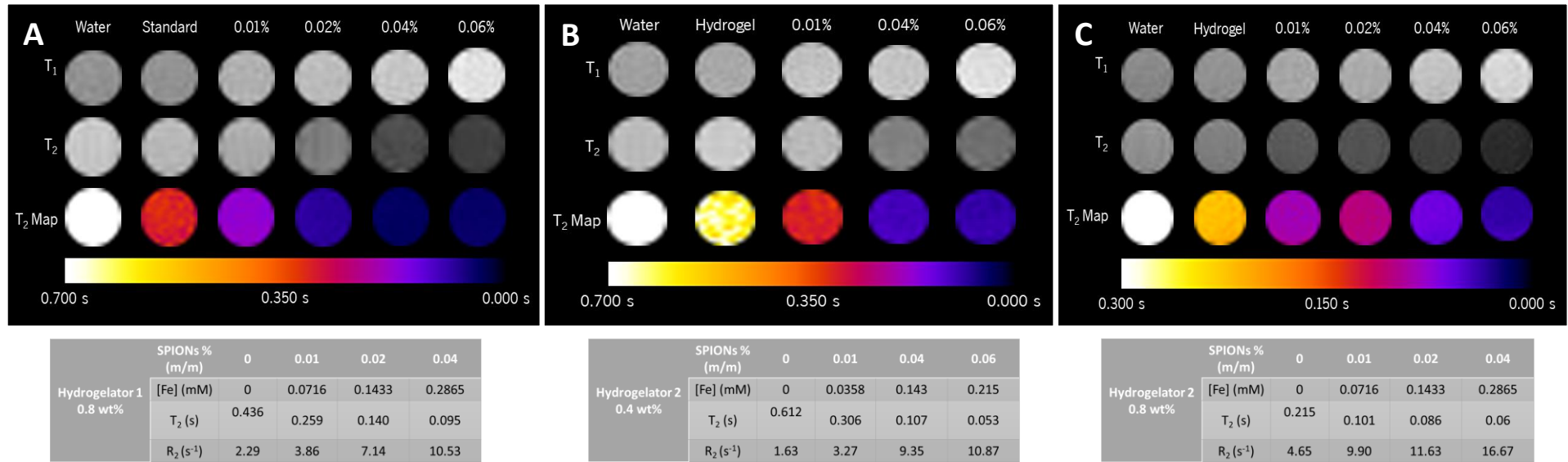
FIGURE 46. T_1- AND T_2 MRI PHANTOM IMAGES AND T_2 RELAXATION MAP OF MAGNETIC HYDROGELS OF: A) DEHYDRODIPEPTIDE **1**, 0.8 %WT ; B) DEHYDRODIPEPTIDE **2**, 0.4 %WT; C) DEHYDRODIPEPTIDE **2**, 0.8 %WT.
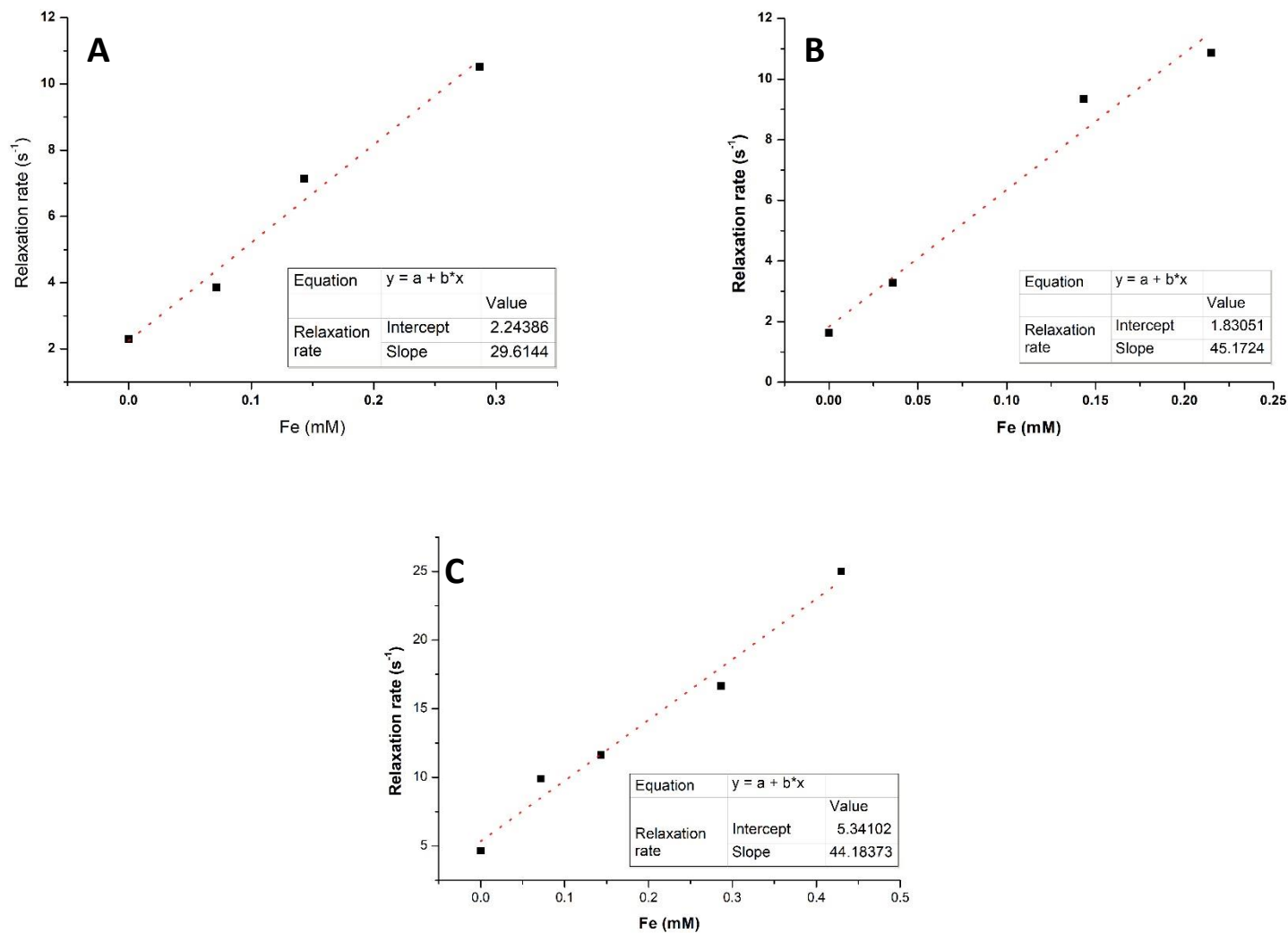
FIGURE 47. DEPENDENCE OF THE OBSERVED PARAMAGNETIC TRANSVERSE RELAXATION RATE (R_2; 3 T, 25 °C) ON THE FE CONCENTRATION OF SPIONS INCORPORATED INTO HYDROGELS OF: A) DEHYDRODIPEPTIDE **1**, 0.8% ; B) DEHYDRODIPEPTIDE **2**, 0.4 WT%; C) DEHYDRODIPEPTIDE **2**, 0.8 WT%.

The incorporation of SPIONs into the hydrogels results in significant reduction of their efficacy as CA for MRI (Table V).

TABLE V. r_2 FOR SPIONs IN WATER AND HYDROGEL **1** AND **2** WITH SPIONs.

	SPIONs	SPIONs incorporated into hydrogel 1	SPIONs incorporated into hydrogel 2	
		0.8 wt%	0.4 wt%	0.8 wt%
r_2(mM^{-1}s^{-1}) 3 T ; 25 ºC	122.1	29.6	45.2	44.2

The outer-sphere relaxation mechanism is determined by the relative translational diffusion of the water molecules and magnetic nanoparticles. Hence, the transverse relaxivity r_2 is compromised by all effects that restrict water diffusion (*e.g.* low temperatures or high medium viscosity). Magnetic nanoparticles enclosed into nanostructures (lipid-based vesicles and liposomes) with restricted access to bulk water display low relaxivities.[55] We have previously confirmed by TEM that hydrogels made by self-assembly of dehydrodipeptides display a nanosized fibrillar structure densely entangled. The incorporated SPIONs are likely randomly distributed into the hydrogel water pools created by fibres entanglement or associated with the fibres through weak non-polar interactions. Restricted water diffusion inside the hydrogel water compartments is very likely the cause of the observed low relaxivities. Interestingly, the concentration of hydrogelator **2** has no significant effect on the relaxivity, although the density of fibres and their entanglement is predicted to increase with hydrogelator concentration. This result suggests that the hydrogelator concentration 0.4 wt% is already limiting of the relaxivity. Moreover, the molecular structure of the hydrogelator seems to have a strong effect on the relaxivity: the tyrosyl dehydrodipeptide hydrogel leads to a more pronounced reduction of SPIONs relaxivity than the aspartyl hydrogel suggesting higher diffusional limitations for the water molecules in the tyrosyl hydrogel.

Although the lower relaxivity of the magnetic hydrogels compared to the SPIONs alone is an obvious limitation for gel imaging by MRI, the significant dark contrast observed at the concentrations tested invites to the exploration of these materials for implantation applications in vivo. Nonetheless, all processes that result in gel disassembly/degradation, with SPION release, are likely to generate a significant relaxivity enhancement. Thus, the magnetic self-assembled

peptide hydrogels are potential self-reporting agents responsive to biological *stimuli* or external triggers such as magnetic hyperthermia.

According to the values of r_2 the magnetic hydrogels preferentially behave as T_2-MRI enhancers. This was further confirmed in the T_2w-MRI iamges, which showed a concentration dependence T_2 signal where a significant darker contrast was observed as we increased the Fe concentration of the hydrogel samples from 0.01 to 0.06%. Interestingly, both magnetic hydrogels 1 (0.4 %wt) and 2 (0.4 wt% and 0.8 %wt) showed an increase of the T_1-MRI signal when compared to a water control as the Fe concentration increased within the same concentration window, being more evident at high Fe concentrations. This dual T_1/T_2-MRI behavior has been already observed in water dispersions of transition metal oxide nanoparticles[56] and provide magnetic hydrogels with original imaging properties for application in the biomedical field, which render them promising biomaterials to be explored as bio-responsive imaging-guide drug delivery systems and self-reporting contrast agents for real-time monitorization of bio-regenerative or -degradative processes. In order to argue about the effect of the structure hydrogelator molecules (aspartic acid or tyrosine residues) and of the micro- and nanostructure of the hydrogel fibres on the T_1- and T_2-MRI properties, a quantitative analysis of the T_1 and T_2 signal intensities as a function of the concentration would be further required by comparing the normalized sample intensity corresponding to the magnetic hydrogels 1 (aspartic acid) and 2 (tyrosine) at 0.8 %wt (Figures 47A and 46C, respectively). Similarly, this would be also needed to study the effect of the hydrogelator concentration on the MRI enhancement provided by the final magnetic hydrogels, thus comparing the Fe-dependant MRI signal intensity corresponding to the magnetic hydrogels 2 at 0.4 and 0.8 %wt (Figure 47B and 47C, respectively). These studies are being carried out in collaboration between the two research groups leading in this work at the UMinho and INL.

Hyperthermia studies

In this work, we envisaged that the self-assembled peptide hydrogel loaded with magnetic nanoparticles could be remotely activated by and external magnetic field triggering the release of drug cargos incorporated in the hydrogel.

The concentration of SPIONs deployed for the MRI studies (0.01-0.06; % m/m) revealed unsuitable for hyperthermia purposes. Initial optimization studies showed that hydrogels **1** and **2** containing 25, 30 and 35 % (m/m) of SPIONs were suitable for hyperthermia studies - a substantial

temperature raise could be attained upon magnetic actuation on the hydrogels. Interestingly, the incorporation of SPIONs revealed detrimental for hydrogel formation (see section on hydrogel rheology). Accordingly, the concentration of hydrogelator **2** had to be increased from 0.4 to 0.8% wt% to ensure the formation of magnetic hydrogels with a suitable SPIONs concentration of 30 and 35 % (m/m).

The capacity of the SPIONs to generate heat upon magnetic excitation with an alternating magnetic field (H= 240 G, f= 869 kHz) was evaluated in solution and the same concentration of particles was then incorporated into the hydrogels (Figure 49).
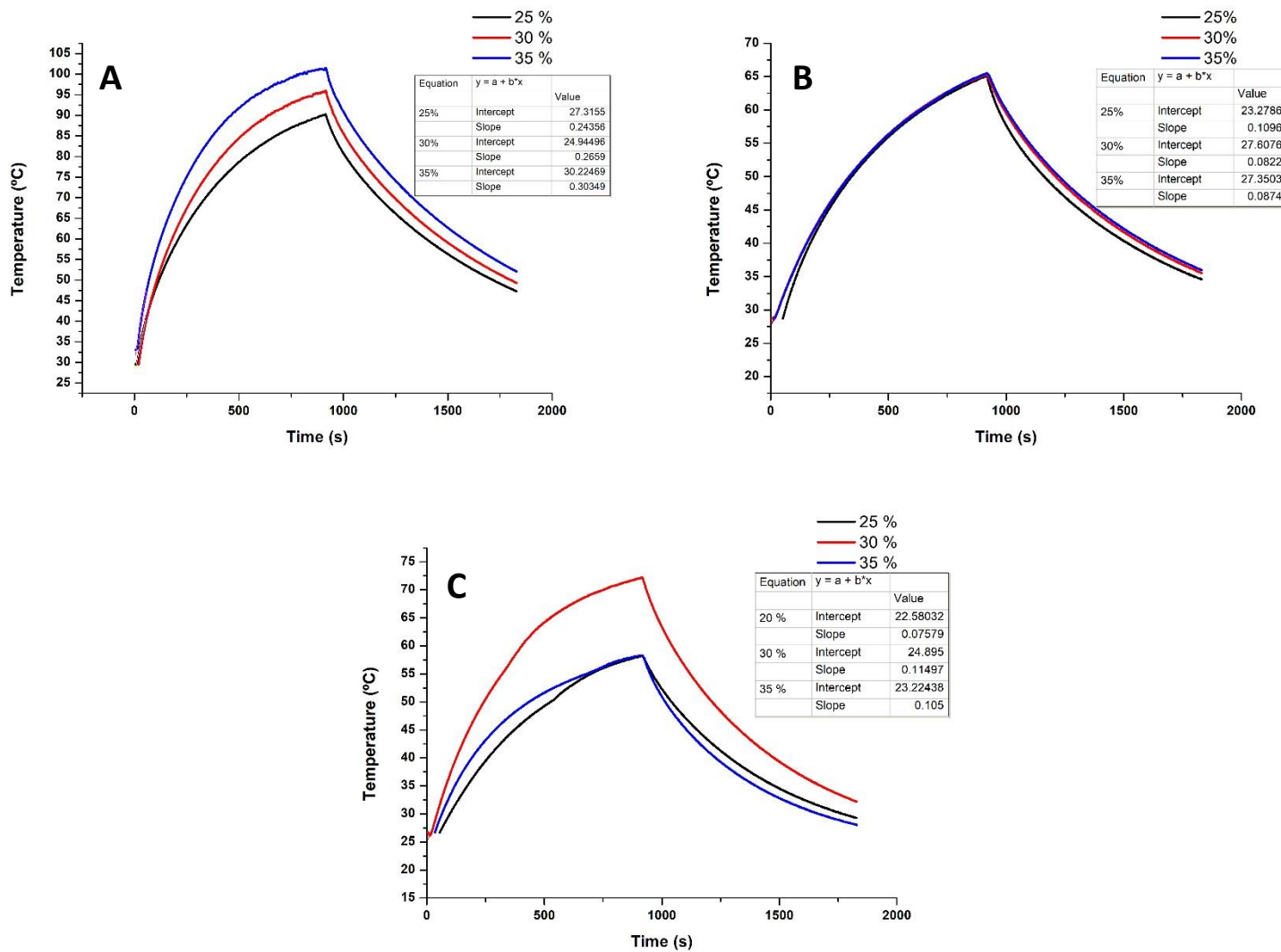
FIGURE 48. HEATING CURVES OF HYDROGELS WITH INCORPORATED SPIONS UNDER AMF IRRADIATION (H=240G, F=869KHZ) : A) SPIONS IN AQUEOUS MEDIUM; B) HYDROGEL **1**, 0.8WT%; C) HYDROGEL **2**, 0.8WT% .

The capacity of the SPIONs to transduce magnetic power into heat in the hydrogel was evaluated by the parameter specific absorption rate (SAR) (Table VI).

TABLE VI. SAR EVALUATION OF SPIONS IN WATER, HYDROGEL **1** AND **2** LOADED WITH SPIONS.

SPIONs		Water			Hydrogel **1** 0.8 wt%			Hydrogel **2** 0.8 wt%		
% m/m	m_{Fe} (g)	dT/dt (°C/s)	ΔT (°C)	SAR (W/g)	dT/dt (°C/s)	ΔT (°C)	SAR (W/g)	dT/dt (°C/s)	ΔT (°C)	SAR (W/g)
25	0.002857	0.24356	62	**356.86**	0.10967	36	**160.69**	0.07579	34	**111.05**
30	0.003429	0.26590	68	**324.60**	0.08227	35	**100.43**	0.11497	45	**140.35**
35	0.005600	0.30349	73	**226.86**	0.08748	35	**65.39**	0.105	34	**78.49**

The specific absorption rate (SAR; W/g) was calculated by the initial slope method (equation 13).[39]

$$SAR = \frac{CVs}{m_{Fe}} \frac{dT}{dt} \quad \text{equation 13}$$

C is the volumetric specific heat capacity of the magnetic nanoparticle solution (J/(cm³.°C)); Vs is the volume of sample (cm³); m_{Fe} (g) is the mass of iron in the experiment and dT/dt is the initial rate of temperature rise obtained from the T vs t curve (Figure 48).

For the calculation of the SAR it was assumed that the presence of the SPIONs do not change significantly the volumetric specific heat capacity of pure water (4,186 J/(cm³.°C)). While this assumption seems fully justified for the solution of SPIONs in water, for the hydrogels containing SPIONs it is more questionable. Although the hydrogels (0.8 wt%) are 99 % water, putative phase transitions and structural rearrangements of the hydrogel during the heating phase are prone to involve heat exchange processes. As a first approximation we assumed that the hydrogel matrix does not affect significantly the heat capacity of pure water. This aspect requires further investigation.

The SPIONs water dispersions display SAR values as high as 300 W/g (H= 240G, f= 869 kHz), within the range expected for Fe_3O_4 nanoparticles with a core size around 8 nm. The heating properties of SPIONs induced under an oscillating magnetic field are due to two main magnetic relaxation mechanisms. On the one hand, to the Néel relaxation, which is related to the rotation of the magnetic moment to align with the direction of the applied magnetic field. Therefore, the Néel

contribution to the SAR of a MNPs dispersion is mainly determined by the saturation magnetization Ms, particle size and anisotropy (constant) of the nanoparticles. The saturation magnetization of Fe_3O_4 nanoparticles is determined by their ferrite spinel structure and can be obtained from the hysteresis loops. On the other hand, to the Brownian relaxation, which is due to the friction between the nanoparticles and the solvent due to the vibration of the nanoparticles as consequence of the torque in turn provoked by the alignment of the magnetic moment of the nanoparticles and the direction of the applied magnetic field.

Incorporation of SPIONs into hydrogels **1** and **2** leads to a very substantial reduction (over 50%) of their efficacy (SAR) as heat generators. This suggests that the SPIONs interact with the hydrogel fibril network, which results in a reduction of the contribution of the Brownian relaxation mechanism to the overall relaxation. Thus, Néel relaxation, less effective than Brown relaxation in small magnetite nanoparticles, becomes the dominating heat generating mechanism when the SPIONs are incorporated into the hydrogel. It is noteworthy that the reduction in SAR is more pronounced for hydrogel **2** than **1,** suggesting that hydrogel **2** displays a higher density of fibres enhancing *trapping* of SPIONs. Interestingly, while the SPIONs incorporated into hydrogel **1** showed a monotonic reduction of SAR with increasing concentration of nanoparticles, the SAR values measured for the SPIONs incorporated into hydrogel **2**, reach a maximum at Fe concentration 30 % (m/m). This observation is compatible with a switch of the relaxation mechanism from a dominating Brownian mechanism to a dominating Néel relaxation mechanism. This aspect requires further studies. Moreover, the water dispersions of SPIONs usually display concentration-dependent SAR values (H = 240 G; f = 869 kHz). In the range of SPIONs concentration studied in this work (25-35%, m/m), the efficacy of the SPIONs as heat generators decreases with increasing nanoparticle concentration. This confirms the existence of some sort of interaction between the nanoparticles and the hydrogel fibrils in the resulting magnetic hydrogels within this this range of SPIONs concentrations range (25-35%, m/m).

Magnetic hyperthermia studies indicate that incorporation of SPIONs into self-assembled peptide-based hydrogels leads to substantial reduction of their efficacy as heat generators. Nonetheless, under the conditions studied in this work, 8 % (m/v) of hydrogelator and 25-35% (m/m) of SPIONs, magnetic excitation (H = 240 G; f = 869 kHz) is still efficient in inducing gel-sol phase transition. Hence, the hydrogels loaded with SPIONs can be effective drug carriers for magnetically-triggered drug delivery.

FIGURE 49. HYDROGEL AFTER THE HYPERTHERMIA ANALYSIS. A- MAGNETIC HYDROGEL **1** WITH INCORPORATED 25 %, 30% AND 35% OF SPIONS; B- MAGNETIC HYDROGEL **2** WITH INCORPORATED 30% SPIONS.

Chapter 3

Conclusions

In this project we aimed at demonstrating that dehydrodipeptide-based self-assembled hydrogels could be rendered magneto-responsive by incorporation of superparamagnetic iron oxide nanoparticles (SPIONs). Magnetic hyperthermia (MH) could conceptually be used as a remote trigger for release of incorporated drug cargos. Novel dehydrodipeptide hydrogelators were synthesised and fully characterised by ^{1}H and ^{13}C NMR spectroscopy. Methodologies were developed for gelation and incorporation of SPIONs into the self-assembled hydrogels. TEM experiments showed that the self-assembled hydrogels display fibrilar structure. Rheological characterization showed that incorporation of SPIONs not only delays the structural build of hydrogels up also weakens hydrogel strength (elasticity). The performance of SPIONs incorporated into the hydrogels, as paramagnetic water relaxers (contrast agents for MRI) and as heat generators (MH), is significantly lower than in pure water.

The magnetic characterization revealed predominant paramagnetic properties at high (10 % m/m) concentration of incorporated SPIONs, although mixed with a diamagnetic contribution from the organic hydrogelator matrix. Moreover, there is evidence of strong magnetic dipolar interactions between the magnetite nanoparticles in the gel network.

The weakening of gel elasticity and the reduced efficacy of the hydrogel-incorporated SPIONs as contrast agents for MRI and as heat generators for MH, suggests an interaction between the hydrogelator fibres and the nanoparticles. Nanoclustering of the SPIONs in the aqueous water pools on the hydrogel matrix is also a hypothesis that deserves further investigation.

The reduction in performance observed for the SPIONs incorporated into the hydrogel may be turned into advantage as hyperthermia-mediated nanoparticle (and drug) release could become a self-reporting strategy.

Chapter 4

Experimental procedures

Reagents and instrumentation

Analytical grade reagents were purchased from Sigma-Aldrich and Acros and used without further purification. Analytical grade solvents were used and dried by the usual methods when was needed. The petroleum ether used refers to the fraction having a boiling point of 40-60°C. Distilled water was always used for the reactions when aqueous medium was needed. The reactions were monitored by thin layer chromatography (TLC) on Merck-Kieselgel plates 60 F254 and detection was made by examination under UV light (240 nm) or by adsorption of iodine vapour. The organic phases were dried using anhydrous magnesium sulphate (Riedel) and carbonate of anhydrous potassium (Merck). Chromatographic separations were performed on silica MN Kieselgel 60 M (230-400 mesh). When solvent gradient was used, the increase of polarity was made from neat petroleum ether to mixtures of diethyl ether/petroleum ether, increasing 10% of diethyl ether each time until the isolation of the product.

The ^{1}H and ^{13}C NMR spectra (assigned by DEPT, HSQC and HMBC techniques) were recorded on a Bruker Avance III 400 spectrometer, operating at 400.13 MHz and 100.62 MHz, for ^{1}H and ^{13}C NMR respectively. The NMR spectra were recorded at 25°C and in some cases at 75°C, using the residual solvent signals as reference. Deuterated dimethyl sulfoxide (DMSO-d_6) and deuterated chloroform (CDCl$_3$-d_1) were used as solvents. Chemical shifts are given in parts per million (ppm) and the coupling constants in Hertz (Hz). HRMS data were recorded by the mass spectrometry service of the University of Vigo, Spain. MS was recorded by a Thermo Finnigan LxQ (Linear Ion Trap) Mass Detector with Electro Spray Ionization (ESI).

The IR spectra were performed on a Jasco FT / IR 4100 apparatus with Fourier transform and a resolution of 4 cm^{-1} in the region between 4000 and 600 cm^{-1}. The spectrum was obtained by 64 scans.

CD spectra were recorded under N$_2$ on a Jasco J815 CD spectrometer. The samples used were solutions from dilutions of the preparation of the hydrogels.

MR imaging was performed in a 3.0 T horizontal bore MR Solutions Benchtop MRI system equipped with 48 G/cm actively shielded gradients. To image the samples, a 56 mm diameter quadrature birdcage coil was used in transmit/receive mode. For the phantom measurements, the samples at different concentrations (between 0-0.43 mM Fe) were dissolved in 200 μL of Milli-Q water in 300 μL tubes. All MR images of the phantoms were acquired with an image matrix 256 252, field of view (FOV) 60 60 mm, 3 slices with a slice thickness of 1 mm and 1 mm slice gap.

For T2-weighted imaging, fast spin echo (FSE) sequences with the following parameters were used: TE = 15 ms, TR = 1500 ms, NA = 12, AT = 24m 48s. For T1-weighted imaging a FSE sequence with TE = 11 ms, TR = 400 ms, NA = 12 and AT= 7m 34s was used.

Transmission electron microscopy images (TEM) were obtained on a JEOL JEM-2100 microscope at an accelerating voltage of 200 kV. The samples were prepared using a uranyLess staining. Using a carbon coated grid, 10µL of the hydrogel was placed and left for 30 seconds. The excess of water was removed using filter paper. The grid was washed with 10µL of uranyLess and water (2 times), always removing the excess with filter paper after 30 seconds.

Properties as magnetic hyperthermia effectors were investigated using a nB nanoScale Biomagnetics DM-100instrument. Zero-field-cooled (ZFC) and field-cooled (FC) magnetization curves were recorded in a superconducting quantum interference device magnetometer (SQUID-VSM, Quantum Design) over the temperature range of 5–300 K and under an applied magnetic field of 100 Oe.

The hydrogels kinetics and mechanical spectra were measured with a stress-controlled rotational rheometer (MCR300, Anton Paar). Liquid samples were loaded into the Couette geometry of the rheometer and temperature was kept at 25 °C during testing. For the hydrogels kinetics, small amplitude oscillatory shear was applied during 60 000 seconds, with a frequency of 1 Hz and an amplitude varying from 0.0001% to 1 %, depending on the NP loading in sample. After the kinetics, mechanical spectra were recorded using the same strain amplitude as in the kinetics tests, by ramping the frequency from 100 Hz down to 0.01 Hz.

For the formation of the hydrogel the dehydropeptide was weighted into a sample vial and water was added. While on stirring, NaOH (1M) was added till pH 10. The mixture was sonicated and then added GDL and stirred for 5 seconds. The solutions were left standing overnight to form the hydrogel. When the hydrogel was loaded with nanoparticles, its addition occurred before the stabilization of pH 10.

Synthesis

Synthesis of Fmoc-L-Tyr(O^{t}Bu)-Phe(β-OH)-OMe, 5
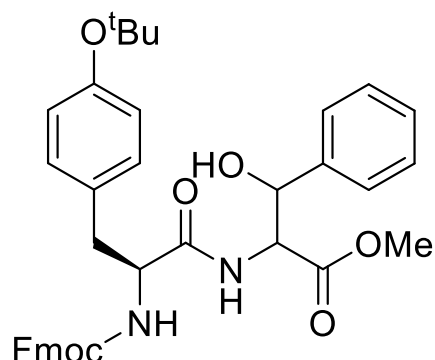
Fmoc-Tyr(O^{t}Bu)-OH, **3** (2.5 mmol, 1.13 g) was dissolved in acetonitrile (20 mL) in an ice bath. HOBt (1.2 eq., 2.8 mmol, 0.43 g), DCC (1.2 eq., 2.8 mmol, 0.57 g), H-Phe(β-OH)-OMe, **4** (1.0 eq., 2.5 mmol, 0.58 g) and triethylamine (2.2 eq., 5.7 mmol, 0.8 mL) were added, waiting about 2 minutes between each addition. The mixture was left stirring overnight. The urea was filtered, and the solvent was removed under reduced pressure. Acetone was added, and the mixture was stored in the freezer for 3 h. The urea was filtered again. Evaporation at reduced pressure gave a residue that was partitioned between ethyl acetate (50 mL) and KHSO$_4$ (30 mL, 1 M). The organic phase was thoroughly washed with KHSO$_4$ (1 M), NaHCO$_3$ (1 M), and brine (3 × 30 mL, each) and dried with MgSO$_4$. Removal of the solvent afforded compound **5** as a diastereomeric mixture (1.41 g, 89%).

^{1}H NMR (400 MHz, CDCl$_3$,δ):1.31 and 1.32 (9H, 2s, C(CH$_3$), 1.6-1.7 (1H, m, CH-Fmoc), 2.85-2.96 (2H, m,β-CH$_2$ Tyr), 3.71 (3H, s, OMe CO$_2$CH$_3$), 4.11-4.20 [5H, m, CH Fmoc + CH$_2$ Fmoc + α-CH Tyr + α-CH Phe(β-OH)], 4.7-4.8 (2H, m, CH$_2$-Fmoc), 5.22-5.24 [1H, m,β-CH Phe(β-OH)], 6.85-7.77 [19 H, m, ArH + NH-Tyr + NH Phe(β-OH)].

Synthesis of Npx-L-Tyr(OᵗBu)-Phe(β-OH)-OMe, 6
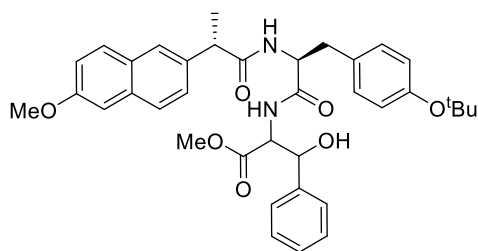
Fmoc-Tyr(OᵗBu)-Phe(β-OH)-OMe, **5** (1 mmol, 0.64 g) was dissolved in DMF (2 mL) and piperidine (0.5 mL) was added. The mixture was left stirring for 10 minutes until a white precipitate started to form. Ethyl acetate (50 mL) was added and reaction mixture was washed with distilled water (3 x 50mL). The organic phase was then dried and the removal of the solvent afforded the *N*-deprotected dipeptide as an oil (1.27 g). This compound was used without purification. The oil was dissolved in dry DCM (7 mL) and put in ice bath. (S)-(+)-naproxen chloride (1 mmol , 0.25g) and NEt₃ (2.1 eq., 2.1 mmol, 0.3 mL) were added and the reaction mixture was left stirring overnight (18 h). Removal of the solvent at reduced pressure gave a residue that was partitioned between ethyl acetate (50 mL) and KHSO₄ (30 mL, 1 M). The organic phase was thoroughly washed with KHSO₄ (1 M), NaHCO₃ (1 M), and brine (3 × 30 mL, each) and dried with MgSO₄. Removal of the solvent afforded compound **6** as diastereomeric mixture (0.56 g, 89%).

¹H NMR (400 MHz, DMSO,δ):1.30 and 1.31 (9H, 2s, C(CH₃), 1.60 and 1.57 (3H, 2d, *J* = 7.2 Hz, CH₃ Npx), 2.71-2.88 (2H, m, β-CH Tyr), 3.61 and 3.68 (3H, 2s, OMe CO₂Me), 3.82-3.93 (4H, m, CH Npx + OCH₃ Npx), 4.55-4.61 [2H, m, α-CH Phe(β-OH)] + α-CH Tyr), 5.10-5.17 [1H, m, Phe(β-OH)], 6.82 (2H,d, *J* = 8.4, ArH Tyr), 7.01 (2H,d ,*J* = 8.4 Hz, ArH Tyr) 7.12-7.76 [13 H, m, ArH + NH Tyr + Phe(β-OH)]

Synthesis of Npx-L-Tyr(OᵗBu)-*Z*-ΔPhe-OMe, 7
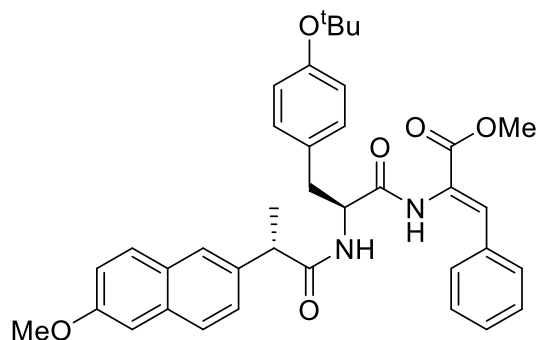
DMAP (0.1 equiv, 0.09 mmol, 0.012 g) was added to a solution of compound **6** (0.9

mmol, 0.56 g) in dry acetonitrile (10 mL) followed by Boc₂O (1.1 equiv) under rapid stirring at rt. The reaction was monitored by ¹H NMR until all the reactant had been consumed (18–24 h). Then *N,N,N',N'*-tetramethylguanidine (2% in volume) was added, stirring was continued, and the reaction followed by ¹H NMR. When all the reactant had been consumed, removal of the solvent at reduced pressure gave a residue that was partitioned between ethyl acetate (50 mL) and KHSO₄ (30 mL, 1 M). The organic phase was thoroughly washed with KHSO₄ (1 M), NaHCO₃ (1 M), and brine (3 × 30 mL, each) and dried with MgSO₄. Removal of the solvent afforded an yellow oil (0.39 g, 71 %). Column chromatography (petroleum ether/ethyl ether) gave compound **7** as a beige solid (0.21g, 39 %)

¹H NMR (400 MHz, CDCl₃,δ):1.31 (9H, s, C(CH₃), 1.53 (3H, d, J = 7.2 Hz, CH₃ Npx), 2.92-3.08 (2H, m, β-CH Tyr), 3.62 (1H, q, J =7.2 Hz, CH Npx), 3.73 (3H, s, OMe CO₂Me), 3.93 (3H, s, OMe Npx), 4.69-4.74 (1H, m, α-CH Tyr), 5.81 (1H, d, J =7.6 Hz, NH Tyr), 6.76 (2H, d, J = 8.4 Hz, ArH Tyr), 6.92 (2H, d, J = 8.4 Hz, ArH Tyr), 7.10 (1H, s, β-CH ΔPhe), 7.11-7.67 (12H, m, ArH + NH ΔPhe).

¹³C NMR(100 MHz, CDCl₃ ,δ): 18.12 (CH₃ Npx),28.81 (C(*C*H₃)₃), 36,08 (CH₂ β-CH Tyr), 46.88 (CH Npx), 52.50 (CH₃, OMe CO₂Me), 54.53 (α-CH Tyr), 55.29 (CH₃ OMe Npx), 78.34 (*C*(CH₃)), 105.60 (CH Ar), 119.21 (CH Ar), 123.68 (C ΔPhe), 124.22 (CH Ar), 125.97 (CH Ar), 126.14 (CH Ar), 127.70 (CH Ar), 128.53 (CH Ar), 128.93 (C Ar),129.26 (CH Ar), 129.42 (CH Ar), 129.65 (CH Ar), 130.83 (C Ar),132.51 (C Ar),133.84 (C Ar), 133.81 (C Ar),135.23 (C Ar), 154.30 (C Ar Tyr), 157.79 (C Ar Npx), 165.13 (C=O ΔPhe),169.61 (C=O Tyr) 175.01 (C=O Npx)

Synthesis of Npx-L-Tyr-*Z*ΔPhe-OMe, 8
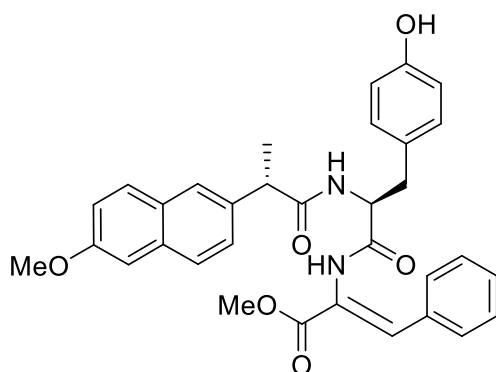
To Npx-Tyr(O*t*Bu)-ΔPhe-OMe (0.3 mmol, 0.19 g) was added TFA (3 mL) and was left at room temperature for 4 h. The solvent was removed under reduced pressure and ethyl ether was

added to the residue which was left in the freezer. The mixture was filtrated, and compound **8** was isolated as a beige solid (0.14 g, 87%).

¹H NMR (400 MHz, DMSO,δ):1.26 (3H, d, *J* = 7.2 Hz, CH₃ Npx), 2.69-2.99 (2H,m , β-CH₂ Tyr) , 3.60 (3H, s, OMe CO₂Me), 3.81-3.83 (4H, m, OMe Npx + CH Npx), 4.63-4.69 (1H, m, α-CH Tyr), 6.66 (2H, d, *J* = 8.4 Hz, ArH Tyr), 7.07-7.69 (14H, m, ArH Tyr + Npx + β-CH ΔPhe), 8.21 (1H, d, *J*=8.4 Hz, NH Tyr), 9.18 (1H, bs, OH Tyr), 9.79 (1H, s, NH ΔPhe).

Synthesis of Npx-L-Tyr-*Z*ΔPhe-OH, 1
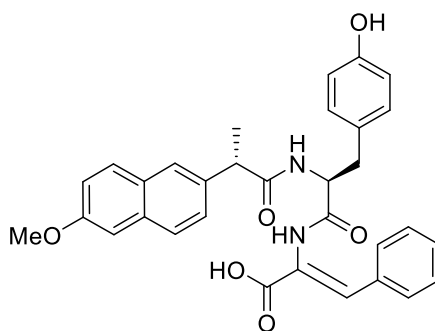
Npx-Tyr-ΔPhe-OMe (0.26 mmol of 0.14 g) was dissolved in 1,4-dioxane (2mL) and NaOH (1M) (3 mL).The reaction was monitored by TLC. The organic solvent was removed under reduced pressure and the reaction mixture was acidified to pH 3 with KHSO₄ (1M) the solid formed was filtered affording compound **1** (0.14 g, quantitative yield).

¹H NMR (400 MHz, DMSO-d₆,δ):1.24 (3H, d, *J* = 6.8 Hz, CH₃ Npx), 2.67-3.02 (2H, m, β-CH₂ Tyr), 3.75 (1H, q, *J* = 6.8 Hz, CH Npx),3.79 (3H, s, OMe Npx), 4.62-4-87 (1H, m, ,α-CH Tyr), 6.64 (2H, d, *J* = 8.4 Hz, ArH Tyr), 7.07-8.23 (14H, m, ArH Npx + Tyr + ΔPhe), 8.21 (1H, d, *J* = 8.4 Hz, NH Tyr), 9.17 (1H, bs, OH Tyr), 9.6 (1H, bs, NH ΔPhe).

¹³C NMR(100 MHz, DMSO-d₆,δ): 18.91 (CH₃ Npx), 36.59 (β-CH₂ Tyr), 44.66 (CH Npx), 54.19 (α-CH Tyr), 55.12 (OCH₃ Npx), 105.63 (CH), 114.80 (CH Ar), 118.39 (CH Ar), 125.35 (CH Ar), 126.40 (CH Ar), 126.52 (C Ar),126.69 (CH Ar), 127.93 (C Ar), 128.32 (C Ar), 128.34(CH Ar), 128.95 (CH Ar), 129.07 (CH Ar), 129.80 (CH Ar), 130.24 (CH Ar), 131.43 (CH Ar), 133.05 (C Ar), 133.60 (C Ar), 137.14 (C Ar), 155.75 (C Ar), 156.90 (C Ar), 166.19 (C=O ΔPhe), 171.00 (C=O Tyr), 173.32 (C=O Npx)

MS (ESI) m/z: [M+H]⁺ calcd for C₂₈H₂₈N₂NaO₇ 538.21; found 537.26.

Synthesis of Fmoc-L-Asp(OᵗBu)-Phe(β-OH)-OMe, 11
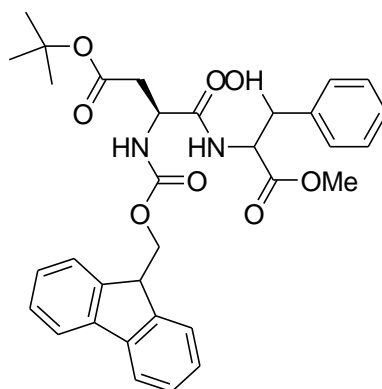
Fmoc-Asp(OᵗBu)-OH, **10** (2.2 mmol, 0.90 g) was dissolved in acetonitrile (20 mL) in an ice bath. HOBt (1 eq., 2.2 mmol, 0.34 g), DCC (1.1 eq., 2.4 mmol, 0.50 g), H-Phe(β-OH)-OMe, **4** (1.0 eq., 2.2 mmol, 0.51 g) and triethylamine (2.0 eq., 4.4 mmol, 0.62 mL) were added, waiting about 2 minutes between each addition. The mixture was left stirring overnight. The urea was filtered, and the solvent was removed under reduced pressure. Acetone was added, and the mixture was stored in the freezer for 3 h. The urea was filtered again. Evaporation at reduced pressure gave a residue that was partitioned between ethyl acetate (50 mL) and KHSO₄ (30 mL, 1 M). The organic phase was thoroughly washed with KHSO₄ (1 M), NaHCO₃ (1 M), and brine (3 × 30 mL, each) and dried with MgSO₄. Removal of the solvent afforded compound **11** as a diastereomeric mixture (1.27 g, 98%).

¹H NMR (400 MHz, CDCl₃,δ):1.44 and 1.47 (9H, 2s, C(CH₃), 2.41 - 2.86 (2H, m, β-CH₂ Asp) , 3.71 and 3.74 [3H, 2s, OMe CO₂Me), 4.12-4.61 (4H, m, α-CH Asp + CH + CH₂ Fmoc) 4.79-4.87 [(1H, m, α-CH Phe(β-OH)], 5.26-5.31 [1H, m, β-CH Phe(β-OH)], 5.80 and 5,92 (1H, 2d, *J* = 7.6 and 8.4 Hz, NH Asp), 7.29-7.88 [(14 H, m, ArH + NH Phe(β-OH)).


Synthesis of Npx-L-Asp(OᵗBu)-Phe(β-OH)-OMe, 12
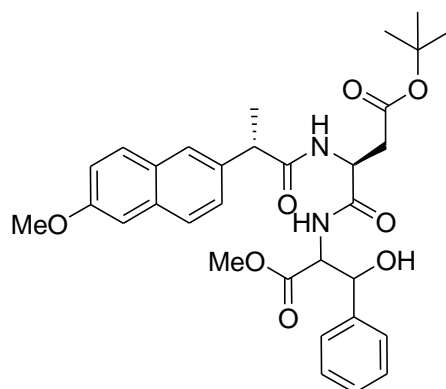
Fmoc- Asp(OᵗBu)-Phe(β-OH)-OMe, **11** (1.2 mmol, 0.49 g) was dissolved in DMF (2 mL)

and piperidine (0.5 mL) was added. The mixture was left stirring for 10 minutes until a white precipitate started to form. Ethyl acetate (50 mL) was added and reaction mixture was washed with water (3 x 50mL). The organic phase was dried and removal of the solvent afforded a mixture of the *N*-deprotected dipeptide with dibenzofulvene as an oil (0.32g). The oil was dissolved in dry DCM (6 mL) in ice bath. (S)-(+)-naproxen chloride (0.86 mmol , 0.21g) and NEt$_3$ (2 eq., 1.72 mmol, 0.25 mL) were added and the reaction mixture was left stirring overnight (18 h). Removal of the solvent at reduced pressure gave a residue that was partitioned between ethyl acetate (50 mL) and KHSO$_4$ (30 mL, 1 M). The organic phase was thoroughly washed with KHSO$_4$ (1 M), NaHCO$_3$ (1 M), and brine (3 × 30 mL, each) and dried with MgSO$_4$. Removal of the solvent afforded compound **12** as diastereomeric mixture (0.39 g, 79%).

^{1}H NMR (400 MHz, DMSO ,δ):1.35 and 1.36 (9H, 2s, C(CH$_3$), 1.58 and 1.61 (3H, 2d, *J* = 7 Hz, CH$_3$ Npx), 2.31-2.81 (2H, m, β-CH$_2$ Asp), 3.57 and 3.65 (3H, 2s, OMe CO$_2$CH$_3$), 3.68-3.74 (4H, m, CH Npx) 3.91 and 3.92 (3H, 2s, OCH$_3$ Npx), 4.63-4.66 [2H, m, α-CH Phe(β-OH) and α-CH Asp), 5.13-524 [1H, m, β-CH$_2$ Phe(β-OH)], 7.11-7.76 [14 H, m, ArH + NH Asp + NH Phe(β-OH)]

Synthesis of Npx-L-Asp(O^{t}Bu)-*Z*-ΔPhe-OMe, 13
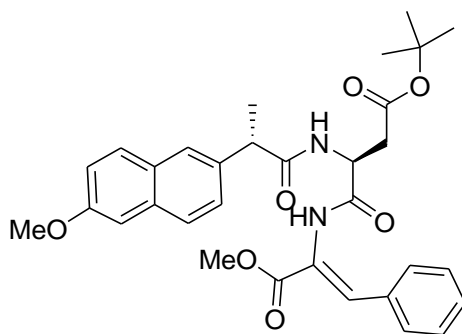
DMAP (0.1 equiv, 0.07 mmol, 0.009 g)) was added to a solution of compound **12** (0.7 mmol, 0.39 g) in dry acetonitrile (5 mL) followed by Boc$_2$O (1.0 equiv) under rapid stirring at rt. The reaction was monitored by ^{1}H NMR until all the reactant had been consumed (18–24 h). Then *N,N,N′,N′*-tetramethylguanidine (2% in volume) was added, stirring was continued, and the reaction followed by ^{1}H NMR. Removal of the solvent at reduced pressure gave a residue that was partitioned between ethyl acetate (50 mL) and KHSO$_4$ (30 mL, 1 M). The organic phase was thoroughly washed with KHSO$_4$ (1 M), NaHCO$_3$ (1 M), and brine (3 × 30 mL, each) and dried with MgSO$_4$. Removal of the solvent afforded an yellow oil (0.22 g, 56 %). Column chromatography (petroleum ether/ethyl ether) gave compound **13** as a white solid (0.12g, 31 %)

^{1}H NMR (400 MHz, CDCl$_3$,δ):1.36 (9H, s, C(CH$_3$), 1.61 (3H, d, *J* = 7.2 Hz, CH$_3$ Npx), 2.55

(1H, dd, J = 6.8 Hz e 16.8 Hz, β-CH₂ Asp), 2.89 (1H, dd, J = 4.0 Hz e 16.8 Hz, β-CH₂ Asp), 3.73 (3H, s, OMe CO₂Me) 3.76 (1H, q, J = 7.2 Hz, CH Npx), 3.92 (3H, s, OMe Npx), 4.88-4.93 (1H, m, α-CH Asp), 6.82 (1H, d, J = 8.0 Hz, NH Asp), 7.04 (1H, s, β-CH ΔPhe), 7.11-7.13 (1H, m, ArH), 7.24-7.26 (3H, m, ArH), 7.32-7.37 (4H, m, ArH), 7.61-7.68 (3H, m, ArH), 7.84 (1H, bs, NH ΔPhe).

¹³C NMR (100 MHz, CDCl₃,δ): 18.25 (CH₃-Npx), 27.90 [(*C*H₃)₃C], 36.29 (CH₂ β-CH₂ Asp), 47.00 (CH Npx), 49.62 (CH α-CH Asp), 52.47 (CH₃ CO₂Me), 55.29 (CH₃ OMe Npx), 81.94 [*C*(CH₃)], 119.14 (CH Ar), 123.52 (C ΔPhe), 125.71 (CH Ar), 125.98 (CH Ar), 127.74 (CH Ar), 127.79 (CH Ar), 128.43 (CH Ar), 128.59 (C Ar), 129.01 (C Ar), 129.22 (CH Ar), 129.44 (CH Ar), 129.72 (CH Ar),133.21 (CH Ar),133.26 (C Ar), 133.80 (C Ar),135.69 (C Ar), 157.72 (C Ar Npx), 169.27 (C=O ΔPhe),171.22 (C=O Asp) 174.58 (C=O Npx)

HRMS (ESI) m/z: [M+H]⁺ calcd for C₃₂H₃₇N₂O₇ 561.25884; found 561.25953.

Synthesis of Npx-L--Asp-*Z*ΔPhe-OMe, 2
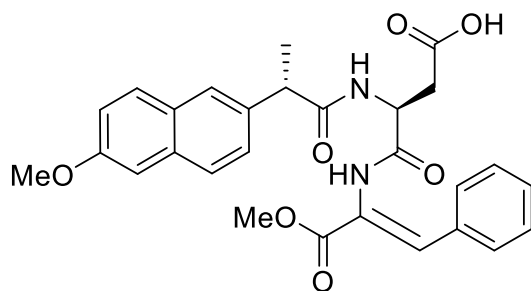
TFA (1.5 mL) was added to Npx-Asp(OᵗBu)-ΔPhe-OMe, **13** (0.35 mmol, 200 mg) and the mixture was left at room temperature for 4 h. The solvent was removed under reduced pressure and ethyl ether was added to the residue which was left in the freezer. Compound **2** was obtained as beige solid (144 mg, 82%).

¹H NMR (400 MHz, DMSO,δ):1.41 (3H, d, J = 7.2 Hz, CH₃ Npx), 2.59-2.77 (2H, m, β-CH₂ Asp) , 3.59 (3H, s, OMe CO₂Me), 3.81 (1H, q, J = 7.2 Hz, CH Npx), 3.83 (3H, s, OMe Npx), 4.73-4.79 (1H, m, ,α-CH Asp), 7.1 (1H, dd, J = 2.8 Hz e J =9.2 Hz ArH), 7.19 (1H, s, β-CH ΔPhe), 7.21-7.23 (4H, m, ArH,), 7.44 (1H, dd, J = 1.6 Hz e 8.8 Hz, ArH Npx), 7.57-7.60 (2H, m, ArH) 7.67-7.71 (3H, m, ArH), 8.39 (1H, d, J = 7.6 Hz, NH Asp), 9.59 (1H, s, NH ΔPhe), 12.37 (1H, bs, COOH).

¹³C NMR(100 MHz, DMSO ,δ): 18.95 (CH₃-Npx), 35.88 (CH₂ β-Asp), 44.70 (CH Npx), 49.55 (α-CH Asp), 52.10 (OCH₃ CO₂Me), 55.14 (OCH₃ Npx), 105.66 (CH Ar), 118.44 (CH Ar), 125.46 (CH Ar), 125.62 (CH Ar), 126.49 (CH Ar), 126.68 (CH Ar), 128.37 (C Ar), 128.46(CH

Ar), 129.08 (CH Ar), 129.36 (CH Ar), 130.11 (CH Ar), 132.10 (β-CH ΔPhe), 133.11 (C ΔPhe), 137.08 (C Ar), 156.95 (C Ar), 165.25 (C=O ΔPhe), 170.57 (C=O Asp), 171.51 (CO$_2$H) 173.63 (C=O Npx).

HRMS (ESI) m/z: [M+Na]$^+$ calcd for C$_{28}$H$_{28}$N$_2$NaO$_7$ 527.17887; found 527.17862.

Chapter 5

References

[1]   S. M. Douglas, H. Dietz, T. Liedl, B. Högberg, F. Graf, and W. M. Shih, "Self-assembly of DNA into nanoscale three-dimensional shapes," *Nature*, vol. 459, no. 7245, pp. 414–418, **2009**.

[2]   G. Fichman and E. Gazit, "Self-assembly of short peptides to form hydrogels: Design of building blocks, physical properties and technological applications," *Acta Biomater.*, vol. 10, no. 4, pp. 1671–1682, **2014**.

[3]   H. Vilaça *et al.*, "Dehydrodipeptide Hydrogelators Containing Naproxen N-Capped Tryptophan: Self-Assembly, Hydrogel Characterization, and Evaluation as Potential Drug Nanocarriers," *Biomacromolecules*, vol. 16, no. 11, pp. 3562–3573, **2015**.

[4]   N. M. Sangeetha and U. Maitra, "Supramolecular gels: Functions and uses," *Chem. Soc. Rev.*, vol. 34, no. 10, pp. 821–836, **2005**.

[5]   H. Vilaça *et al.*, "New self-assembled supramolecular hydrogels based on dehydropeptides," *J. Mater. Chem. B*, vol. 3, no. 30, pp. 6355–6367, **2015**.

[6]   J. Raeburn, A. Z. Cardoso, and D. J. Adams, "The importance of the self-assembly process to control mechanical properties of low molecular weight hydrogels," *Chem. Soc. Rev.*, vol. 42, no. 12, pp. 5143–5156, **2013**.

[7]   E. R. Draper and D. J. Adams, "Low-Molecular-Weight Gels : The State of the Art," *CHEMPR*, vol. 3, no. 3, pp. 390–410, **2017**.

[8]   E. K. Johnson, D. J. Adams, and P. J. Cameron, "Peptide based low molecular weight gelators," *J. Mater. Chem.*, vol. 21, no. 7, pp. 2024–2027, **2011**.

[9]   N. Habibi, N. Kamaly, A. Memic, and H. Shafiee, "Self-assembled peptide-based nanostructures: Smart nanomaterials toward targeted drug delivery," *Nano Today*, vol. 11, no. 1, pp. 41–60, **2016**.

[10]   Z. Yang, G. Liang, M. Ma, Y. Gao, and B. Xu, "Conjugates of naphthalene and dipeptides produce molecular hydrogelators with high efficiency of hydrogelation and superhelical nanofibers," *J. Mater. Chem.*, vol. 17, no. 9, pp. 850–854, **2007**.

[11]   P. K. Singh, S. Chibh, T. Dube, V. S. Chauhan, and J. J. Panda, "Arginine-α, β-dehydrophenylalanine Dipeptide Nanoparticles for pH-Responsive Drug Delivery," *Pharm. Res.*, vol. 35, no. 2, p. 35, **2018**.

[12]   J. Nanda, B. Adhikari, S. Basak, and A. Banerjee, "Formation of hybrid hydrogels consisting of tripeptide and different silver nanoparticle-capped ligands: Modulation of the mechanical strength of gel phase materials," *J. Phys. Chem. B*, vol. 116, no. 40, pp. 12235–12244, **2012**.

[13]   J. Gao, H. Gu, and B. Xu, "Multifunctional Magnetic Nanoparticles : Design , Synthesis , and Biomedical Applications," vol. 42, no. 8, **2009**.

[14]   G. Von Maltzahn *et al.*, "Nanoparticles that communicate in vivo to amplify tumour targeting," *Nat. Mater.*, vol. 10, no. 7, pp. 545–552, **2011**.

[15]   S. Laurent, A. A. Saei, S. Behzadi, A. Panahifar, and M. Mahmoudi, "Superparamagnetic iron oxide nanoparticles for delivery of therapeutic agents: opportunities and challenges," *Expert Opin. Drug Deliv.*, vol. 11, no. 9, pp. 1449–1470, **2014**.

[16]   S. Laurent *et al.*, "Magnetic iron oxide nanoparticles: Synthesis, stabilization, vectorization, physicochemical characterizations and biological applications," *Chem. Rev.*, vol. 108, no. 6, pp. 2064–2110, **2008**.

[17]   M. A. Chuev and J. Hesse, "Nanomagnetism: Extension of the Stoner-Wohlfarth model within Néel's ideas and useful plots," *J. Phys. Condens. Matter*, vol. 19, no. 50, **2007**.

[18]   R. E. Rosensweig, "Heating magnetic fluid with alternating magnetic field," *J. Magn. Magn. Mater.*, vol. 252, no. 1–3 SPEC. ISS., pp. 370–374, **2002**.

[19]   K. M. Krishnan, "Biomedical nanomagnetics: A spin through possibilities in imaging, diagnostics, and therapy," *IEEE Trans. Magn.*, vol. 46, no. 7, pp. 2523–2558, **2010**.

[20]   Y. W. Jun *et al.*, "Nanoscale Size Effect of Magnetic Nanocrystals and Their Utilization for Cancer Diagnosis via Magnetic Resonance Imaging," *J. Am. Chem. Soc.*, vol. 127, no. 16, pp. 5732–5733, **2005**.

[21]   J. H. Lee *et al.*, "Artificially engineered magnetic nanoparticles for ultra-sensitive molecular imaging," *Nat. Med.*, vol. 13, no. 1, pp. 95–99, **2007**.

[22]   N. Bao, L. Shen, Y. H. A. Wang, J. Ma, D. Mazumdar, and A. Gupta, "Controlled growth of monodisperse self-supported superparamagnetic nanostructures of spherical and rod-like $CoFe_2O_4$ nanocrystals," *J. Am. Chem. Soc.*, vol. 131, no. 36, pp. 12900–12901, **2009**.

[23]   S. L. Saville *et al.*, "The formation of linear aggregates in magnetic hyperthermia: Implications on specific absorption rate and magnetic anisotropy," *J. Colloid Interface Sci.*, vol. 424, pp. 141–151, **2014**.

[24]   J. Mohapatra, A. Mitra, D. Bahadur, and M. Aslam, "Surface controlled synthesis of MFe_2O_4 (M = Mn, Fe, Co, Ni and Zn) nanoparticles and their magnetic characteristics," *CrystEngComm*, vol. 15, no. 3, pp. 524–532, **2013**.

[25]   J. W. Park, K. H. Bae, C. Kim, and T. G. Park, "Clustered magnetite nanocrystals cross-linked with PEI for efficient siRNA delivery," *Biomacromolecules*, vol. 12, no. 2, pp. 457–465, **2011**.

[26]   S. H. Noh *et al.*, "Nanoscale magnetism control via surface and exchange anisotropy for optimized ferrimagnetic hysteresis," *Nano Lett.*, vol. 12, no. 7, pp. 3716–3721, **2012**.

[27]   P. Caravan, J. J. Ellison, T. J. Mcmurry, and R. B. Lauffer, "Gadolinium(III) Chelates as MRI Contrast Agents", Chemical Reviews Volume 99 issue 9 , **1999**.

[28]   V. M. S. Gil and C. F. G. C. Geraldes, *Ressonância Magnética Nuclear: Fundamentos, Métodos e Aplicações*. **2002**.

[29]   J. W. M. Bulte, "The chemistry of contrast agents in medical magnetic resonance imaging", *NMR Biomed.*, vol. 17, no. 4, pp. 210–210, **2004**.

[30]   J. C. Weinreb and A. K. Abu-Alfa, "Gadolinium-based contrast agents and nephrogenic systemic fibrosis: Why did it happen and what have we learned?," *J. Magn. Reson. Imaging*, vol. 30, no. 6, pp. 1236–1239, **2009**.

[31]   A. Forgács *et al.*, "Mono-, Bi-, and Trinuclear Bis-Hydrated Mn^{2+} Complexes as Potential MRI Contrast Agents," *Inorg. Chem.*, vol. 54, no. 19, pp. 9576–9587, **2015**.

[32]   P. Moroz, S. K. Jones, J. Winter, and B. N. Gray, "Targeting liver tumors with hyperthermia: Ferromagnetic embolization in a rabbit liver tumor model," *J. Surg. Oncol.*, vol. 78, no. 1, pp. 22–29, **2001**.

[33]   E. Pöselt *et al.*, "Relaxivity optimization of a pegylated iron-oxide-based negative magnetic resonance contrast agent for T2-weighted spin-echo imaging," *ACS Nano*, vol. 6, no. 2, pp. 1619–1624, **2012**.

[34]   D. Ho, X. Sun, and S. Sun, "Monodisperse magnetic nanoparticles for theranostic applications," *Acc. Chem.*

Res., vol. 44, no. 10, pp. 875–882, **2011**.

[35] S. Tong, S. Hou, Z. Zheng, J. Zhou, and G. Bao, "Coating optimization of superparamagnetic iron oxide nanoparticles for high T2relaxivity," *Nano Lett.*, vol. 10, no. 11, pp. 4607–4613, **2010**.

[36] T. J. Yoon, H. Lee, H. Shao, S. A. Hilderbrand, and R. Weissleder, "Multicore assemblies potentiate magnetic properties of biomagnetic nanoparticles," *Adv. Mater.*, vol. 23, no. 41, pp. 4793–4797, **2011**.

[37] O. T. Bruns *et al.*, "Real-time magnetic resonance imaging and quantification of lipoprotein metabolism in vivo using nanocrystals," *Nat. Nanotechnol.*, vol. 4, p. 193, Jan. **2009**.

[38] J. M. Perez, L. Josephson, and R. Weissleder, "Use of magnetic nanoparticles as nanosensors to probe for molecular interactions," *ChemBioChem*, vol. 5, no. 3, pp. 261–264, **2004**.

[39] J.-H. Lee *et al.*, "Exchange-coupled magnetic nanoparticles for efficient heat induction," *Nat. Nanotechnol.*, vol. 6, p. 418, Jun. **2011**.

[40] Z. Nemati *et al.*, "Improving the Heating Efficiency of Iron Oxide Nanoparticles by Tuning Their Shape and Size," *J. Phys. Chem. C*, vol. 122, no. 4, pp. 2367–2381, **2018**.

[41] P. Guardia *et al.*, "Water-Soluble Iron Oxide Nanocubes with High Values of Specific Absorption Rate for Cancer Cell Hyperthermia Treatment," *ACS Nano*, vol. 6, no. 4, pp. 3080–3091, Apr. **2012**.

[42] L. M. Bauer, S. F. Situ, M. A. Griswold, and A. C. S. Samia, "High-performance iron oxide nanoparticles for magnetic particle imaging-guided hyperthermia (hMPI)," *Nanoscale*, vol. 8, no. 24, pp. 12162–12169, **2016**.

[43] R. Das *et al.*, "Tunable High Aspect Ratio Iron Oxide Nanorods for Enhanced Hyperthermia," *J. Phys. Chem. C*, vol. 120, no. 18, pp. 10086–10093, **2016**.

[44] E. Alphandéry, S. Faure, O. Seksek, F. Guyot, and I. Chebbi, "Chains of Magnetosomes Extracted from AMB-1 Magnetotactic Bacteria for Application in Alternative Magnetic Field Cancer Therapy," *ACS Nano*, vol. 5, no. 8, pp. 6279–6296, Aug. **2011**.

[45] G. Salas *et al.*, "Modulation of magnetic heating via dipolar magnetic interactions in monodisperse and crystalline iron oxide nanoparticles," *J. Phys. Chem. C*, vol. 118, no. 34, pp. 19985–19994, **2014**.

[46] D. L. J. Thorek, A. K. Chen, J. Czupryna, and A. Tsourkas, "Superparamagnetic iron oxide nanoparticle probes for molecular imaging," *Ann. Biomed. Eng.*, vol. 34, no. 1, pp. 23–38, **2006.**

[47] U. Gneveckow *et al.*, "Description and characterization of the novel hyperthermia- and thermoablation-system MFH®300F for clinical magnetic fluid hyperthermia," *Med. Phys.*, vol. 31, no. 6, pp. 1444–1451, **2004**.

[48] M. Arruebo *et al.*, "Assessment of the evolution of cancer treatment therapies," *Cancers (Basel).*, vol. 3, no. 3, pp. 3279–3330, **2011**.

[49] H. Vilaça *et al.*, "Self-assembled RGD dehydropeptide hydrogels for drug delivery applications," *J. Mater. Chem. B*, vol. 5, no. 43, pp. 8607–8617, **2017**.

[50] P. M. T. Ferreira, L. S. Monteiro, G. Pereira, L. Ribeiro, J. Sacramento, and L. Silva, "Reactivity of dehydroamino acids and dehydrodipeptides towards N- bromosuccinimide: Synthesis of β-bromo- and β,β-dibromodehydroamino acid derivatives and of substituted 4-imidazolidinones," *Eur J. Org. Chem.*, no. 35, pp. 5934–5949, **2007**.

[51]   N. J. Greenfield, "Using circular dichroism spectra to estimate protein secondary structure," *Nat. Protoc.*, vol. 1, no. 6, pp. 2876–2890, **2007**.

[52]   C. D. Ramos CHI, "The use of circular dichroism spectroscopy to study protein folding, form and function.," *Afr J Biochem Res*, no. 3, pp. 164–173, **2009**.

[53]   B. H. Stuart, "Infrared Spectroscopy of Biological Applications: An Overview," *Encycl. Anal. Chem.*, **2012**.

[54]   A. V. Dobrynin and J. M. Y. Carrillo, "Universality in nonlinear elasticity of biological and polymeric networks and gels," *Macromolecules*, vol. 44, no. 1, pp. 140–146, **2011**.

[55]   J. Estelrich, M. J. Sánchez-Martín, and M. A. Busquets, "Nanoparticles in magnetic resonance imaging: From simple to dual contrast agents," *Int. J. Nanomedicine*, vol. 10, pp. 1727–1741, **2015**.

[56]   N. Guldris *et al.*, "Influence of the separation procedure on the properties of magnetic nanoparticles: Gaining in vitro stability and T1-T2magnetic resonance imaging performance," *J. Colloid Interface Sci.*, vol. 472, pp. 229–236, **2016**.